

MASTER THESIS

SENSITIVITY ANALYSIS OF A DEM MODEL
FOR THE DRY-MIXING OF CONCRETE
CONSTITUENTS IN A SCREW-CONVEYOR

AUTHOR

Raïsa N. Roeplal

Faculty of Engineering Technology, Department of Mechanical Engineering
Chair of Thermal & Fluid Mechanics

EXAMINATION COMMITTEE

Chairman: prof. S. Luding

Supervisor: dr. T. Weinhart

External member: prof. dr. ir. C. H. Venner

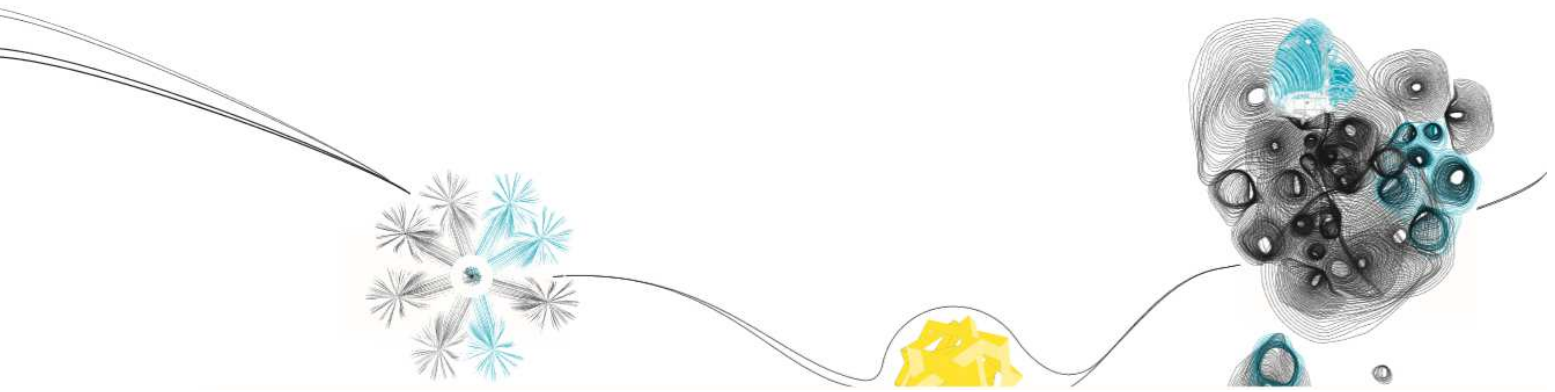
External member: I. Vrooijink, MSc.

DOCUMENT NUMBER

ME - 325

DATE

October 31st, 2019



UNIVERSITY OF TWENTE.

SENSITIVITY ANALYSIS OF A DEM MODEL FOR THE DRY-MIXING OF CONCRETE CONSTITUENTS IN A SCREW-CONVEYOR

Author

Raïsa N. Roeplal

University of Twente

Faculty of Engineering Technology

Department of Mechanical Engineering, Thermal & Fluid Engineering, Multi-Scale Mechanics group

ID-number: s1817094

e-mail: r.n.roeplal@student.utwente.nl

Graduation Committee

Chairman: prof. Stefan Luding

Supervisor: dr. Thomas Weinhart

External member: prof. dr. ir. C. H. Venner

External member: I. Vrooijink, MSc.

Report number: 325

October 21, 2019

PREFACE

This thesis embodies the work I have done to conclude my ME-Master studies at the University of Twente. Throughout my time at the UT I have learned a lot –academically, socially, mentally– and have gotten to know many people who have supported me and, in this way, have also contributed to this work. I would like to take this opportunity to share my experiences and thank them.

First of all, to those who made this work possible: Ivo Vrooijink, dr. Thomas Weinhart and prof. Stefan Luding. In the second year of my studies, I became interested in concrete printing technologies and decided to focus on this field for my thesis. During my search for a graduation project I came into contact with Ivo, who supervises the concrete printing project “Konkreet” at the Saxion University of Applied Sciences. After expressing my interest in the field he provided me with the opportunity to use the Konkreet lab-scale printer for my research, which I am very grateful for. It soon became clear that my research would be conducted at the Multiscale Mechanics group of the TFE department under the supervision of prof. Luding and dr. Weinhart, whom I have gotten to know as very kind and helpful individuals. At the beginning of this project I had a clear goal of what my model would be able to predict, and I figured that the hardest part in the model development process would be the derivation of appropriate mathematical relations from the literature. During the first few weeks I quickly realized that developing a model is a much more complicated and lengthy process that I had anticipated, and that one of the biggest challenges for me would be to learn other important skills such as programming and debugging! Moreover, I discovered that mathematical relations are generally well-established and selecting the “right” parameters for these relations is the most difficult part in DEM modeling. Thanks to the efforts of prof. Luding and dr. Weinhart, I received a crash course in MercuryDPM and was able to learn the concepts of DEM much faster. I am thankful for their guidance and I would especially like to thank dr. Weinhart for taking his time to assist me with software-related issues. Throughout this project, my conversations with prof. Luding have taught me things that I will always remember and will continue to apply in other areas of my life: “take small steps, be optimistic and never say that your work is not good enough”.

Secondly, to my sister Nikita, my boyfriend Joël, and my Surinamese friends who became more like family: Lakshna, Santosh, Shailin, Viraj, Siroshni and Annemieke. I thank you for your warmth and support, and allowing me to feel safe while I rant about anything and everything, knowing that you would understand. When I first joined the UT, I never expected meeting other people from all over the world who ironically made this place feel more like home. Yibo, Zheng Ling and Joel, my trusted study partners who have also become my good friends. Thank you for all the work we have done together; though not effortlessly, but with great ease as a team.

Finally, to my parents: there are not enough words to describe my gratitude to you for sacrificing so much to make this journey possible. I dedicate this thesis to you.

ABSTRACT

The quality of fresh concrete has been reported to show a direct dependency on the concrete composition, the mixing methods, and the mixer conditions. Despite this link between concrete quality and mixing parameters, the general use of mixers for specific purposes is still marked by many uncertainties. While it is well-known that each type of concrete requires a specific combination of mixing tools and processing parameters, a theoretical framework on how to integrate these factors is still lacking and the quality of the mixed product is optimized through trial-and-error in practice. Numerical simulations are expected to be a powerful tool to understand the mechanics of, and to predict fresh concrete quality, for various operating conditions and mixer geometries. This study is intended to set up a model that is able to predict the behavior of moist concrete constituents in a screw conveyor, which provides pre-blending of the ingredients during their transportation to the main mixer of a lab-scale 3D concrete printer. Since the material is, in essence, a collection of discrete grains with a small amount of interstitial liquid, its behavior can be studied using discrete models. The Discrete Element Method (DEM) is a popular simulation scheme which consists of integrating Newton's equations of motion for a system of particles, starting from a known initial configuration. The particles are modeled as solid spheres, with a fictional liquid layer surrounding the grains if the material is wet. The simulation model employed in this study consists of two major aspects, namely the forces acting on the solid particles inside the system as a result of their interactions and the redistribution of interstitial liquid during material handling. Different types of interactions between particles can be distinguished, based on their moisture degree: dry particles interact through repulsion, friction and damping forces depending on the particle properties and the overlap of particles in contact. Moist particles are subject to additional liquid bridge forces as a function of the liquid volume, particle size and the distance between contact partners. Several force models are available for a variety of grain phenomena in literature, ranging from extremely simplified to very detailed expressions. One of the challenges of DEM lies in choosing the most simple contact force model which produces realistic behavior of the material, in order to easily implement the model and interpret results. In this study, the Linear Spring Dashpot model is used to model the contact forces. Despite its simplicity, the model still requires several input parameters to be known before it can be utilized to reproduce the material behavior accurately. These parameters are generally determined through bulk calibration experiments, where the parameters are "fitted" to match experimental results. This procedure is known to be extremely time-consuming, especially for a large collection of unknowns. Sensitivity analyses are often performed beforehand to determine the importance of specific DEM input parameters for a given system and potentially allow them to be excluded from the timely calibration process. The sensitivity analyses are the main focus of the simulations performed in this study.

LIST OF SYMBOLS

Symbol	Description	Unit
\vec{a}	Acceleration	m/s ²
a	Radius	m
Bo	Bond number	-
\vec{F}	Force vector	N
k	Stiffness	N/m
m	Mass	kg
M	Mixing index	-
\vec{n}	Normal vector	-
\vec{r}	Position vector	m
S	Separation distance	m
\vec{T}	Torque vector	Nm
\vec{t}	Tangential vector	-
t_c	Contact time	s
\vec{v}	Velocity vector	m/s
V_D	Distributable liquid volume	m ³
V_{Lmin}	Liquid volume trapped inside the particles	m ³
V_{LB}	Liquid bridge volume	m ³
γ	Viscous dissipation	kg/s
δ	Overlap	m
ϵ	Restitution coefficient	-
μ	Friction coefficient	-
ρ_b	Bulk density	kg/m ³
ρ_p	Particle density	kg/m ³
σ	Surface tension	N/m
ω	Angular velocity	rad/s
θ	Contact angle	rad

LIST OF SUBSCRIPTS & SUPERSCRIPTS

Subscript	Description
<i>i, j</i>	Refers to particle <i>i, j</i>
<i>ij</i>	Between particle <i>i</i> and <i>j</i>
<i>nb</i>	Nearest neighbors
<i>p</i>	Refers to a particle
<i>w</i>	Refers to a wall

Superscript	Description
<i>b</i>	Body
<i>c</i>	Contact
<i>eff</i>	Effective
<i>n</i>	Normal
<i>nc</i>	Non-contact
<i>ro</i>	Rolling
<i>s</i>	Sliding
<i>t</i>	Tangential
<i>to</i>	Torsion

CONTENTS

Acknowledgements	i
Abstract	iii
List of Symbols	v
List of Symbols	vi
1 Introduction	1
1.1 Context & motivation	1
1.2 Research objective & scope	4
1.3 Research design & structure	5
1.4 Research contributions	6
2 Literature Review: Wet Granular Mixing	8
2.1 Concrete: a wet granular material	8
2.1.1 Introduction to granular materials	8
2.1.2 Forces acting in granular materials	10
2.2 Granular mixing	13
2.2.1 Mixing mechanisms	14
2.2.2 Wet granular mixing	14
2.3 Modeling granular mixtures	16
2.3.1 Fundamentals of DEM	16
2.3.2 Mixing characterization	20
2.4 Overview of screw conveyor mixing studies	21
2.4.1 Analyses on the effects of material properties	21
2.4.2 Analyses on the effects of equipment design	22
2.4.3 Analyses on the effects of operating conditions	22
3 Model Development	25
3.1 System and relevant phenomena	25
3.2 Objective & Scope	27
3.3 Physical model formulation	27
3.3.1 Contact models	27
3.3.2 Liquid migration model	32

3.4	Numerical model formulation	35
3.5	Software implementation	37
3.5.1	Source Code	37
3.5.2	Output data	39
4	Model Implementation	40
4.1	Goal	40
4.2	Simulation Conditions & Procedure	41
4.2.1	Geometry	41
4.2.2	Particles	43
4.2.3	Species	43
4.3	Reference simulation	47
4.3.1	Stiffness analysis	48
4.3.2	Particle density	48
4.4	Particle resolution analysis	49
4.5	Effects of interaction parameters	50
4.5.1	Effect of friction	50
4.5.2	Effect of the restitution coefficient	59
4.5.3	Effect of cohesion	64
4.5.4	Effect of water intake	68
4.6	Effect of mixing element geometry	70
5	Discussion & Recommendations	71
5.1	Conclusions	71
5.2	Recommendations and future work	72
	References	79
A	Extended literature: the basics of concrete mixing	80
A.1	General material components	80
A.1.1	Cement paste	80
A.1.2	Aggregates	82
A.1.3	Admixtures	82
A.2	Material mix design	84
A.2.1	Material requirements	84
A.2.2	Types of concrete	85
A.3	Concrete handling equipment	87
A.3.1	Transportation screws	87
A.3.2	Mixers	87

1

INTRODUCTION

1.1 CONTEXT & MOTIVATION

Over the past few decades, a clear trend of automation in manufacturing technologies has changed the way we live and work. Nowadays, almost all large-scale consumer products are being produced through highly automated manufacturing processes, allowing for higher productivity, lower costs and increased efficiency. While most industries are already benefiting from these developments, the construction industry still lags behind. To this day, building methods as we know them are generally labor intensive, inefficient and nontransparent, therefore highly prone to corruption and delays. In this era of automation and digitization, a new technology has been introduced to the construction industry, redefining both the design and production process: 3D printing or additive manufacturing (AM). Despite the fact that the printing technology has already proven its potential in a wide range of disciplines, varying from the medical world to the food industry and from aerospace engineering to household uses, it is a relatively new concept in the building and construction industry. Besides the aspect of automation, the main advantage of AM is the capability to produce complex, curvilinear structures with the same effort as traditional rectilinear structures.

The term “3D printing” encompasses a broad range of manufacturing technologies which involve the successive deposition of material layers based on a digital model, until a three dimensional physical object is created. There are various ways to create a printed object; the printing processes are all additive in nature, however, they differ with respect to the method which is applied for building the layers. The construction printing methods which have been developed thus far are mainly based on two techniques: extrusion-based AM and powder-based AM. The extrusion-based techniques are analogous to the Fused Deposition Modeling (FDM) method in additive manufacturing, where material is extruded from a nozzle mounted on a gantry, crane or a robotic arm to print building elements layer-by-layer. This technique relies on the bonding between printed layers and the proper hardening time of the extruded filament for the structure to maintain its shape. The powder-based techniques use the same operating principles as the binder jetting additive manufacturing technology, where layered

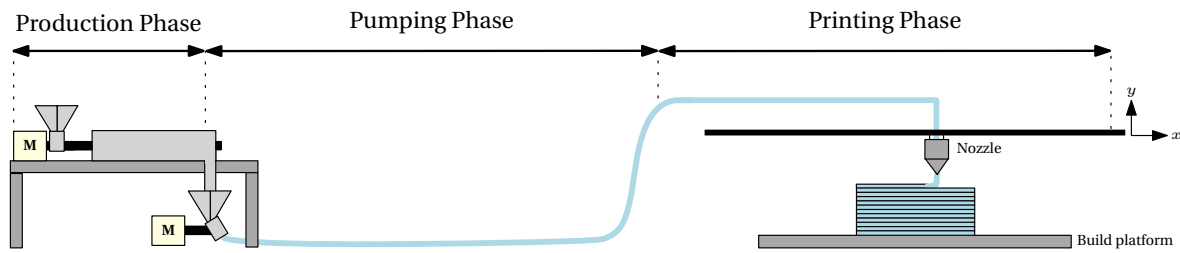


FIGURE 1-1. Illustration of the extrusion-based concrete printing process, consisting of production phase, a pumping phase and a printing phase.

structures are built by selectively depositing a binding agent into a powder bed. The concrete elements are produced either by using cement powder and water (or another liquid) as the binder, or by injecting cement paste into an aggregated bed. A chemical reaction between the binder and the aggregate causes local hardening, resulting in a solidified final structure. In addition to printing techniques, different materials suitable for construction printing have also been explored. While the techniques were initially based on earth minerals such as sand and ceramics, other specialized resources such as biodegradable materials and polymers are quickly emerging. The majority of construction printing systems worldwide are extrusion-based, with concrete being the most commonly used printing material [1]. This comes as no surprise, as concrete is currently the most widely used building material in all parts of the world. The widespread use of concrete stems from its various benefits, the most important being: i) the wide availability of the material constituents of concrete (cement, aggregates and water); ii) the excellent water resistance and iii) the economy of concrete compared with other forms of construction [2, 3]. Thus, concrete has become a natural material choice for 3D printing in construction. In general, a concrete printing system consists of the printer itself, as well as a production unit which continuously produces fresh printing material and a pumping unit which feeds the material to printer, as seen in Figure 1-1. The most important requirement of the production unit is its ability to continuously deliver a homogeneous product of constant quality to the printer, depending on the printing speed.

In recent years, there have been several developments of the 3D printing technology in building and construction research and industry. Numerous prototypes have been successfully developed and are currently being commercialized in different parts of the world, allowing researchers to believe that 3D concrete printing will highly benefit the construction industry in the near future. Despite the positive prospects, this technology is still in its infancy and most of the research done in this field has been dedicated towards analyzing its viability. Fundamental understanding of the process parameters – for both the material production as well as the material extrusion – is still limited. Thus, 3D concrete printing has become a field of interest to many research institutes. In the Netherlands for example, the Eindhoven University of Technology built a 3D concrete printing facility where pioneering research is done on the dependency between the design, material, print process and final printed product. Additional concrete printing topics are also studied in collaboration with the Delft University of Technology through the “4TU.Bouw Center of Excellence for the Built Environment”, an alliance between the Dutch technical universities with the goal of strengthening research and exchanging knowledge [4, 5]. Recently, a research group at the Saxion University of Applied Sciences in Enschede also acknowledged the importance of keeping up with the developments of this trending technology and, in this regard, initiated the long-term project “Konkreet” in order to acquire technical knowledge and expertise in the field of extrusion-based 3D concrete printing. In the initial stages of this project, a

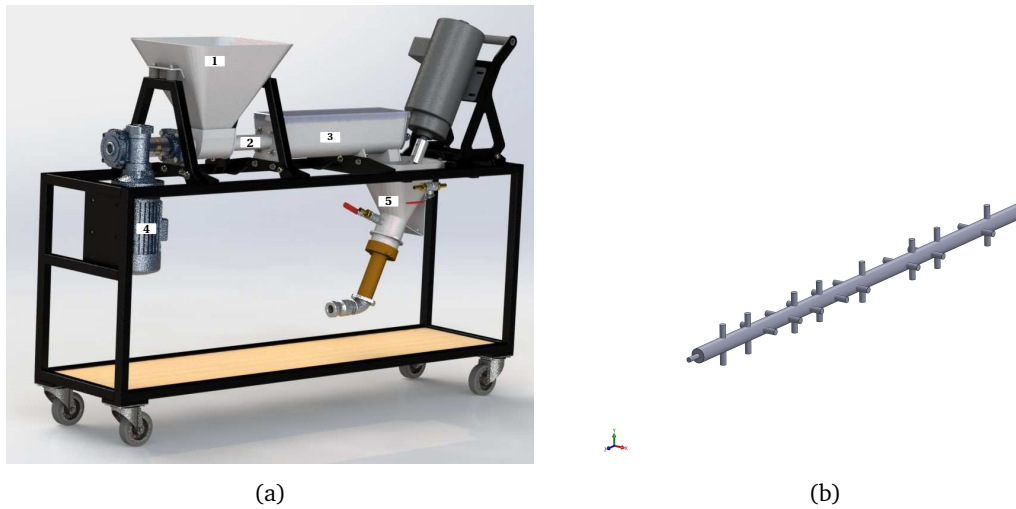


FIGURE 1-2. Illustration of (a) the initial Konkreator production unit; (b) the initial mixing element used for the wet-mixing process.

lab-scale printer, the “Konkreator”, was developed by students from different backgrounds to perform tests for a variety of object designs. Several studies have been dedicated towards improving the system operation and deriving an optimal concrete “recipe” for printing. The initial design of the Konkreator’s production unit is shown in Figure 1-2a. Since a 3D concrete printing system requires continuous operation, the production unit consists of a (or several) continuous concrete mixers. The current continuous production unit is described as follows. First, all dry ingredients are added to the hopper (1), allowing them to fall towards the feeding screw (2), which provides preliminary mixing of the dry ingredients and transports the material to the inlet of the main mixer (3). The feeding screw and the mixer shaft are driven by the same electric motor (4). The mixer itself consists of a horizontal mixing container with therein a mixing element (Figure 1-2b) and a water inlet which allows water to be injected into the mixer while the mixing element incorporates the liquid into the mixture as it travels towards the outlet. Next, the material enters the mortar pump via the second hopper (5), allowing it to be transported to the printing nozzle. Based on this description, the mixing process can be thought of as a sequence of two main processes: i) the dry-mixing process in unit (2), where preliminary mixing of the dry ingredients occurs and ii) the wet-mixing process in unit (3), where mixing of the dry ingredients with water occurs.

The main performance issue with this production system is concerned with the mixture quality at the end of the wet-mixing process. In 2018, an optimization study involving several tests using the initial system was performed. First of all, it was noticed that the water added in the mixing container was able to pass the mixer inlet and accumulate in the housing of the feeding screw. Also, the mixing element was not capable of properly transporting the mixture towards the container outlet, which resulted in accumulation inside the container. Moreover, the material that did reach the mortar pump was not properly mixed. This was assumed to be caused by insufficient mixing time, since it was observed that water was being transported through the mortar pump while the granular materials became clustered and caused clogging of the pump. Also, according to literature research performed during the study, a mixing time of 4-6 minutes is required for proper incorporation of water into the dry ingredients, which could not be achieved with the initial design of the mixing unit [6]. Hence, a

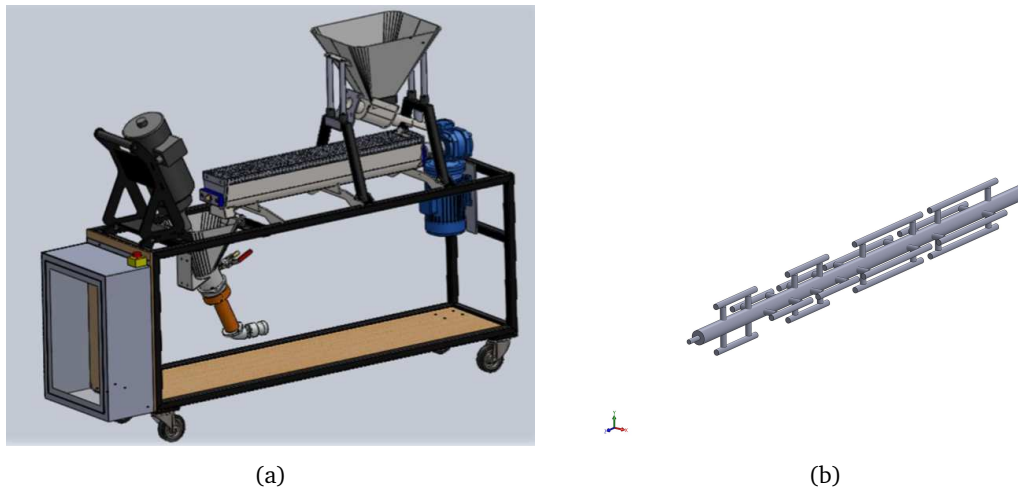


FIGURE 1-3. Illustration of (a) the modified Konkreator production unit; (b) the modified mixing element used for the wet-mixing process.

modified design shown in Figure 1-3a was proposed to tackle these shortcomings. In order to eliminate the possibility of water accumulation in the feeding screw housing, the hopper was mounted on top of the mixing container so that dry materials would enter the mixer from the top, instead of from the side. The relocation of the hopper and feeding screw provided extra space, which was conveniently used to elongate the mixer. This provided the opportunity to increase the mixing time, which was expected to enhance the quality of the mixture entering the mortar pump. Additionally, extra elements were added to the mixing shaft, as seen in Figure 1-3b.

Despite these modifications the quality of the substance being fed to the printing nozzle still suffered from inadequate mixing. This was evident from “lumps” in the material at the mixer outlet. Based on this information, the following problem is identified: it is currently unclear which combination of factors results in the bad mixer performance and therefore it is not known what has to be done to reach an optimal mixture quality.

1.2 RESEARCH OBJECTIVE & SCOPE

Since a reliable, fully functional printer is a primary necessity for gaining knowledge and experience in the concrete printing field, it is clear that future research regarding the mixing process for extrusion printing is required. In the past, the quality of fresh concrete has been reported to show a direct dependency on the concrete composition, the mixing methods and the mixer conditions. While the characteristics of concrete and its constituents are well-described in standards, there are no explicit guidelines and/or regulations regarding the actual production process, the mixing. For example, according to DIN EN 206-1: i) “The mixer must be able, with its available capacity, to achieve an even distribution of the raw materials and an even workability of the concrete within the mixing time” (art. 9.6.2.3) and “Mixing the raw materials must take place in a mixer according to 9.6.2.3 and take such a time needed for the mixture to appear homogeneous” (art. 9.8). Thus, mixing processes are highly subjective, giving the user freedom to find an optimum combination of material proportions, mixing time, velocity and geometry of the mixing tools and the mixing sequence which produces fresh

concrete with acceptable homogeneity. Concrete mixing is most often performed using automated mixers, which have been commercially available for many years with no reported problems in recent literature [7]. Hence, the majority of hardware design improvements has been dedicated towards increasing the energy efficiency of the mixer without affecting the concrete quality, rather than the ability to produce a homogeneous mixture [8]. However, with the development of new concrete types – for example 3D printing of concrete – the traditional mixing tools and processes must to be reevaluated in combination with specific production requirements. For example, ultra-high performance concrete (UHPC) and fiber-reinforced concrete require more specialized mixing techniques when compared to ordinary concrete due to poor miscibility [9]. The increasing complexity of concrete recipes is associated with specific production requirements, which in turn calls for higher quality control of fresh concrete. In practice, mixing procedures are generally established on a trial-and-error basis where the mixture uniformity can be examined through physical experiments such as sampling, or more advanced methods such as X-ray tracking or positron emission particle tracking (PEPT). Although these methods provide useful first-hand information on particle behavior, they are time-consuming, expensive procedures which are usually applied selectively to very few particles. Nowadays, numerical analyses are being recognized as a powerful research tool in addition to theoretical and experimental analyses, saving both time and costs. Several computational models have been developed to enhance the understanding of material mixing processes. More particularly, the discrete element method (DEM) has shown its capability to predict the behavior of granular flows which are comprised of individual solid particles, by calculating the motion of each particle in the flow. This method has previously been used for mixing analyses of mostly dry and, to a limited extent, wet granular materials with the aid of different software packages. At the University of Twente, the MercuryDPM is used for performing discrete particle simulations. While this program has been utilized successfully for modeling various granular flow phenomena, its capability to model a complex process such as concrete mixing is yet to be explored.

Given the aforementioned, it is clear that the increasing demand for reliable concrete production processes coupled with inadequate experimental techniques for assessing fresh concrete quality require further understanding and development of concrete mixing models. Although DEM simulations are frequently used for mixing analyses, it is well-known that the development of such models is a very time-consuming process in which the complexity increases with the type and number of material interactions occurring within the system. While the development of a concrete mixing model is a challenge in itself, the implementation of such a model in a software program must also be considered. Hence, the goal of this study is to set the first steps in developing a concrete mixing model in MercuryDPM, which is able to predict the mixture quality for various operating conditions. In this regard, the focus of the model will be limited to simulating the dry-mixing process in the screw conveyor.

1.3 RESEARCH DESIGN & STRUCTURE

In order to achieve the defined objective, the research is divided into several phases with dedicated tasks, as shown in Figure 1-4. The first phase consists of a literature review (Section 2), where the main goal is to gain knowledge of the relevant phenomena occurring during the concrete mixing process and how these phenomena are modeled mathematically. This includes, first of all, understanding of the granular nature of concrete flow and how granular mixing is described in literature. Next, the

DEM is introduced for modeling the mixing process as well as assessing the degree of mixing. Also, an overview of previous relevant mixing studies based on this method is provided. The next research phase (Section 3) is dedicated towards developing the mathematical model which is able to capture the relevant phenomena which occur during the dry-mixing process, as well as the numerical scheme which is appropriate for the simulations. An important task in the model development process is the model calibration, i.e., determining the input parameters for the simulation which provide the correct physical behavior of the material in the mixer. This is a crucial step which must be performed before the model can be used to accurately re-design the system. Depending on the number of model inputs, the calibration process can be very lengthy as the experiments must be repeated several times to scrutinize the effect of each parameter. In this regard, the general approach is to first perform sensitivity analyses, which give more insight on the significance of each parameter on the material behavior. Hence, the final phase (Section 4) of this research is dedicated towards using the computational model to perform the sensitivity analyses, so that future research can be directed towards the calibration and implementation of the model. This work is concluded in Section 5, where the findings of the study are discussed and recommendations for further work are provided.

1.4 RESEARCH CONTRIBUTIONS

The contribution of this thesis is twofold. First and foremost, this work is relevant in the field of concrete printing research. Concrete in general is a very complex composite material, with its behavior being dictated by many factors, one of which is the production method. One of the major challenges in concrete technology is the lack of guidelines regarding production methods for the different types of concrete. Even today, the typical varieties which have been used for decades are mainly produced through trial-and-error and experienced operators. This lack of scientific knowledge is currently extending towards the relatively new “printing concrete”, which has entirely different properties in its fresh state. Hence, the heuristic production methods used for typical concrete types cannot simply be adapted to printing concrete and in-depth research is required for the efficient production of this material. Secondly, the simulations performed in this study contribute to the further development of the MercuryDPM package, which is currently being expanded in terms of its applicability to different systems and physical phenomena. At the moment, packages for analyzing low-liquid content granular materials –which include phenomena such as liquid bridge formation and liquid migration– in standard system geometries are already available in MercuryDPM. However, simulations for mixing high liquid content materials in customized systems require further programming and testing.

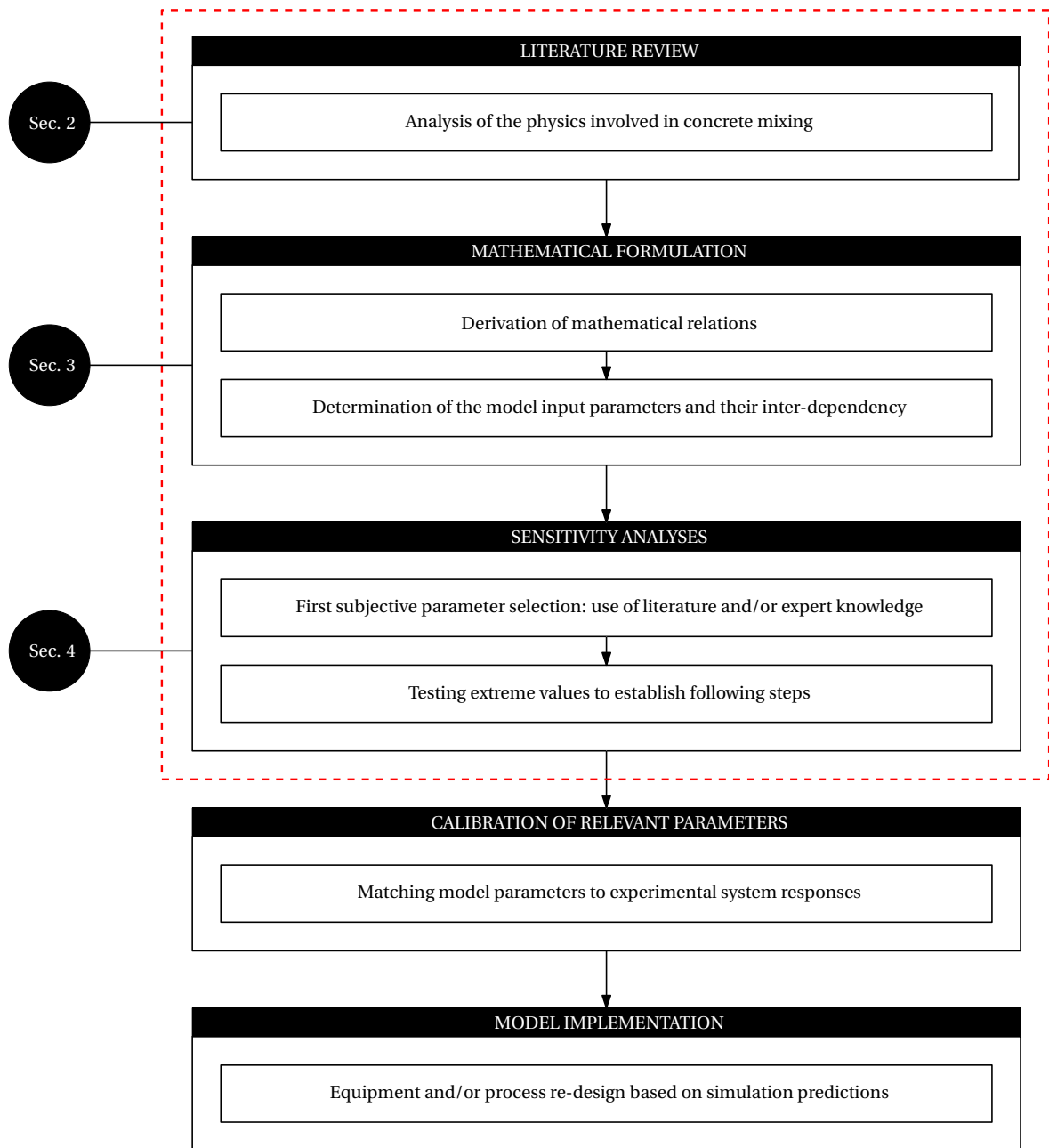


FIGURE 1-4. General workflow in developing a model for equipment re-design. The focus of this study is limited to the first three steps.

2

WET GRANULAR MIXING

INTRODUCTION

The aim of this section is to form a basis for understanding how concrete mixing processes can be modeled numerically. In order to achieve this goal, it will first be discussed how concrete fits the description of a granular material. Next, the principles of granular mixing are discussed. This includes a summary of the phenomena which are believed to govern the mixing process and how this theory can be translated to concrete mixing processes. Finally, the Discrete Element Method is introduced as a method for modeling granular mixing, followed by a description of how the quality of a mixture can be quantified and lastly, a summary of previous studies in continuous and/or screw conveyor mixers based on the DEM.

2.1 CONCRETE: A WET GRANULAR MATERIAL

2.1.1 INTRODUCTION TO GRANULAR MATERIALS

An concrete material analysis is presented in Appendix A. From the theory, it is clear that the dry ingredients of concrete are collections of discrete grains ranging in size: coarse grains (large aggregates), fine grains (sand) and very fine grains (cement and admixtures). Materials of this (discrete) nature are commonly known as “granular” matter and they are studied extensively in literature. A granular material can be defined as a collection of solid particles (grains), which can be of different sizes and shapes and where the majority of the particles is in contact with at least some of its neighboring particles [10]. Because of their diversity, granular materials can be classified in various ways. Richards [11] proposed a classification of granular particles according to their size range, as shown in Table 2-1. While the range values are indicative, the classification is an important aspect since the size of the particles dictates the type of interactions occurring between them. For example, for sizes between 10 and 1000 nm, the particle dynamics are influenced by the temperature-dependent motion of the surrounding fluid molecules. On this scale, the particles are referred to as “colloids”. While this effect

can be ignored for larger particles such as powders, other effects such as Van der Waals forces between the particles must still be considered [12, 13]. A special case arises for particles which are typically larger than 100 μm : here, ordinary temperature plays no role and the particle-particle interactions are dissipative [14]. Some typical examples are sand, sugar or seeds. Due to the macroscopic size of the grains, classical mechanics is all that is relevant to describe the particle dynamics and the particles are not sensitive to thermal energy, $k_B T$ (k_B , Boltzmann's constant; T , normal temperature). Also, force interactions between the particles are usually only repulsive in nature, since cohesion is most likely negligible in cases of dry granular material. Moreover, the shape of the particles often has no effect on the qualitative behavior of the material, so that the grains can be treated as point-objects [15].

Despite this seemingly simple description, granular materials in this range are known to exhibit unusual behavior, when compared to common materials which are classified as solids, liquids or gases. For example, granular materials can exist under different states. This behavior can be attributed to the dissipative nature of the grains: when two grains collide with each other, some of their kinetic energy is transformed into other forms due to the fact that the particle collisions are inelastic and that static friction occurs during interaction. Thus, the particles must be agitated externally (through gravity, vibrations, etc.) in order to stay in motion. Depending on the rate of energy input, a granular material can stay at rest as a solid, flow like a liquid or behave like a gas, as illustrated in Figure 2-1 [16].

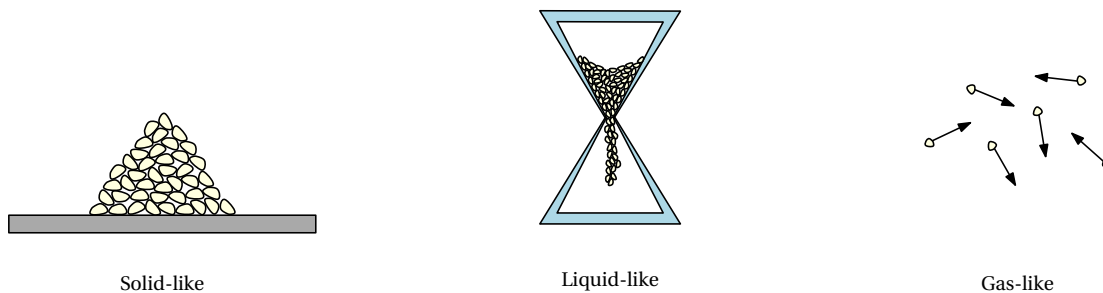


FIGURE 2-1. Illustrations of granular materials acting as a solid (left), a liquid (center) and a gas (right).

TABLE 2-1. Classification of particles based on their size, adapted from [11].

Particle size range	Material type	Individual component
0.1 μm - 1.0 μm	Ultra-fine powder	Ultra-fine particle
1.0 μm - 10 μm	Super-fine powder	Super-fine particle
10 μm - 100 μm	Granular powder	Granular particle
100 μm - 3.0 mm	Granular solid	Granule
3 mm - 10 mm	Broken solid	Grain

When considering cohesion due to the presence of a liquid phase, granular materials can be categorized as dry, (fully) saturated or partially saturated matter. In the first case, the voids between the grains are completely occupied by a gas (usually air), while in the second case, the fluid is a liquid. In the last case, some of the voids are filled with a liquid and the rest is filled with a gas. When the voids are large such that the grains are no longer in contact with each other, but rather they are surrounded by a fluid, the material is considered to be a fluid-particle suspension (slurry). As seen in Table 2-2, three regimes

are often distinguished for partially saturated material based on liquid content: the pendular state, the funicular state and the capillary state.

TABLE 2-2. Granular material with various amounts of liquid where, in the illustrations, the filled circles represent solid grains and the blue regions represent the interstitial liquid; adapted from [16].

Liquid content	State	Illustration	Description
No	Dry		Cohesion between grains is negligible.
Small	Pendular		Liquid bridges are formed at the contact points of grains. Cohesive forces act through the liquid bridges.
Middle	Funicular		Liquid bridges around the contact points and liquid-filled pores coexist. Both give rise to cohesion between particles.
Almost saturated	Capillary		Almost all the pores are filled with the liquid, but the liquid surface forms menisci and the liquid pressure is lower than the air pressure. This suction results in a cohesive interaction between particles.
More	Saturated		The liquid pressure is equal to, or higher than, the air pressure. No cohesive interaction appears between particles.

2.1.2 FORCES ACTING IN GRANULAR MATERIALS

Depending on the application, a combination of various forces can act on solid particles in a granular material. A summary of the most frequently encountered forces is shown in Figure 2-2. Hydrodynamic forces and body forces are well-known and will not be discussed further. Contact forces occur between two solid objects in the material once they come into contact; these forces will be discussed in great detail at a later stage. In the following, the different types of adhesive forces will be introduced as they are important for this study.

The term “adhesion” refers to the tendency of particles to stick together due to inter-particle attraction forces. A distinction is made between “adhesive” and “cohesive” interactions: cohesion refers to the attraction of surfaces of the same material, while adhesion more generally accounts for different surfaces (for example, attraction between a particle and a wall). Different adhesive forces become dominant depending on the particle size, as shown in Table 2-4. Some of the origins of adhesion between solids in a granular material are:

- *Surface and field forces at direct contact*

Forces of this nature are illustrated in Figure 2-3a:

- The van der Waals force is a distance-dependent attractive or repulsive force acting between particles, which decreases with the sixth power of the distance between the particles and with decreasing size of the particle. Thus, although the force is larger for bigger particles of the same substance, the inertial forces on particles decrease to a greater

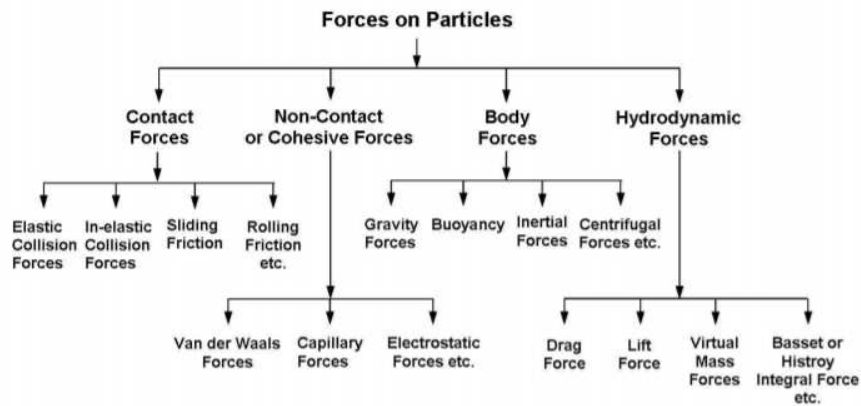


FIGURE 2-2. Summary of possible forces acting on particles in granular flows.

extent than the van der Waals force as the size decreases, making the van de Waals force dominant for small particles such as dry powders.

- Particles are generally covered with electrical surface charges (bottom middle illustration of Figure 2-3a), especially at sharp edges and corners. Particles (in the order of 10^{-6} m) and surfaces can become charged as a result of friction and frequent rubbing against other and solid surfaces, giving rise to electrostatic forces which are dominant for small particles. As a result, flocculation can occur. For wet granular matter, the liquid becomes trapped and immobilized inside the flocs. Flocculation is promoted by liquid with a small ionising power (for example, with kerosine up to 0.75 l/kg, cement is stiff and buttery, while the same amount of water gives a very fluid mortar) [17]. These forces can be attractive and repulsive, based on how the surfaces are charged, and can remain active between particles which are separated by a relatively long distance. Another type of interaction becomes important for colloidal particles (in the order of 10^{-9} m). Colloids dispersed in a solution become ionized (electrically charged) at their surface, usually due to the adsorption of ions (both positive and negative) present in the liquid onto the surface of the particle. The charge at the particle surface affects the ions in the nearby region and increases the concentration of counter ions (ions of charge opposite to that of the particles) close to the surface. This results in the formation of an electrical double-layer at the particle-liquid interface, as seen in the top middle illustration of Figure 2-3a. The liquid layer surrounding each particle is comprised of two parts: an inner region where ions are strongly bound (Stern layer) and an outer, diffuse layer where they are less firmly associated. Within a certain region of the diffuse layer there exists a boundary inside which the ions and the particle form a stable entity. The potential at this boundary is the zeta potential, which generally gives information on the tendency of the particles to attract or repel each other. If all the particles in a suspension have a large negative or positive zeta potential, then they will repel each other and remain discrete. However, if the particles have low zeta potential values they will form flocs.
- Magnetic forces are present in materials which exhibit magnetism (for example iron powder). The magnetic field induces attractive forces on the particles, causing them to

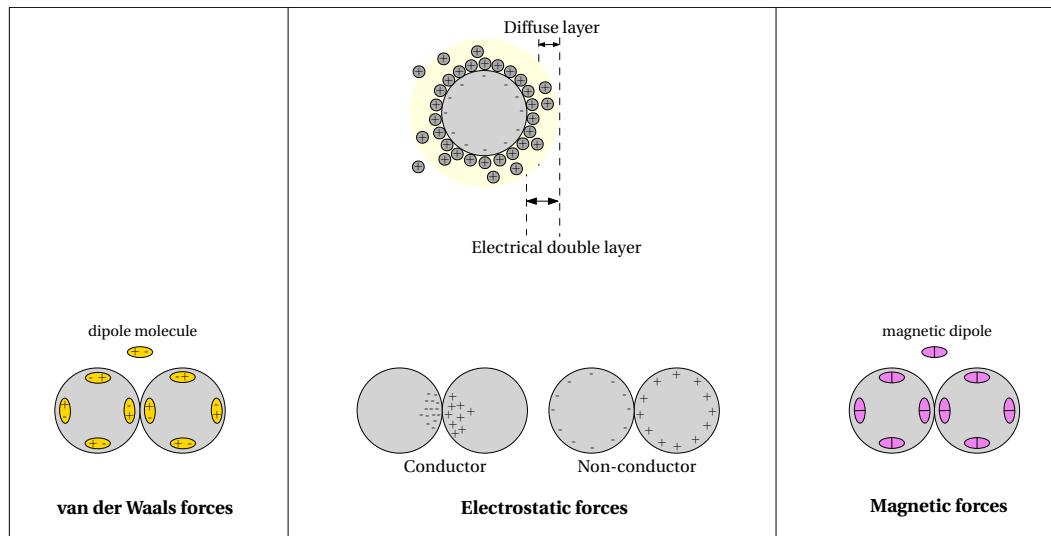
stick together.

- *Material bridges between contacts*

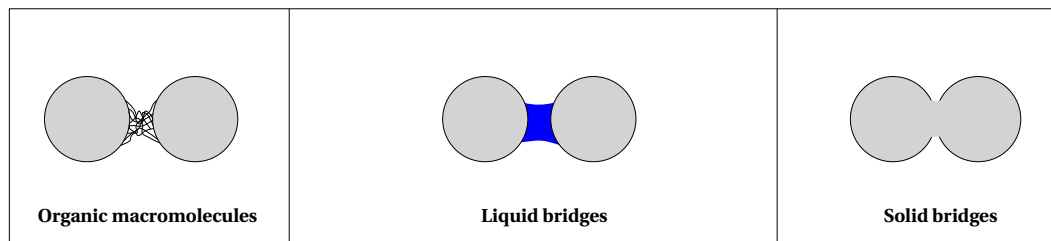
Material bridges are possible due to the adsorption of macromolecules (floculants) on the surface of particles. Other possibilities are the presence of liquid or solid bonds which connect the particles, as shown in Figure 2-3b. Capillary forces play its role for narrow capillaries, so for small particles and only if no excess of water is present [17]. According to Nori and Mitarai [16], capillary forces act through liquid bridges in the pendular state. In the capillary state, the grains are kept together due to suction at the interface between the liquid and the surrounding air. In the funicular state, both of these effects play important roles in cohesion. The capillary adhesion force is, in general, stronger than other adhesion forces such as van der Waals forces and electrostatic forces. While liquid bridge bonds can be ruptured (due to agitation), solid bridges have a more permanent nature. These connections can be formed due to chemical reactions, fusion of the contacts (due to sintering) at high temperatures or freezing of liquid bridges.

- *Interlocking of solids*

Finally, adhesion of particles can be caused due to surface roughness and/or the shape of the particles in contact, as shown in Figure 2-3c.



(a) Surface and field forces at direct contact



(b) Material bridges between contacts

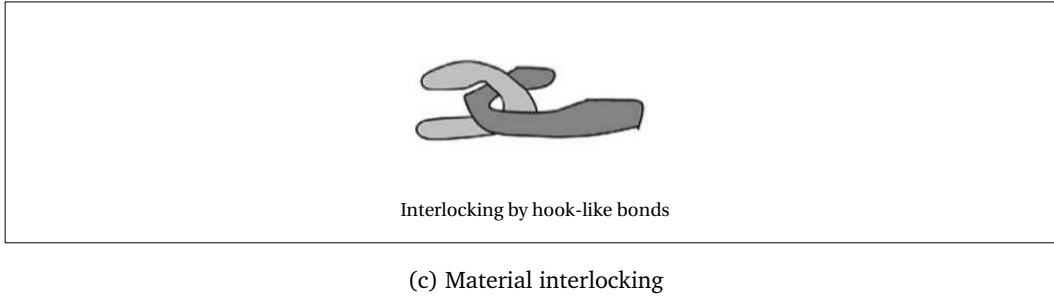


FIGURE 2-3. Mechanisms of particle adhesion, adapted from [18].

TABLE 2-4. Forces acting between particles embedded in a liquid, based on their size; adapted from [17].

Particle size [mm]	Type of force	Attractive effect	Repulsive effect
1 – 30	Mechanical	none	none
0.1 – 1	Capillary	yes	no
$2 \times 10^{-4} - 0.1$	Flocculation	yes	no
$1 \times 10^{-6} - 2 \times 10^{-4}$	Colloid (double layer)	no	yes

The strength of cohesion arising from the attractive forces can be quantified by the granular Bond number, which is the ratio of the maximum adhesive force to the weight of the particles [19]:

$$Bo_g = \frac{F_{c,max}}{F_g} \quad (2.1)$$

This dimensional number classifies granular materials as a group of free-flowing particles for $Bo_g < 1$ and cohesive particles for $Bo_g > 1$.

2.2 GRANULAR MIXING

Despite the fact that granular materials are involved in many industrial applications, the knowledge of their mixing processes is underdeveloped when compared to for example liquid mixing. The main purpose of granular mixing or blending is to produce a mixture with an internal structure of acceptable quality. More specifically, granular mixing processes are often required to produce a high degree of homogeneity [20]. However, the segregation of particles is a fundamental challenge in achieving a homogeneous end product. A large number of other factors (such as mixing process parameters) can either stimulate or minimize segregation, making the mixing process a complex combination of various factors which must be well understood in order to produce a high quality mixture. A number of reviews on granular mixing is available in literature, as well as research publications on experimental and computational analyses regarding the mixing process in various types of mixers and the influence of material properties process parameters on the mixing effectiveness. A review of these works is presented in [20].

2.2.1 MIXING MECHANISMS

The mechanisms responsible for granular mixing are described in literature by several authors; however, the theory by Lacey [21] is most commonly cited. This theory defines the following three basic mixing mechanisms [20, 22]:

- *Convection*
This involves the transfer of clumps of adjacent particles with respect to each other by the rotational action of the mixer vessel or mixing device. This effect contributes primarily to macroscopic mixing, and the rate of mixing is large relative to the other mechanisms.
- *Shear*
This mechanism is caused by momentum exchange between groups of particles with different velocities. The particle groups move as “blocks” outside narrow regions called slip zones in which a high velocity gradient is present. This movement of particle groups enhances the breakage of inter-particle forces and hence, is responsible for the disruption of agglomerates. The amount of shear mixing is directly proportional to the surface area between mixing equipment and material in the mixer.
- *Diffusion*
This process is responsible for the mixing on the particle length scale in the mixer (microscopic homogenization). The term does not refer to molecular diffusion, but to the random dispersion of particles allowing them to move relative to each other. Although this mechanism is critical to microscopic mixing, its effect is considered to be small in comparison to the other mechanisms.

These mechanisms are governed by many factors such as the material properties, geometry of the mixer and mixing tools and the operating conditions. For example, convection and diffusion mixing are important in symmetric tumbling mixers, while convection and shearing are dominant in paddle and ribbon-blade mixers. Even by handling the same material in a single mixer, the mixing quality can be greatly affected by varying the operating conditions. An overview of some typical granular mixers is provided by Huang and Kuo [23].

2.2.2 WET GRANULAR MIXING

In many industrial processes, liquids are often added to granular materials. It is well known that the presence of liquid alters the behavior of a granular flow significantly due to the additional forces exerted on the grains by the interstitial fluid. Most wet granular studies are focused on low liquid contents compared to the grain volume, such that pendular liquid bridges are formed between the material grains [24, 25, 26]. One typical example in this regard is wet granulation, a widely used process in many industries involving the blending of dry particulate matter with a liquid binder in type of mixer usually referred to as a “granulator”. In short, wet granulation involves wetting of dry powder particles which subsequently stick to other particles by means of capillary bridge forces as they come into contact with each other (agglomeration). Thus, the product of a wet granulation process is simply a collection of larger grains. This particle enlargement method is often used when larger particles are desired because they provide better handling over the ungranulated powder. Several authors [27, 28, 29] describe wet granulation as a combination of the following three processes (Figure 2-4, left) :

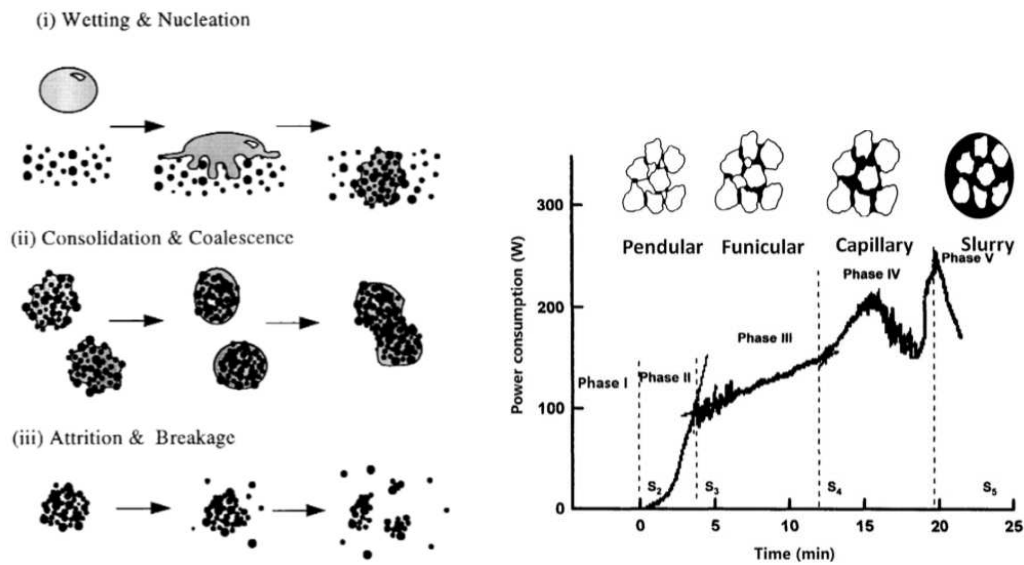


FIGURE 2-4. Processes involved in wet granulation [27] (left) and example of a power consumption curve during wet granular mixing (right).

- *Wetting and nucleation*

The process starts when liquid binder is brought into contact with the dry powders (wetting). As the mixture is transported through the granulator, the liquid is distributed through the powder and nuclei granules are formed. These processes depend on nuclei formation, which are a function of wetting thermodynamics and kinetics, and the binder dispersion, which depends on process variables.

- *Consolidation and coalescence*

Here, collisions between two granules, granules and feed powder or a granule and the processing equipment results in granule compaction and growth. During granulation, it is possible that the granules transform from the pendular state to the saturated state, either due to addition of liquid binder and/or consolidation, which decreases the granule porosity.

- *Breakage and attrition*

This refers to the breakage of wet or dried granules due to impact, wear or compaction in the granulator or during subsequent product handling.

During the mixing process, power consumption variations occur due to a change in the cohesive forces of the agglomerates and therefore, the load on the impeller reflects changes in the rheological properties of the moist mass. Hence, power measurements are often used to monitor the granulation process and identify the optimal liquid amount for agglomeration. Leuenberger et al. (1979) identified several phases in the power consumption curve, as seen in Figure 2-4. According to the authors, the optimal amount of liquid is obtained in the third phase. It has been found that the characteristic curve can be observed in most power consumption records, independently of the mixer. However, the curve depends on the material characteristics [30].

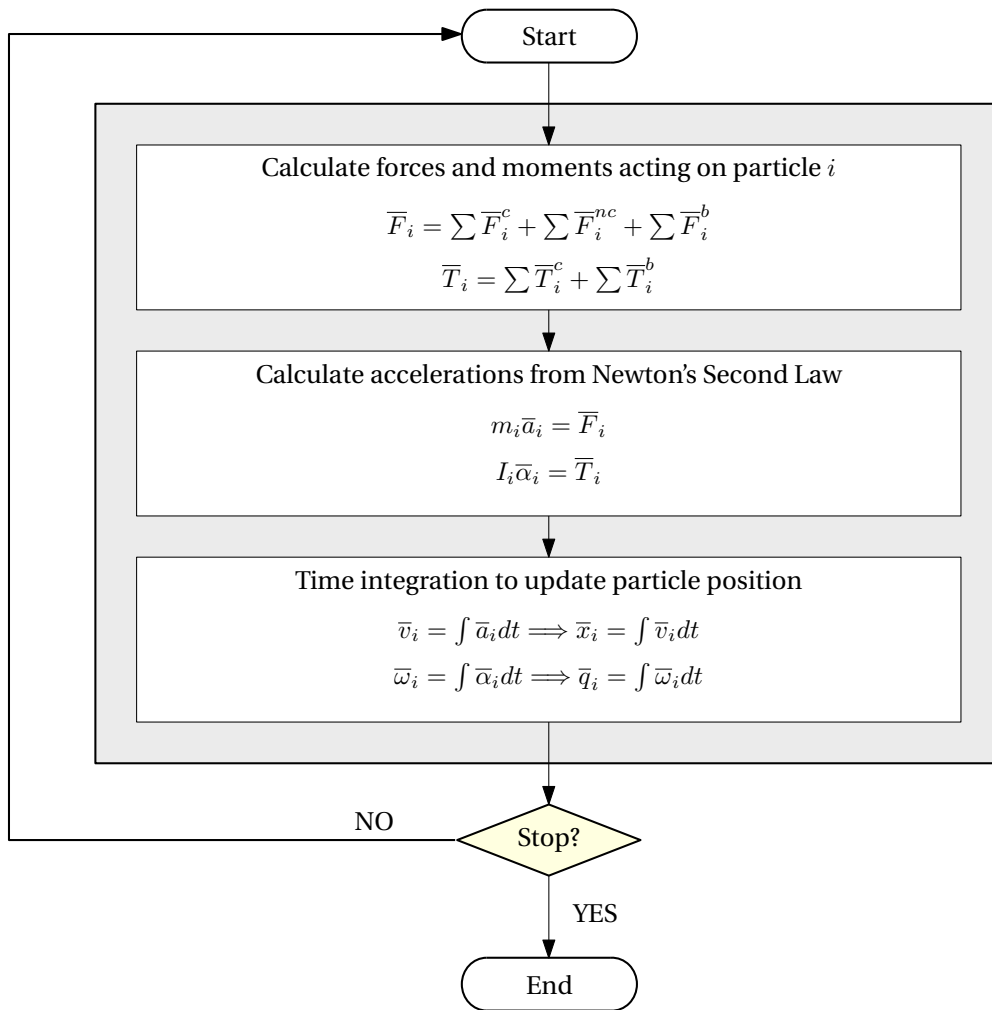


FIGURE 2-5. Schematic representation of the DEM calculation scheme at a single time step.

2.3 MODELING GRANULAR MIXTURES

The discrete element method is applied in analyses where the scale of observation requires the interaction between particles and the surrounding fluid to be taken into account, for example for phenomena such as mixing, compaction, de-airing, sedimentation etc. [31]. The aim of discrete methods is to closely study the movement, trajectories, rotation and interaction of particles. Several methods based on the discrete approach have been developed over the years. Three discrete methods are often encountered in literature: the Discrete Element Methods (DEM), Dissipative Particle Dynamics (DPD) and the Viscoplastic Suspension Element Method (VSEM). Only the DEM will be discussed in detail, since this method is used in the current study.

2.3.1 FUNDAMENTALS OF DEM

The Discrete Element Method (DEM) was first introduced by [Cundall and Strack \(1979\)](#) [32] for problems in geotechnical engineering. This method was developed in analogy to the Molecular Dynamics method, which was developed in the 1950's to study the movements of atoms of molecules

(molecular systems). The basic principle of both methods is to determine the trajectories of particles which obey Newton's equations of motion; however, DEM is generally used to simulate the behavior of macroscopic particles with dissipative interactions, while MD is concerned with energy conservation. For this reason, DEM is sometimes referred to as the "soft-particle" MD method. The basic principle of discrete particle simulations can be expressed as follows: if all the forces and torques acting on a particle are known at each time step of the simulation, then the trajectory of that particle can be predicted in time. This theory can be expressed for both translational and rotational motion of each particle i using Newton's second law:

$$\sum \vec{F}_i = m_i \vec{a}_i = m_i \frac{d\vec{v}_i}{dt} \quad (2.2a)$$

$$\sum \vec{T}_i = I_i \vec{\alpha}_i = I_i \frac{d\vec{\omega}_i}{dt} \quad (2.2b)$$

Each particle inside the system is subjected to various contacts, such as interactions with neighboring particles, the system walls and the surrounding fluid. Thus, a variety of forces affects the particles' motion, as shown in Figure 2-5. Thus, the left-hand side of Eq. (2.2a) and (2.2b) can be expressed as, respectively:

$$\sum \vec{F}_i = \sum_{j=1}^{N_p} \vec{F}_{ij}^c + \sum_{k=1}^{N_w} \vec{F}_{ik}^c + \sum_{j=1}^{N_p} \vec{F}_{ij}^{nc} + \sum_{k=1}^{N_w} \vec{F}_{ik}^{nc} + \vec{F}_i^b \quad (2.3a)$$

$$\sum \vec{T}_i = \sum_{j=1}^{N_p} \vec{T}_{ij}^c + \sum_{k=1}^{N_w} \vec{T}_{ik}^c + \sum_{j=1}^{N_p} \vec{T}_{ij}^{nc} + \sum_{k=1}^{N_w} \vec{T}_{ik}^{nc} + \vec{T}_i^b \quad (2.3b)$$

where

- \vec{F}_{ij}^c and \vec{T}_{ij}^c are the contact force and torque acting on particle i due to particle j
- \vec{F}_{ij}^{nc} and \vec{T}_{ij}^{nc} are the non-contact force and torque acting on particle i due to particle j
- \vec{F}_{ik}^c and \vec{T}_{ik}^c are the contact force and torque acting on particle i due to wall k
- \vec{F}_{ik}^{nc} and \vec{T}_{ik}^{nc} are the non-contact force and torque acting on particle i due to wall k
- \vec{F}_i^b and \vec{T}_i^b are the body force and torque acting on particle i
- N_p is the number of particles in the system
- N_w is the number of walls making up the system geometry

In wet granular matter, all of the above interactions are present. While the body forces and torques are easily determined using familiar physics laws, the computation of short and long-range interaction forces and torques requires careful consideration of the particle-particle and particle-wall interaction phenomena. Several interaction models have been developed in literature and the suitable models applicable to this study are presented in Section 3. In the following, the concept of particle contact and contact forces (and torques) is introduced briefly.

In the DEM, particles are allowed to overlap with surroundings objects upon contact as shown in Figure 2-6. Whether a particle is in contact with its neighbors depends on its position within the frame of reference, relative to the positions of its neighbors. A particle is defined in space by its center-of-mass position (\vec{r}), while a flat wall is identified by its inward normal (\vec{n}_w) and a point on the

wall (\vec{p}_w). By definition, two objects are in contact only when $\delta^n > 0$, where δ^n is the overlap between the objects in normal direction. Once a particle overlaps with another object, a force is activated at the contact. Various models have been developed for computing the contact force; these models are often referred to as “contact laws”. The contact laws aim to mimic the interaction behavior of real particles, and are only valid when small contact deformations occur. In assuming small deformation areas, the contact can be represented by a single contact point \vec{c} in the middle of the contact area. It is important to realize that the forces and torques which are assumed to act at this contact point are actually derived from integrating the stress over the actual contact area [33]. The equations for computing the overlap and contact point are given in Table 2-5 for both particle-particle interaction and particle-wall interaction.

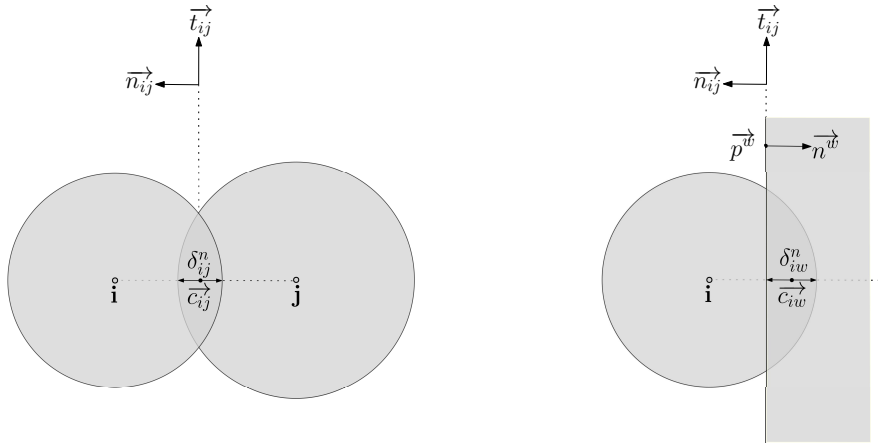


FIGURE 2-6. Left: contact parameters for a collision between two particles defined by their center-of-mass positions; right: contact parameters for a collision between a particle and a wall which is defined by an inward normal and a point on the wall, adapted from [33].

TABLE 2-5. Equation sets for determining the overlap and contact point in particle-particle interaction and particle-wall interaction.

Particle-particle interaction parameters	$\vec{c}_{ij}^c = \vec{r}_i - (a_i - \delta_{ij}/2) \vec{n}_{ij}^c$	(2.4)
	$\delta_{ij}^n = (a_i + a_j) - (\vec{r}_i - \vec{r}_j) \cdot \vec{n}_{ij}^c$	(2.5)
	$\vec{n}_{ij}^c = \vec{r}_{ij} / \vec{r}_{ij} $	(2.6)
	$\vec{r}_{ij}^c = \vec{r}_i - \vec{r}_j$	(2.7)
Particle-wall interaction parameters	$\vec{c}_{iw}^c = \vec{r}_i - (a_i - \delta_{iw}/2) \vec{n}_{iw}^c$	(2.8)
	$\delta_{iw}^n = a_i - \vec{n}_w \cdot (\vec{r}_i - \vec{p}_w)$	(2.9)
	$\vec{n}_{iw}^c = -\vec{n}_w$	(2.10)

The contact force (\vec{F}_{ij}^c in case of particle-particle interaction and \vec{F}_{iw}^c in case of particle-wall interaction) can generally be decomposed into a normal ($\vec{F}_{ij}^{c,n}$) and a tangential ($\vec{F}_{ij}^{c,t}$) component, as shown in Figure 2-7. In general, the contact forces and torques acting on particle i , from particle j , are written as, respectively:

$$\vec{F}_{ij}^c = \vec{F}_{ij}^{c,n} + \vec{F}_{ij}^{c,t} \quad (2.11)$$

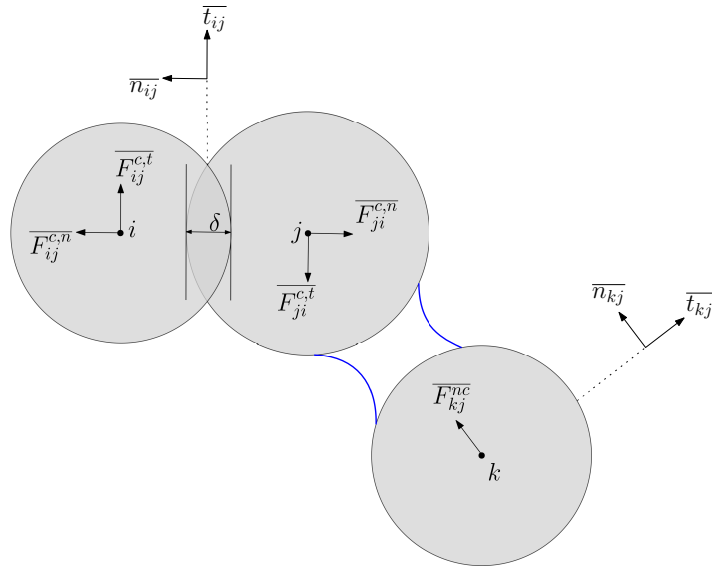


FIGURE 2-7. Illustration of two colliding particles i and j and two non-contacting particles j and k , and the resulting contact forces acting upon them.

$$\vec{T}_{ij}^c = \left(\vec{r} \times \vec{F}_{ij}^{c,t} \right) + \vec{T}_{ij}^{r\delta} + \vec{T}_{ij}^{to} \quad (2.12)$$

where the normal and tangential components are given by:

$$\vec{F}_{ij}^{c,n} = F_{ij}^{c,n} \vec{n}_{ij} \quad (2.13a)$$

$$\vec{F}_{ij}^{c,t} = F_{ij}^{c,t} \vec{t}_{ij} \quad (2.13b)$$

Both contact and non-contact forces (and torques) are described extensively in literature and are further discussed in Section 3 for the current study. In order to ensure that the contact forces and torques are objective (i.e., they are independent of the frame of reference), the relative velocity \vec{v}_{ij} , and therefore the relative displacement, is decomposed into four components: two translational velocities and two angular velocities as shown in Figure 2-8. They are given as follows.

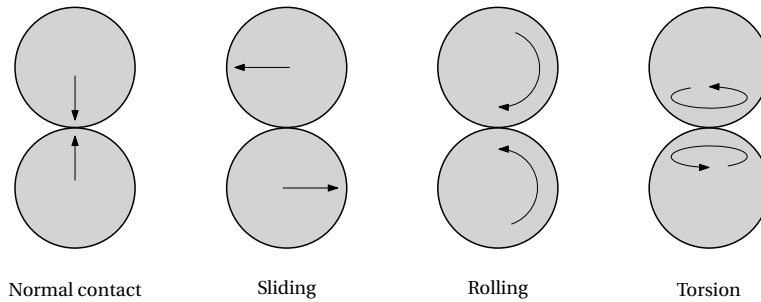


FIGURE 2-8. Schematic illustration of two colliding particles, i and j , and the resulting contact forces acting upon them.

TABLE 2-6. Equation sets for determining the normal, sliding, rolling and torsion contact velocities.

Corrected particle radii	$a'_\alpha = a_\alpha - \delta/2 \quad (\alpha = i, j)$	(2.14)
	$a_{eff} = a_i a_j / (a_i + a_j)$	(2.15)
	$a'_{eff} = a'_i a'_j / (a'_i + a'_j)$	(2.16)
Relative velocity	$\vec{v}_{ij} = \vec{v}_i - \vec{v}_j + a'_i \vec{n}_{ij} \times \vec{\omega}_i + a'_j \vec{n}_{ij} \times \vec{\omega}_j$	(2.17)
Normal relative velocity	$\vec{v}_{ij}^n = -\vec{v}_{ij} \cdot \vec{n}_{ij}$	(2.18)
Lateral sliding velocity	$\vec{v}_{ij}^t = \vec{v}_{ij} - \vec{n}_{ij} (\vec{n}_{ij} \cdot \vec{v}_{ij})$	(2.19)
Rolling velocity	$\vec{v}_{ij}^{r\sigma} = a'_{eff} (\vec{n}_{ij} \times \vec{\omega}_i - \vec{n}_{ij} \times \vec{\omega}_j)$	(2.20)
Torsion velocity	$\vec{v}_{ij}^{t\sigma} = a_{eff} (\vec{n}_{ij} \cdot \vec{\omega}_i - \vec{n}_{ij} \cdot \vec{\omega}_j) \vec{n}_{ij}$	(2.21)

As discussed in Section 2, the grains of a granular material have a dissipative character. Contrary to molecular systems, the particles lose energy during each collision. Thus, in order to keep a granular material in steady or periodic motion, the grains must be agitated externally. In order to quantify the amount of energy which is irreversibly lost during a head-on collision, the normal restitution coefficient is defined as

$$\epsilon^n = -\frac{v_{ij}^{n'}}{v_{ij}^n} \quad (2.22)$$

which is the ratio between the post-collisional and pre-collisional normal relative velocities. From the definition it is clear that $0 \leq \epsilon^n \leq 1$, where $\epsilon^n = 1$ would be applicable to a fully elastic collision.

2.3.2 MIXING CHARACTERIZATION

For continuous mixers, the change in homogeneity in axial direction is an important parameter to study. Ghaderi [34] states that, in general, mixing action is caused by radial mixing –responsible for the intermingling of the parallel streams– and axial mixing, which causes smoothing-out of the time-based fluctuations in the effective composition of the input. Since the radial direction is usually much smaller than the length of the mixer, the contribution of heterogeneity along the axial direction is far greater than in the radial direction, and therefore, continuous mixers are usually characterized by their ability to smoothing out ingoing fluctuations (axial mixing).

DEM simulations are particularly suitable for determining the the quality of a granular mixture since various details such as particle positions at any time can be obtained accurately. The particle mixing index provides a means to characterize the mixture quality in simulations. However, many definitions of the mixing index are provided by different researchers in literature [35]. Most of the described methods deal with binary mixtures consisting of two constituents and are based on statistical analyses. Mixture homogeneity is usually quantified by the variance of the distribution of the compositions of N samples of a whole mixture, μ being the mean composition and x_i the composition in sample i [36]:

$$\sigma^2 = \frac{1}{N} \sum_{i=1}^N (x_i - \mu)^2 \quad (2.23)$$

with

$$\mu = \frac{1}{N} \sum_{i=1}^N x_i \quad (2.24)$$

For batch mixers, the samples are typically retrieved throughout the powder bed while for continuous

mixing, the mixture can be analyzed at the outlet [36, 37, 38] and along the axis of rotation [39]. The main challenge in this methods is the sampling, as the scale of scrutiny (sample size) largely affects the obtained value of mixture quality. Other methods described in literature employ tracking of particles throughout the mixer in relation to their neighbors. Wen et al. [40] conducted a comparative study on several different methods by determining the defined mixing indices using DEM simulation results. One of the simplest methods to implement was found to be the *nearest neighbor method*, a grid-independent method which will also be employed here. This method is described as follows. In a binary mixture, half of the particles are of one species and the rest is of a different species. The twelve nearest neighbors of each particle are recorded in time. If these particles have the same species as the particle under investigation, the material is considered to be unmixed. If more than half of the nearest neighbors are of the other species, it is fully mixed. The overall mixing index can then be determined as the average over all particles [41]:

$$M = \frac{1}{N_p} \sum_{N_p} \frac{2n_{diff}}{n_{nb}} \quad (2.25)$$

where N_p is the number of particles, n_{diff} is the number of particles with a different species than the particle under investigation and n_{nb} is the number of nearest neighbors.

2.4 OVERVIEW OF SCREW CONVEYOR MIXING STUDIES

The mixing behavior of any products is determined by a combination of mixer design (dimensions), mixing products (material properties) and mixing operation (rotational speed, filling fraction, feeding order etc.). Several studies are available in literature on mixing analyses of granular flows in industrial processing equipment as a function of these parameters. While most mixing studies –both numerical and experimental– are performed for batch mixers [42, 43, 44, 45, 46, 47, 48, 49, 50, 51, 52, 53, 54], continuous blenders, more specifically screw-type blenders, have been analyzed to a lesser extent. In the following, a brief summary of literature findings on the relevant parameters during continuous granular mixing is presented.

2.4.1 ANALYSES ON THE EFFECTS OF MATERIAL PROPERTIES

Cleary et al. [55] and Yu et al. [56] studied the flow of non-cohesive and cohesive particles from a hopper/bin into a screw conveyor, respectively. In both studies it was found that friction is an important factor in the particle draw-down and flow behavior. The second study also showed that the presence of cohesive forces in the material significantly alters the flow behavior. Different states of the flow are observed as cohesion increases: for cohesionless particles, there is a continuous flow of particles from the hopper into the screw casing. As the cohesive force increases up to a certain value, the flow becomes intermittent as it becomes difficult for the particles to fill the voids created by the screw. For very high cohesion, the material is solid-like and heavily resists perturbation of the screw blade.

Orefice and Khinast [57] observed the effect of particle-conveyor friction for a system of dry particles. It was found that the volume throughput is inversely proportional to the relative friction coefficient. As the friction coefficient increases, the relative tangential velocity of the particles with respect to the screw surface approaches zero. Pezo et al. [58, 59] also studied the flow of dry particles

in a screw conveyor; however, the authors briefly state that the particle velocities (both axial and tangential components) are invariant to changes in particle-wall friction without substantiating their claim.

2.4.2 ANALYSES ON THE EFFECTS OF EQUIPMENT DESIGN

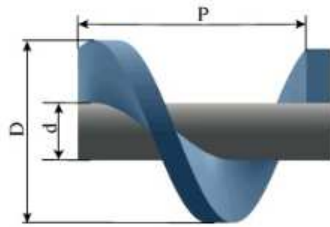
Tsai and Lin [60] performed experiments using a screw feeder for various screw dimensions and shapes. In general, the most important screw dimensions are the screw diameter D , the pitch diameter $D - d$ and the pitch P as shown in Figure 2-9a. The authors found that increasing the screw diameter, flight diameter, flight thickness or decreasing the pitch may increase the degree of mixing of the screw feeder. On the other hand, the degree of mixing is reduced for lower values of d .

Tanida et al. [61] studied cohesionless particle transport and mixing in a screw feeder for different screw designs in which the ratio of screw pitch P to screw diameter D was varied. For small values of P/D , the flow rate is proportional to this fraction and decreases as the ratio becomes larger. The rate of mixing increases rapidly with increasing P/D in small ranges of this ratio.

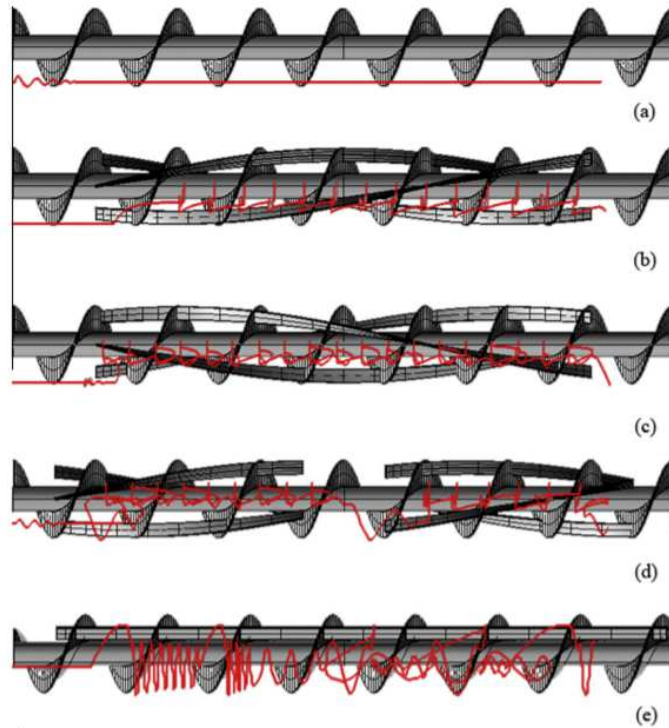
Pezo et al. [58, 59] altered the design of a single flight screw conveyor's blade by inserting additional helix or helical strips, on the periphery of the helix, in the same or opposite direction of material flow. It was concluded that the transporting path of dry particles in the conveyor mixer can be prolonged significantly by addition of these elements. While the retention time remains constant, the particle velocities increase significantly. The particle trajectories of tracer particles are shown in Figure 2-9b for various designs of the screw conveyor blade. Simulations reveal that the particle path is nearly a straight line in the starting case (a), which is a typical design for screw conveyors. The particle trajectories become more complex for modified designs, thereby increasing the probability of particles being mixed during the transport.

2.4.3 ANALYSES ON THE EFFECTS OF OPERATING CONDITIONS

The most studied operating conditions are the rotation speed of the shaft and the filling fraction of particles in the trough. Shi et al. [63] modeled the contact forces occurring between dry particles in a screw conveyor for different rotation speeds. Their simulation results show that the average normal forces are stronger than the average tangential forces at the same moment. Also, the average contact force appears to be highest at the lowest rotation speed in their study. According to the authors, this is due to the average particle overlap being highest at the lowest rotational speed. On the contrary, Wang et al. [64] state that the rotation speeds increase the axial particle velocity, mass flow rate and contact forces between dry particles while the axial particle velocity decreases with filling level. Neither of the two authors studied the mixing efficiency. Heindel et al. [62] studied the effects of screw rotation speed on the mixing index for a dry, multicomponent mixture in a double screw mixer. It was concluded that screw rotation speed had negligible impact on the mixing degree for a fixed filling fraction and fixed geometry of the screw.



(a)



(b)

FIGURE 2-9. (a) Relevant dimensions of a basic screw-conveyor mixing element with flight diameter D , flight pitch P and shaft diameter d , courtesy of [62]; (b) Particle trajectory of a tracer particle for various designs of the mixing element, courtesy of [58].

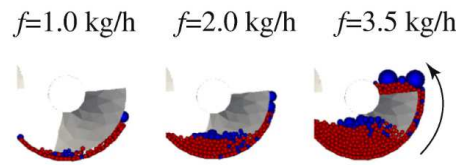


FIGURE 2-10. Illustration of how the feed rate effects the filling level relative to the shaft, courtesy of [62].

In the previously mentioned study by [Tanida et al. \[61\]](#) on cohesionless particle mixing in a screw feeder, the authors also focus on the effect of filling fraction. The authors state that particle mixing in a screw conveyor is activated by the transverse motion over the center shaft. This motion becomes restricted as the filling fraction increases over a value of 0.5. It was found that both coefficient of mixing and transport rate decay for higher filling levels. [Pezo et al. in \[58, 59\]](#) also support the claim of maintaining a maximum filling fraction of 0.5, in order to provide the particles with enough space where additional mixing action can occur during transport. Rather than analyzing the effect of filling fraction on mixing behavior, [Orefice and Khinast \[57\]](#) focused on the conveying efficiency, which is defined as the ratio of the mean volume throughput to the mean maximum throughput. Notably, the authors mention that maximum efficiency is also achieved for a filling fraction of roughly 0.5. However, in the study by [Heindel et al. \[62\]](#), it was found that decreasing the solid particle feed rate too much results in a decreased mixing degree and increased segregation in the transverse section, possibly as a result of free space under the shaft. The authors state that when the feed rate is high enough (such that the particle filling level reaches the shaft), then some particles are lifted up by the screw flight and are transferred across the shaft to the other side of the tube, a flow pattern seems to disappear for (too) low feed rates. This seems to correspond with the findings of [Tsai and Lin \[60\]](#), where it was found that increasing the shaft size results in enhanced mixing.

In summary, the described studies demonstrated the use of DEM to facilitate screw (re)design by analyzing particle movements and interactions. Although DEM has shown a lot of potential in granular mixing analysis, most of the previous studies are limited to mono-disperse, single-component and dry particle systems. Also, only a limited amount of research has included the aspect of mixing quantification in screw conveyor/mixers systems.

3

MODEL DEVELOPMENT

INTRODUCTION

As discussed in the previous section, the Discrete Element Method is used to model a granular medium as a set of rigid particles subjected to translational and rotational movements due to interactions with their surroundings. This section presents the mathematical models for determining particle and liquid migration during the dry-mixing process. A systematic approach is taken to formulate the governing equations. First, the system and the relevant phenomena occurring therein are described in detail. Next, the goal of the model and the level of detail which will be included are clearly stated, as these aspects set the basis for which outputs should be generated and hence, which equations should be formulated. After presenting the governing equations, the computer implementation is discussed.

3.1 SYSTEM AND RELEVANT PHENOMENA

Recall the concrete production system as shown in Figure 1-3. The mixer is in principle a combination of a dry-mixing unit and a wet-mixing unit (Figure 3-1). The dry-mixing unit is basically a screw conveyor system with a dual function: i) to transport the dry ingredients from the hopper to the wet-mixing unit at controlled and steady rates and ii) to perform some premixing action of the sand, cement and other dry ingredients before wet-mixing, where the goal is to achieve even wetting of the dry material and a homogeneous distribution of the constituents.

At the beginning of the dry-mixing process, the solid constituents (sand, cement, limestone, fly ash, silica fume) are added to the system. In the dry state, cement particles are cohesive due to the presence of electrostatic and van der Waals interparticle forces. Rather than dispersing into the sand, the cement particles form weak solids (multiparticle clumps) [65]. On the other hand, the sand particles naturally contain a certain amount of moisture; hence, the material is actually not “dry” and the sand particles can transfer moisture to the other powders during this so-called dry-mixing stage. The particles interact with each other and the system walls, allowing them to travel from the inlet to

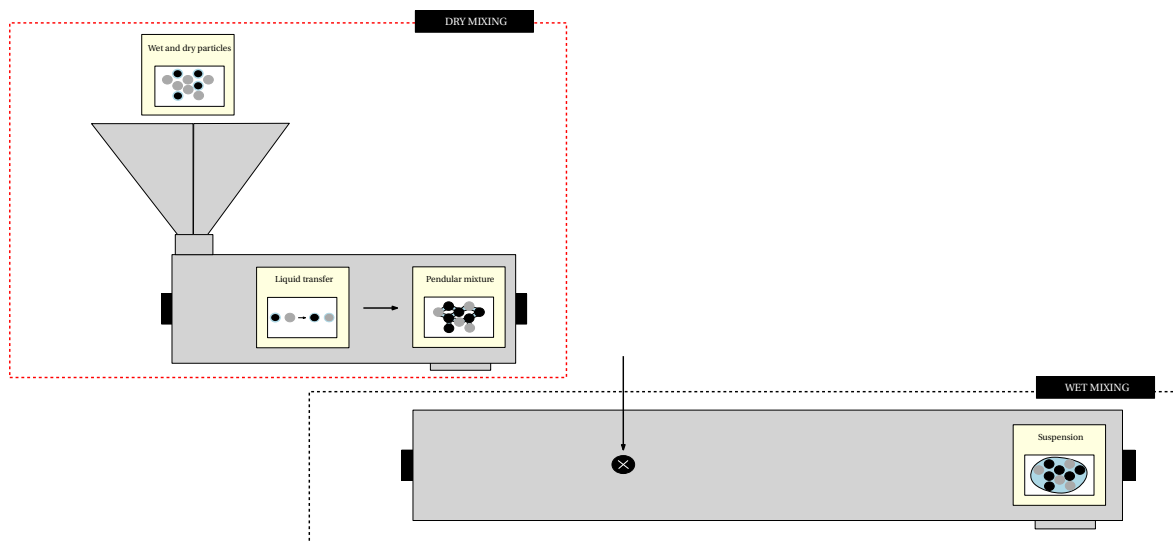


FIGURE 3-1. Schematic illustration of the complete mixing system, consisting of a dry-mixing unit and a wet-mixing unit. The arrow indicates the point of water injection to the system.

the outlet of the system. The type of interactions occurring between contacting particles in general depends their moisture content at the time of contact. Three inter-particle interactions are possible:

1. Contact between dry particles

When a particle comes into contact with a neighboring object (another particle or a wall), contact forces and torques are generated at the contact point, as discussed in Section 2.3.1. The forces are repulsive and dissipative in nature, leading to rebound of the particles after impact (a change in the direction of motion) accompanied by energy loss.

2. Contact between wet particles

When moist solid particles come into contact, the repulsive contact forces and torques are generated at the contact point and the particles' liquid volume is transferred into a liquid bridge which connects the particles. The liquid bridges exert attractive forces between particles causing them to resist gravitational and shear forces which tend to tear them apart [66]. When the particles are agitated, they start to move away from each other such that the distance between the particle surfaces becomes larger and the liquid bridge becomes thinner. The magnitude of the adhesive force decreases as the distance between the particles increases. At some critical separation distance (the "rupture" distance), the liquid bridge will break at the thinnest part and the liquid on either half of the broken bridge must be allocated to the individual particles.

3. Contact between dry and wet particles

In this case, the liquid stored in the thin film of the wet particle is partly absorbed by the dry particle, thereby creating a new wet particle. A certain amount of liquid volume ($V_{L_{min}}$) is trapped and remains fixed in the particles once they become wet. A particle's moisture content must therefore be larger than or equal to $V_{L_{min}}$ in order to transfer liquid to other particles.

3.2 OBJECTIVE & SCOPE

With reference to Section 1, there is a clear need for an extensive model which can predict the distribution of the solid grains and liquids in the mixer for various geometries, as the material travels from the inlet to the outlet. Since the mixture evolves from a dry granular material at the start of dry-mixing to a suspension at the end of wet-mixing, the complete model should ultimately be able to simulate the entire range of saturation levels from the dry state to the fully saturated state. A model of this extent has already been developed and tested by Krenzer [9] using the software package EDEM as a doctoral research project. Given the time which is available for the current study, the scope of the model is restricted to the dry-mixing unit where it is assumed that the liquid content is so low such that the mixture remains in the pendular regime. Hence, the goal of the model in this study is to assess the degree of mixing in the dry-mixing unit enclosed by the red dotted lines in Figure 3-1.

The basic idea is to develop a DEM model which accounts for particle-particle and particle-wall interactions depending on the moisture state of the particles. This includes on the one hand the application of a suitable contact model and on the other hand the realization of liquid transfer between contacting objects at each time step. At this stage, the only adhesive forces taken into consideration are those due to liquid bridges (capillary adhesion). The software package MercuryDPM is employed to perform the simulations using a special type of particle package, the “liquid film particle” which allows the user to assign liquid to spherical particles, as shown in Figure 3-2. MercuryDPM currently offers a wide variety of contact models and a liquid migration model which may be combined to describe the phenomena occurring within the system.

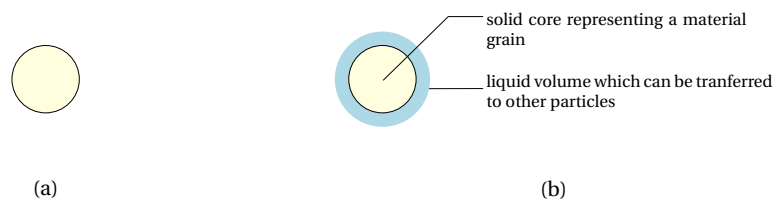


FIGURE 3-2. Different types of particles: (a) dry solid particle, (b) wet particle with a solid core and a surrounding (virtual) liquid film layer which can increase or decrease in volume through interactions with the surrounding particles.

3.3 PHYSICAL MODEL FORMULATION

3.3.1 CONTACT MODELS

Recall from Section 2.1.2 that forces acting on particles can arise due to short-range interactions (collisions between particles, or particles and walls), body forces and long-range interactions. In wet granular matter, all of these interactions are present. While the body forces and torques are easily determined using familiar physics laws, the computation of short and long-range interaction forces and torques requires careful consideration of the particle-particle and particle-wall interaction phenomena. The models applicable to this study are presented in the following.

3.3.1.1 BODY FORCES

The body force on each particle i is the gravitational force:

$$F_i^b = m_i g \quad (3.1)$$

with

$$m_i = V_i \rho_i = \left(\frac{4}{3} \pi a_i^3 \right) \rho_i \quad (3.2)$$

3.3.1.2 CONTACT FORCES AND TORQUES

Normal forces are always considered when describing contacts, as particles would “fly” through each other if they were not active. For the tangential degrees of freedom, there are three different interaction laws to be considered [67]: i) friction (sliding resistance), ii) rolling resistance and iii) torsion resistance. There are various models to calculate the contact forces for these interactions, with the simplest model being the Linear Spring Dashpot (LSD) model. Generally, the force is a combination of two basic components: a linear elastic repulsive force ($k \delta_{ij}$) due to which the particles repel each other, and a linear dissipative force which acts in the direction opposite to their relative velocity (γv_{ij}) during particle contact, allowing for energy dissipation. These interactions are determined based on the normal, sliding, rolling and torsion velocity discussed previously (Table 2-6) and they all follow a similar force calculation routine, as shown in Figure 3-3. For the tangential degrees of freedom, the forces are used to calculate moments. Unlike the tangential force, the rolling and torsion forces are not actually present but simply facilitate the calculation of the moments.

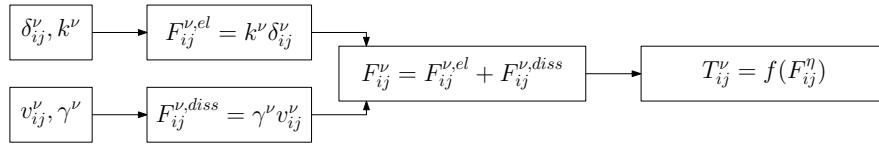


FIGURE 3-3. Subroutine for calculating contact interaction forces and torques from the corresponding input parameters. The subroutine is the same for calculating all interaction forces, hence, in the notation $\nu = n, t, ro, to$. The moments are only calculated from the tangential, rolling and torsion forces, hence, $\eta = t, ro, to$.

Each of the three tangential forces/torques is also limited by a yield criterion. In the case of the tangential force (Figure 3-4), the surface contact shears and the particles slide over each other when the ratio of the tangential to the normal force exceeds the static sliding friction coefficient μ^{ss} . The tangential force then decreases until the ratio becomes small than or equal to the dynamic sliding contact friction coefficient μ^s . The same analogy applies to the rolling and torsion forces. While the static coefficient of friction is generally larger than the dynamic coefficient, a single friction coefficient is often assumed, i.e., $\mu^{ss} = \mu^s$. Similarly, the rolling- (and torsion)-to-normal-force are bounded by rolling and torsion friction coefficients, respectively. The equation set for calculating the normal and tangential degrees of freedom is presented in Table 3-1.

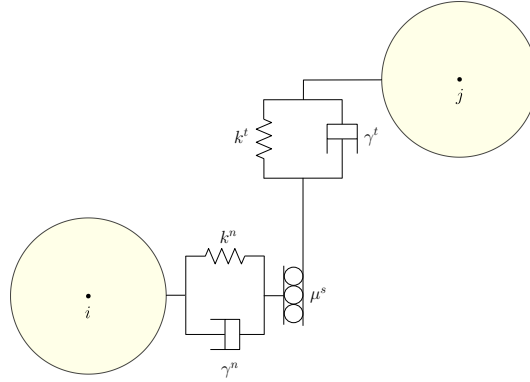


FIGURE 3-4. Example of two particles, i and j , which can interact through the LSD model with sliding friction.

TABLE 3-1. Equation set for the LSD normal and tangential force model.

Model equations	$\vec{F}_{ij}^{c,n} = k^n \vec{\delta}_{ij}^n + \gamma^n \vec{v}_{ij}^n$	(3.3)
	$\vec{F}_{ij}^{c,t} = \min(\mu^s \vec{F}_{ij}^{c,n}, k^t \vec{\delta}_{ij}^t + \gamma^t \vec{v}_{ij}^t)$	(3.4)
	$F_{ij}^{c,ro} = \min(\mu^{ro} \vec{F}_{ij}^{c,n}, k^{ro} \vec{\delta}_{ij}^{ro} + \gamma^{ro} \vec{v}_{ij}^{ro})$	(3.5)
	$F_{ij}^{c,to} = \min(\mu^{to} \vec{F}_{ij}^{c,n}, k^{to} \vec{\delta}_{ij}^{to} + \gamma^{to} \vec{v}_{ij}^{to})$	(3.6)
Input variables	$\vec{r}_i, \vec{r}_j, \vec{v}_i, \vec{v}_j$	
Parameters	$a_i, a_j, k^n, k^t, k^{ro}, k^{to}, \gamma^n, \gamma^t, \gamma^{ro}, \gamma^{to}$	

3.3.1.3 NON-CONTACT FORCES

As previously discussed, liquid bridges are formed between particles when liquid is present in the material. Once the bridge is formed, a cohesive (capillary) force F^{cp} acts in the normal direction. This force remains active even after the particles separate, until a critical distance S_{crit} is reached, at which point the liquid bridge ruptures (Figure 3-5).

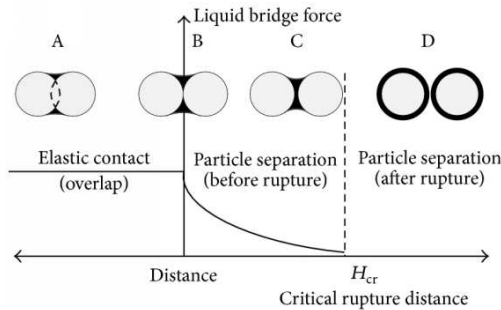


FIGURE 3-5. Illustration of liquid bridge formation and rupture depending on the distance between two wet particles.

If two spherical particles are connected by a liquid bridge as shown in Figure 3-6, the capillary force acting on each particle is essentially caused by: i) the interfacial surface tension at the liquid-gas-solid contact line and ii) the difference in hydrostatic pressure across the liquid-gas interface that develops from the interface curvature. Several authors have derived expressions for the capillary force by taking these contributions into account; a good summary can be found in [66]. For sake of brevity, only the final expression of $F_{ij}^{cp,n}$ proposed by Willett et al. will be considered as a function of the particles' specifications, liquid properties and moisture content in the system.

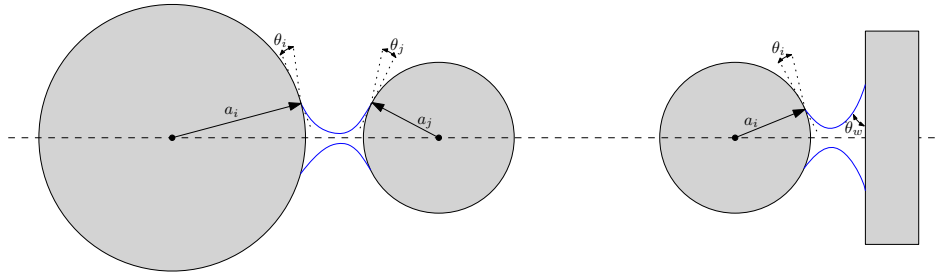


FIGURE 3-6. Illustration of a liquid bridge between two particles (left) and a particle and wall (right).

TABLE 3-2. Equation set for the liquid bridge (capillary) force model by Willett.

Model equations	$F_{ij}^{cp,n} = \frac{F_{ij}^{cp,max} \left(\frac{a_{ij}^{eff}}{a_{ij}^m} \right)}{1 + 1.05\bar{S} + 2.5\bar{S}^2}$	(3.7)
	$F_{ij}^{cp,max}(S=0) = 2\pi a_{ij}^m \sigma \cos \theta_{ij}^{eff}$	(3.8)
	$F_{iw}^{cp,max}(S=0) = 4\pi a_i \sigma \cos \theta_{iw}^{eff}$	(3.9)
	$a_{ij}^m = 2a_{ij}^{eff}$	(3.10)
	$a_{ij}^{eff} = \frac{a_i a_j}{a_i + a_j}$	(3.11)
	$\theta_{ij}^{eff} = \frac{\theta_i + \theta_j}{2}$	(3.12)
	$\theta_{iw}^{eff} = \frac{\theta_i + \theta_w}{2}$	(3.13)
	$\bar{S} = S \sqrt{\left(a_{ij}^m / V_b^{ij} \right)}$	(3.14)
	$S = \max(0, \vec{r}_i - \vec{r}_j - (r_i + r_j))$	(3.15)
	$S_{crit} = \left(1 + \frac{\theta}{2} \right) V_b^{1/3}$	(3.16)
	$V_{ij}^b = \min \left(V_f^i + V_f^j, V_{LB}^{max} \right)$	(3.17)
	$V_{iw}^b = \min \left(V_f^i, V_{LB}^{max} \right)$	(3.18)
Input variables	\vec{r}_i, \vec{r}_j	
Parameters	$a_i, a_j, \theta_i, \theta_j, \theta_w, \sigma, V_{LB}^{max}$	

In summary, both the contact forces and the cohesive liquid bridge force are taken into account for contacting particles. If a liquid bridge is formed between separated particles, only the liquid bridge force is considered. The calculation scheme is presented in the following figure.

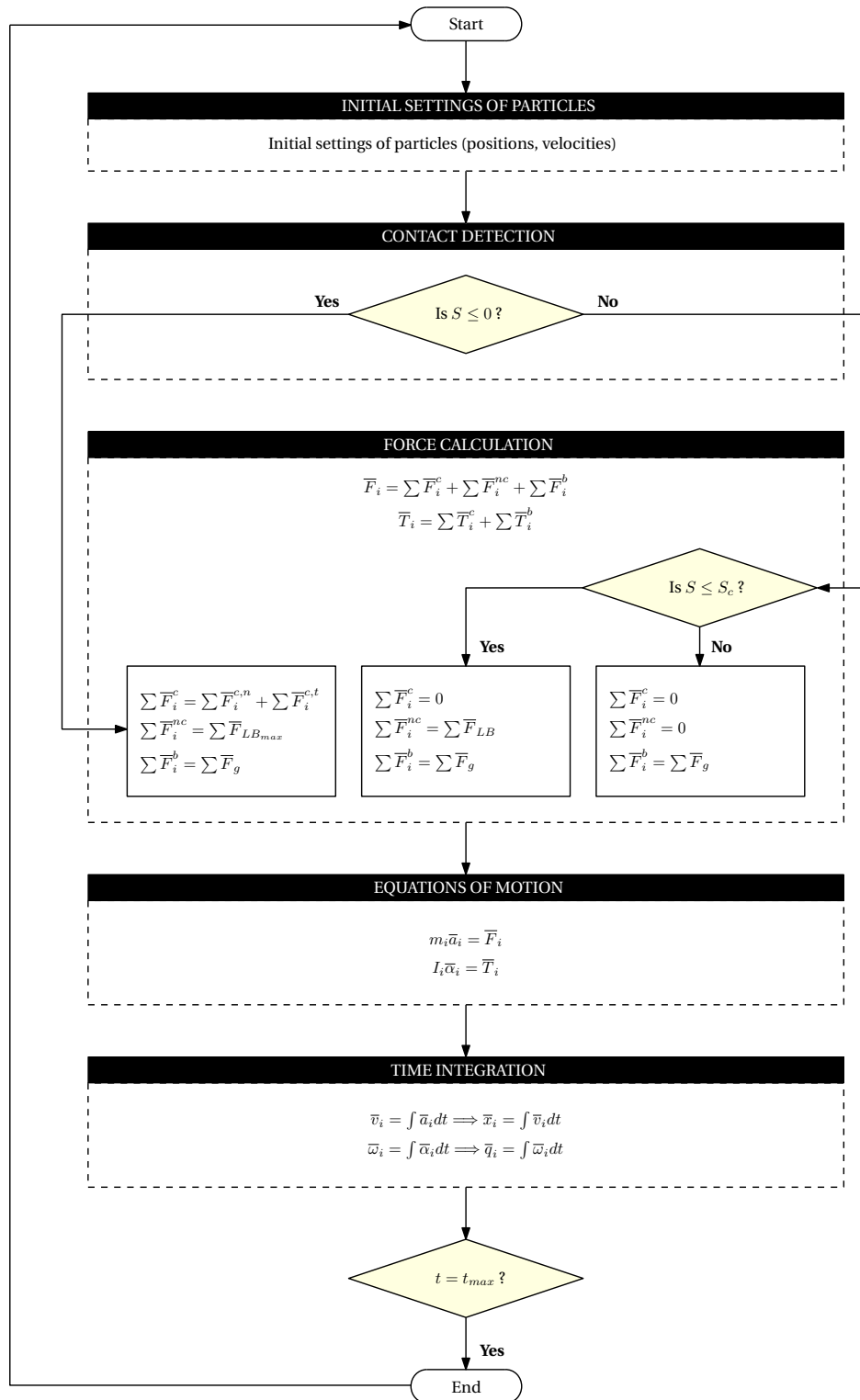


FIGURE 3-7. DEM calculation scheme used for the model.

3.3.2 LIQUID MIGRATION MODEL

The first liquid dispersion model used in DEM where liquid is redistributed upon inter-particle contact was proposed by [Shi and McCarthy \[68\]](#). In this model, it is assumed that liquid is always evenly distributed on the surface of individual particles, meaning that the liquid which is redistributed upon liquid bridge rupture is instantaneously spread over the entire particle surface. [Mani et al. \[69\]](#) also developed a simple redistribution model based on this assumption. A more advanced model developed by [Washino et al. \[70\]](#) captures the contact dispersion more accurately by allowing for partial wetting of individual particle surfaces. A comparison of this model to the results of Shi and McCarthy suggests that the assumption of even liquid distribution is valid when using relatively low viscous liquids as interstitial fluid, for example water at 20 °C. The model proposed by Mani et al. is currently available in MercuryDPM.

3.3.2.1 LIQUID BRIDGE FORMATION

The amount of liquid which is available to form a liquid bridge between two particles i and j depends on their moisture content, V_L^i and V_L^j , respectively. As discussed in Section 3.1, a certain amount of liquid (V_{Lmin}) remains trapped inside each particle and a particle's liquid volume must be larger than V_{Lmin} to contribute to liquid bridge formation. Hence, three scenarios are possible when determining the available liquid for bridge formation (the “distributable” liquid volume), as shown in Table 3-3. In the first case, the contacting particles have not yet reached the minimum liquid content, hence no liquid bridge is formed. In the second case, only one of the partners can contribute to bridge formation while in the last case, both particles provide liquid to the bridge.

TABLE 3-3. The different possible values of the distributable liquid volume (V_D), based on the moisture content of the particles between which a liquid bridge can be formed.

	Particle i	Particle j	Distributable liquid volume
CASE 1	Dry/moist state $V_L^i \leq V_{Lmin}^i$	Dry/moist state $V_L^j \leq V_{Lmin}^j$	$V_D = 0$
CASE 2	Dry/moist state $V_L^i \leq V_{Lmin}^i$	Wet state $V_L^j > V_{Lmin}^j$	$V_D = V_L^j - V_{Lmin}^j$
CASE 3	Wet state $V_L^i > V_{Lmin}^i$	Wet state $V_L^j > V_{Lmin}^j$	$V_D = (V_L^i - V_{Lmin}^i) + (V_L^j - V_{Lmin}^j)$

Although the amount of liquid that can be transferred to a liquid bridge is in theory equal to V_D , a liquid bridge limit is imposed in the model to avoid liquid clustering. Thus, the liquid bridge volume V_{LB}^{ij} is:

$$V_{LB}^{ij} = \min(V_D, V_{LBmax}) \quad (3.19)$$

where the limiting value V_{LBmax} is determined by

$$V_{LBmax} = \beta r_p^3 \quad (3.20)$$

and the value of β is chosen such that liquid bridges remain the pendular regime. [Roy \[71\]](#) argues

that for a random close packing of monodisperse spheres, the maximum available pore volume is determined by $\beta = 0.33$. However, since poor saturation is assumed in the pendular limit, a value of $\beta = 0.058$ may be chosen so that less than 6% of the pore space is occupied by liquid bridges. Figures 3-8a and 3-8b illustrate the particles' liquid content upon liquid bridge formation for CASE 2 and CASE 3 of Table 3-3, respectively. As long as $V_D \leq V_{LB_{max}}$, liquid is transferred to the bridge until the particles' liquid volume is less than or equal to $V_{L_{min}}$. In the event that $V_D > V_{LB_{max}}$, the excess liquid $V_E = V_D - V_{LB_{max}}$ remains on the particles as liquid film volume V_E^i and V_E^j , in proportion to the existing volume per particle.

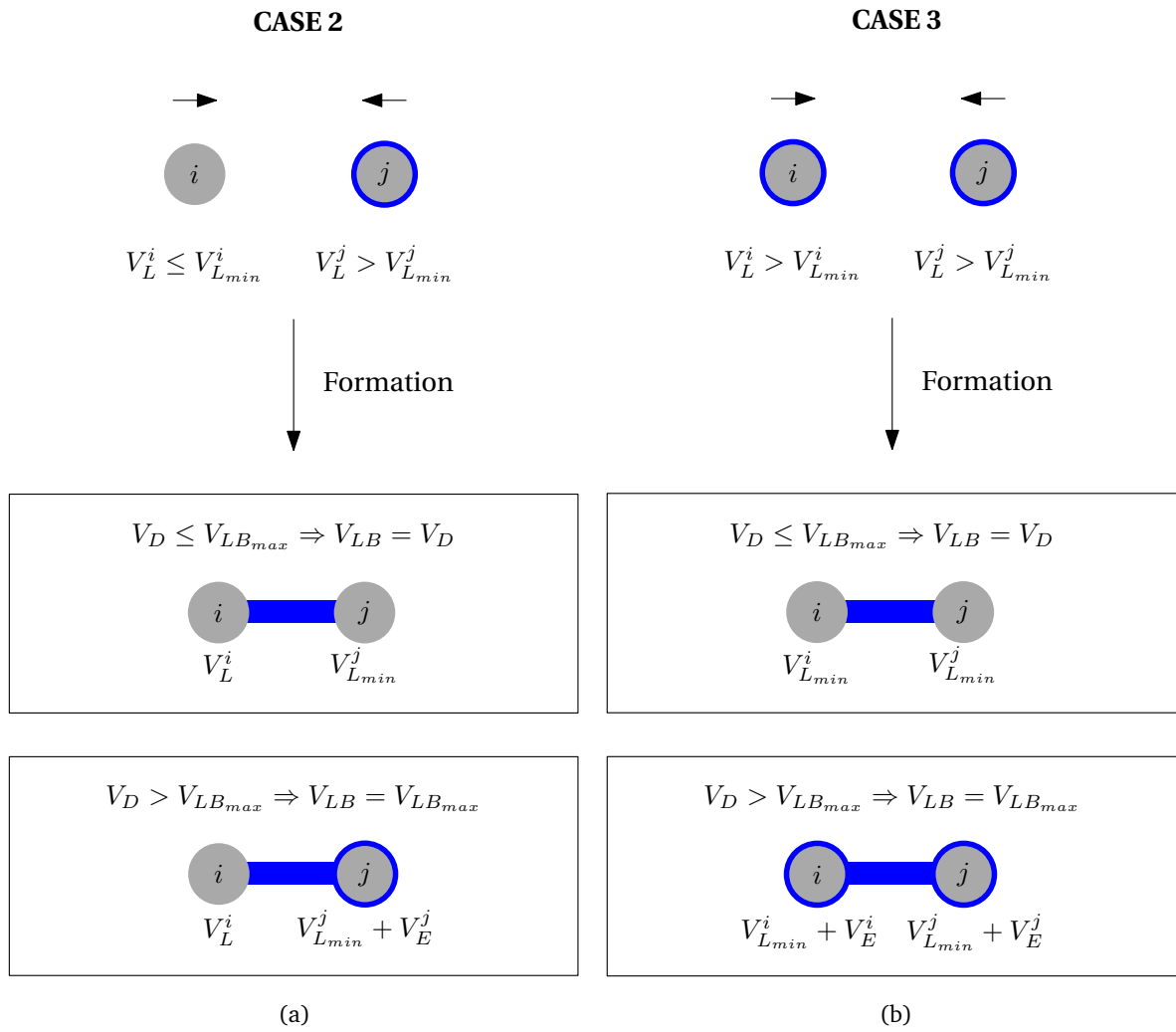


FIGURE 3-8. Illustration of (a) particles' and bridge moisture volume upon liquid bridge formation for CASE 2 of Table 3-3; (b) particles' and bridge moisture volume upon liquid bridge formation for CASE 3. Two scenarios are presented for each case: in the upper boxes, the bridge volume is no more than its maximum allowable value while in the lower boxes, the bridge volume is controlled by allocating the excess distributable volume to the contacting particles.

For particle-wall interactions a similar reasoning is applicable, with the exception that liquid cannot adhere to the system walls and therefore, their liquid content is always equal to $V_L^w = 0$. Hence,

when a wet particle comes into contact with a wall, a bridge is formed with the particle being the sole contributor of liquid to the bridge.

3.3.2.2 LIQUID BRIDGE RUPTURE

Upon rupturing of a liquid bridge between two particles, the bridge volume is redistributed as illustrated in Figure 3-9a. If the particles have multiple contacts the liquid is transferred to the individual bridges, until the maximum bridge volume is reached. Any remaining liquid is then added to the particles' film volumes.

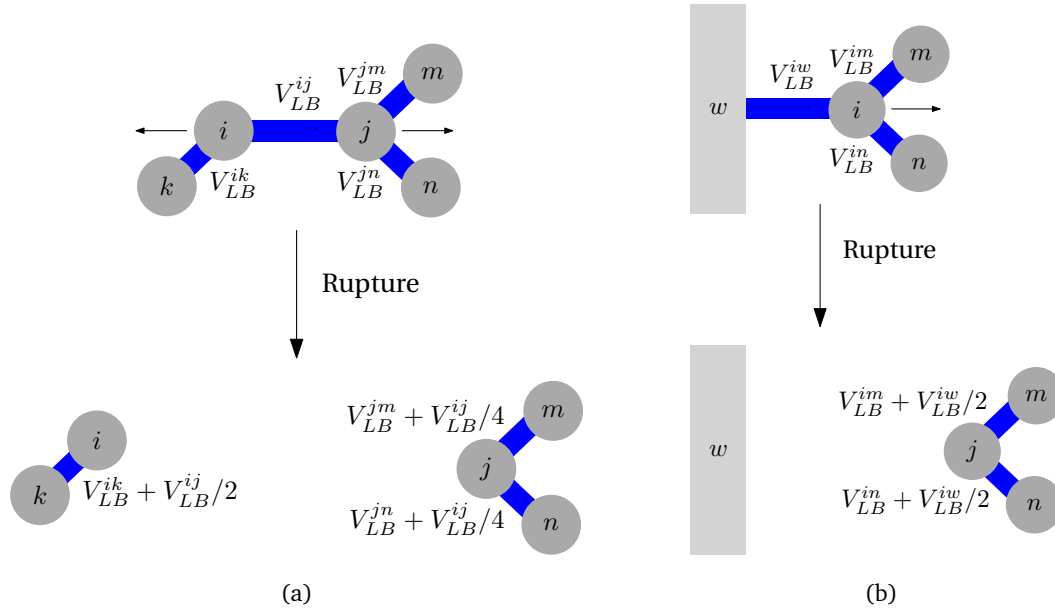


FIGURE 3-9. Illustration of liquid redistribution upon liquid bridge rupture between (a) two particles; (b) a particle and a wall.

Hence, the new volume of the liquid bridges connecting particles i and j to other particles once the liquid bridge between i and j ruptures is given by:

$$V_{LB_{new}}^{mn} = \min \left(V_{LB_{old}}^{mn} + V_{LB}^{ij} / (2N_c^m), V_{LB_{max}} \right) \quad (3.21)$$

where $m \in i, j, n$ denotes the neighboring particles in contact and N_c^m is the number of neighboring contacts associated with the particles m . When a liquid bridge between a particle and a wall ruptures, the entire liquid volume is transferred to the particle and redistributed amongst the particle's contacts (Figure 3-9b). In this case, the new volume of the liquid bridges connecting particles i to other particles once the liquid bridge between i and w ruptures is given by:

$$V_{LB_{new}}^{mn} = \min \left(V_{LB_{old}}^{mn} + V_{LB}^{iw} / N_c^m, V_{LB_{max}} \right) \quad (3.22)$$

3.4 NUMERICAL MODEL FORMULATION

Recall that the idea of DEM is to determine the trajectories of each particle in the system, i.e., to determine the particles' position and orientation at each time step. For a single pair of colliding particles, this can be done analytically by integration of Newton's laws. However, for multi-body systems, analytical solutions are not possible and numerical techniques must be used to determine the evolution of the system. The goal of a numerical scheme is to approximate the solution of a differential equation using a Taylor series. In this case, the differential equation which allows one to solve for the position of each particle i is the translational equation of motion which can be rewritten as

$$\frac{d^2 \vec{r}_i(t)}{dt^2} = \frac{\sum \vec{F}_i}{m_i} \quad (3.23)$$

This second-order equation can be reduced to two first-order differential equations with corresponding initial conditions:

$$\begin{cases} \frac{d\vec{r}_i(t)}{dt} = \vec{v}_i(t) , & \vec{r}_i(0) = \vec{r}_{0_i} \\ \frac{d\vec{v}_i(t)}{dt} = m_i^{-1} \sum \vec{F}_i = \vec{a}_i(t) , & \vec{v}_i(0) = \vec{v}_{0_i} \end{cases} \quad (3.24)$$

Similarly, the differential equations for the rotational equation of motion can be formulated:

$$\begin{cases} \frac{dq_i}{dt} = \frac{1}{2} [0 \ \omega_{ix} \ \omega_{iy} \ \omega_{iz}]^T \otimes q_i , & \vec{r}_i(0) = \vec{r}_{0_i} \\ \frac{d\vec{\omega}_i(t)}{dt} = \mathbf{I}^{-1} \sum \vec{T}_i = \vec{\alpha}_i(t) , & \vec{\omega}_i(0) = \vec{\omega}_{0_i} \end{cases} \quad (3.25)$$

Such first-order ordinary differential equations are normally well-suited to be solved using the Euler method. However, this method is not suitable for integrating Newton's laws since it lacks two important properties when considering potential (elastic) forces: energy conservation and reversibility. Other methods have been designed especially for this application, for example the Velocity Verlet algorithm, which was first introduced in 1982 as a technique known for preserving physical properties of the system. Dropping the subscript i for convenience, the derivation of the scheme is as follows. First, the position evolution function is derived by simply combining Equation (3.23) and the equation of motion:

$$\vec{r}(t + \Delta t) = \vec{r}(t) + \Delta t \cdot \vec{v}(t) + \frac{\Delta t^2}{2} \cdot \vec{a}(t) + O(\Delta t^3) \quad (3.26)$$

Next, a Taylor expansion can also be done to approximate the velocity at the next time step:

$$\vec{v}(t + \Delta t) = \vec{v}(t) + \Delta t \cdot \frac{d\vec{v}}{dt}(t) + \frac{\Delta t}{2} \cdot \frac{d^2\vec{v}}{dt^2}(t) + O(\Delta t^3) \quad (3.27)$$

The unknown terms in this expression are the velocity derivatives. The second derivative can be expressed in terms of known quantities by expanding

$$\frac{d\vec{v}}{dt}(t + \Delta t) = \frac{d\vec{v}}{dt}(t) + \Delta t \cdot \frac{d^2\vec{v}}{dt^2}(t) + O(\Delta t^2) \quad (3.28)$$

Solving this equation for the second derivative yields

$$\frac{d^2 \vec{v}}{dt^2}(t) = \frac{d\vec{v}}{dt}(t + \Delta t) - \frac{d\vec{v}}{dt}(t) + O(\Delta t^3) \quad (3.29)$$

Now, substituting this expression and the equation of motion into Equation (3.27) results in an approximation for the velocity evolution:

$$\vec{v}(t + \Delta t) = \vec{v}(t) + \frac{\vec{a}(t) + \vec{a}(t + \Delta t)}{2} \Delta t + O(\Delta t^3) \quad (3.30)$$

Neglecting higher-order terms, the Velocity Verlet approximations are summarized as:

$$\vec{r}(t + \Delta t) = \vec{r}(t) + \vec{v}(t) \Delta t + \frac{\vec{a}(t)}{2} \Delta t^2 \quad (3.31a)$$

$$\vec{v}(t + \Delta t) = \vec{v}(t) + \frac{\vec{a}(t) + \vec{a}(t + \Delta t)}{2} \Delta t \quad (3.31b)$$

It is clear that the position algorithm depends on quantities from only the current time step while the velocity algorithm requires storage of accelerations at two different time steps, t and $t + \Delta t$. This can be avoided by splitting up the velocity algorithm into two integration steps of half a time step. The implementation of the algorithm for both the translational and rotational equations of motion of a particle i is then as follows [33]:

1. Integrate the (angular) velocities by one half time step:

$$\vec{v}_i(t + \Delta t/2) = \vec{v}_i(t) + \frac{\Delta t}{2} \vec{a}_i(t) \quad (3.32a)$$

$$\vec{\omega}_i(t + \Delta t/2) = \vec{\omega}_i(t) + \frac{\Delta t}{2} \vec{\alpha}_i(t) \quad (3.32b)$$

2. Use the calculated values to integrate the positions and orientations by one full time step:

$$\vec{r}_i(t + \Delta t) = \vec{r}_i(t) + \vec{v}_i(t + \Delta t/2) \Delta t \quad (3.33a)$$

$$\mathbf{q}_i(t + \Delta t) = \mathbf{q}_i(t) + \frac{1}{2} [0 \ \omega_{ix}(t + \Delta t/2) \ \omega_{iy}(t + \Delta t/2) \ \omega_{iz}(t + \Delta t/2)]^T \otimes \mathbf{q}_i(t) \Delta t \quad (3.33b)$$

3. Compute (angular) accelerations from forces and torques at the current time step:

$$\vec{a}_i(t + \Delta t) = m_i^{-1} \sum \vec{F}_i(t + \Delta t) \quad (3.34a)$$

$$\vec{\alpha}_i(t + \Delta t) = \mathbf{I}_i^{-1} \sum \vec{T}_i(t + \Delta t) \quad (3.34b)$$

4. Integrate (angular) velocities by another half time step:

$$\vec{v}_i(t + \Delta t) = \vec{v}_i(t + \Delta t/2) + \frac{\Delta t}{2} \vec{a}_i(t + \Delta t) \quad (3.35a)$$

$$\vec{\omega}_i(t + \Delta t) = \vec{\omega}_i(t + \Delta t/2) + \frac{\Delta t}{2} \vec{\alpha}_i(t + \Delta t) \quad (3.35b)$$

As the numerical scheme is an explicit solver, it is important to determine a suitable time step which ensures stability of the integration scheme. Several approximations for the time step are available in literature, depending on the contact law [72]. Generally, the time step in DEM simulations involving dry particles is based on the particle collision event [73]. For the LSD model, the particle contact is analogous to a damped harmonic oscillator in which the contact duration t_c between two particles is determined by the half period of oscillation of the mass-spring system [33]:

$$t_c = \frac{\pi}{\omega} \quad (3.36)$$

Here, ω is the oscillation frequency of the damped oscillator, given by:

$$\omega = \sqrt{\omega_0^2 - \eta^2} \quad (3.37)$$

with $\omega_0 = \sqrt{k_n/m_{12}^{eff}}$ being the oscillation frequency of an elastic oscillator and $\eta = \gamma_n/2m_{12}^{eff}$ the effective viscosity. As the contact force only acts for the duration of a half period of oscillation, t_c defines the typical response time on contact level. A fraction of the response time is recommended as the time step for numerical integration. From experience, it is known that choosing $\Delta t \leq t_c/50$ usually provides numerical stability.

3.5 SOFTWARE IMPLEMENTATION

MercuryDPM is a simulation package consisting of object-oriented programming (OOP) codes which implement a combination of contact laws and numerical techniques to perform discrete particle simulations. This programming language uses classes and objects to build applications, where the classes are in principle “templates” containing functions and variables, which can be used to create objects with the required properties for the simulation. MercuryDPM allows users to define particles and walls with specific properties, as well as the interactions occurring between them using classes stored in the kernel. When setting up a simulation, the user creates a source file, located in a *Source* directory, in which the particulars of the simulation (initial conditions, boundary conditions, system walls, interaction parameters etc.) are implemented as objects from the kernel classes. While the simulation is running, output files are generated into a *Build* directory. Figure 3-10 gives an overview of the parameters which can be specified in the source files and which can be extracted from the output files.

3.5.1 SOURCE CODE

The numerical parameters of the source file as shown in the figure above speak for themselves and are not discussed further. The different categories of interaction parameters which are relevant for this study are briefly discussed as follows.

3.5.1.1 PARTICLES

In MercuryDPM, a specific particle type is available to associate liquid with solid particles: *LiquidFilm* particles. In summary, this is a two-layered particle consisting of a core which represents the solid

SOURCE FILE	OUTPUT FILES
<p>Numerical parameters</p> <ul style="list-style-type: none"> • Time step Δt • Time domain $[0, t_{max}]$ • Spatial domain $[x_{min}, x_{max}], [y_{min}, y_{max}], [z_{min}, z_{max}]$ 	<p>.ene file: Energy and center of mass data:</p> <ul style="list-style-type: none"> • $E_g(t), E_k(t), E_r(t), E_e(t)$ • $[X_{com}, Y_{com}, Z_{com}]$
<p>Interaction parameters</p> <ul style="list-style-type: none"> • Particle parameters • Wall parameters • Boundary parameters • Species parameters 	<p>.data file: Positions, velocities, angular velocities:</p> <ul style="list-style-type: none"> • $x(t), y(t), z(t)$ • $v_x(t), v_y(t), v_z(t)$ • $q_x(t), q_y(t), q_z(t)$ • $\omega_x(t), \omega_y(t), \omega_z(t)$
	<p>.out file: User-defined output file</p>

FIGURE 3-10. Overview of the key elements contained in a source file and the various output files.

material (grain) and a virtual liquid layer surrounding the core. The user can assign the following properties to the particles i :

- Radius a_i
- Position r_i
- Velocity v_i
- Angular velocity ω_i
- Liquid volume V_{L_i}

3.5.1.2 WALLS

The system geometry can be defined in MercuryDPM using the standard packages or by importing a geometry from binary STL, STEP or VTK files using the *readTriangleWall* function, which is a new feature in MercuryDPM. Since the system in this study contains non-standard geometries, the second method is employed. The reader imports the walls contained in the STL, STEP or VTK file and sets the material properties and a scale factor (to convert from STL units to DPM units) and adds the imported walls to the *WallHandler*. There are several types of walls available as packages, all derived from the common class *BaseWall*, which allows the user to specify the following properties for each wall w :

- Position r_w
- Velocity v_w
- Angular velocity ω_w

3.5.1.3 SPECIES

The species in MercuryDPM are subdivided into *NormalForceSpecies*, *FrictionForceSpecies* and *AdhesiveForceSpecies*. As the names suggest, these species deal with the normal interactions, tangential interactions and (long-range) adhesive interactions, respectively. In each of these categories, different models are available, which take into account increasingly detailed interaction phenomena such as elastic, plastic, dissipative and adhesive effects. The models from the respective categories can also be combined. For example, in this study, the *LinearViscoelasticFrictionLiquidMigrationWilletSpecies*

is used, which is assigned some general properties which can be set to any type of species (such as the density) and also inherits the properties from *LinearViscoelasticNormalSpecies* for the normal forces, the *LinearViscoelasticFrictionSpecies* for the tangential degrees of freedom and the *LiquidMigrationWilletSpecies* to model the liquid bridge interactions. The following parameters relevant to these interactions can then be specified by the user:

- ParticleSpecies
 - Density ρ
- LinearViscoelasticNormalSpecies
 - Normal stiffness k^n
 - Normal dissipation γ^n OR normal restitution coefficient ϵ^n
- LinearViscoelasticFrictionSpecies
 - Sliding, rolling and torsion stiffness k^s, k^{ro}, k^{to}
 - Sliding, rolling and torsion dissipation $\gamma^s, \gamma^{ro}, \gamma^{to}$
 - Sliding, rolling and torsion friction coefficient (static) $\mu^{ss}, \mu^{ro,s}, \mu^{to,s}$
 - Sliding, rolling and torsion friction coefficient (dynamic) $\mu^s, \mu^{ro}, \mu^{to}$
- LiquidMigrationWilletSpecies
 - Contact angle θ
 - Surface Tension σ
 - Amount of liquid fixed in the particle V_{Lmin}
 - Maximum liquid bridge volume V_{LBmax}

Once the species have been defined, they can be assigned to the particles and walls in the system. Mixed species can also be defined; these are used for the interactions between objects of two different species.

3.5.2 OUTPUT DATA

The output data files are important when analyzing the simulation results. Besides the *.ene* and *.data* files, extra output files which record the particle overlaps and liquid content of the particles are generated. To save computational effort and reduce the amount of data, the outputs are generated every 10000 time steps. The output files can be read into Matlab to sort data and analyze the simulation results. Also, Paraview can be used to visualize the simulation results.

4

MODEL IMPLEMENTATION

INTRODUCTION

In the literature review, it was found that the mixing behavior depends on the material properties, the operation conditions and the mixer geometry. This section mainly explores the effects of material parameters on the mixing behavior in a screw conveyor. This is in essence a sensitivity analysis, as the results provide information on which material parameters have the most pronounced effect on the flow behavior in the system. Also, a case study using a more complex screw design is performed to illustrate .

4.1 GOAL

An industrial system with granular flows usually contains thousands to millions of discrete particles which interact with each other through physical and non-physical contacts. Developing a computational model which is able to qualitatively reproduce the behavior of such a system is a challenging task. First of all, the solver must be capable of handling complex geometries, an enormous amount of particles and the interactions occurring between them. At the same time, the numerical code should efficiently utilize the hardware resources for performing such a large simulation. Simulations may become unstable if the numerical time step is too large, resulting in fictitious particle behavior due to numerical errors; on the other hand, a time step which is unnecessarily small prevents the simulation to be performed within a reasonable amount of time. Moreover, the value of the time step is determined as a direct function of the model parameters, depending on the contact law which is used to describe the particle interactions. Hence, the main challenge in setting the simulations parameters is selecting values of the parameters which result in both a reasonable time step and realistic bulk behavior of the material.

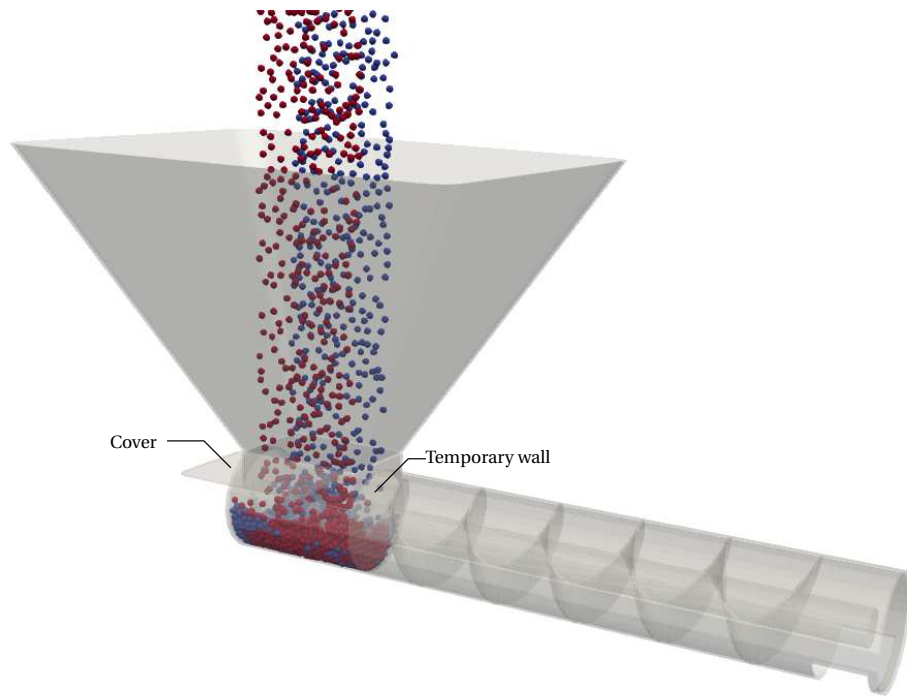
In Section 3, various contact and liquid migration parameters were presented as inputs for the simulation. The complete set of input parameters must be carefully selected in order for the model to match the actual physical system as much as possible. The methods observed in literature for determining these parameter values can generally be categorized into two groups. The *Direct Measuring*

Approach involves direct measurement of contact parameters at the particle or contact level. This method is not used extensively, since most properties are difficult to measure, especially on the microscale. Moreover, the measured values are only applicable if the true size and shape of the particles are employed in the simulation and if the contact model provides an accurate representation of the actual contact behavior. The main advantage of this approach is that the measured values are always valid, regardless of the contact model and DEM code which is used. In the second approach, the *Bulk Calibration Approach*, experiments are set up to replicate the simulation and, subsequently, the input parameters are “fitted” by trial-and-error such that the combination of these parameters in the simulation produces a bulk material behavior which is comparable to the experimental (macroscopic) result. The main drawback of this approach is that various combinations of the DEM parameters may result in the same bulk behavior. Hence, this method does not guarantee that once the model has been calibrated for a certain application, it will be accurate for another [74]. The calibration process is very time-consuming and it becomes more complex to compare or evaluate the effect of input parameters on the simulation results as the number of input parameters increases. For this reason, sensitivity analyses are often performed to evaluate the influence of the various inputs and, consequently, rank their significance based on their influence. Based on the results of the sensitivity study, a reduced set of significant parameters can be produced for the calibration step. The primary goal of the simulations in this study is to perform sensitivity analyses of the input parameters.

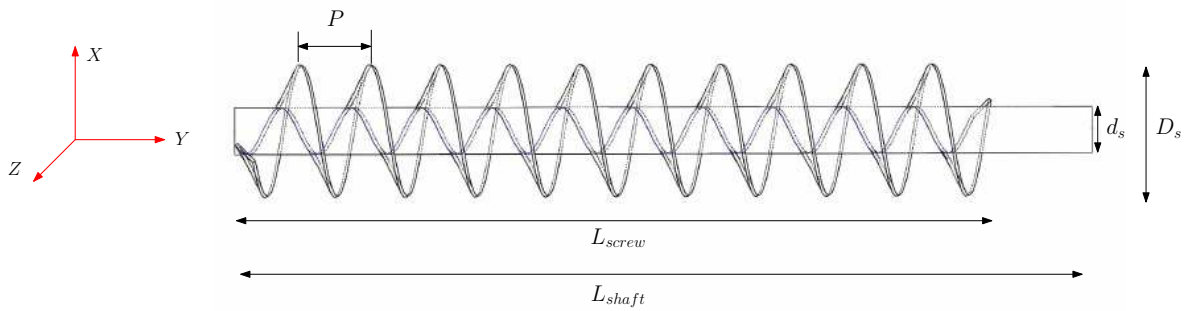
4.2 SIMULATION CONDITIONS & PROCEDURE

4.2.1 GEOMETRY

The set-up used for simulations consisted of a horizontal, single-shaft cylindrical tube screw conveyor, as shown in Figure 4-1. Due to its geometrical complexity, the model was created in SolidWorks and subsequently imported in MercuryDPM as a binary STL file (in which the geometry is represented as a collection of triangular surfaces) using the *readTriangleWall* tool. Several geometrical aspects were considered when setting up the simulation. The first challenge was defining the mixing screw as a rotating surface, while the mixer housing remained stationary. To achieve this, the *readTriangleWall* function was further developed in this study to include extra parameters for the imported walls. More specifically, the possibility to assign an angular velocity and corresponding center of rotation to a specific set of walls was created, providing the user with the freedom to assign different properties to selected parts of the geometry. Another point to consider was the clearance between the screw and the tube. This distance was minimized to avoid particles getting “stuck” between the blade and the tube wall and subsequently being pushed through the walls. Finally, some walls were added to the geometry to aid the simulation. To prevent the particles from traveling further down the tube, a temporary wall (Figure 4-1a) is placed as a barrier during the settling phase which is removed from the simulation right before the screw is set into motion. After the particles have settled down, the tube is closed off with a cover and the shaft starts to rotate. The cover is added to the simulation to prevent the particles from “flying” out of the tube and re-entering the hopper. The mixing element and coordinate system are shown in Figure 4-1b. The relevant dimensions of the screw are listed in Table 4.1.



(a)



(b)

FIGURE 4-1. (a) Geometry used in the simulations (b) illustration of the mixing screw with dimensions presented in Table 4.1.

TABLE 4.1. Dimensions of the screw in the conveyor system.

Parameter	Value
Screw length L_{screw} [m]	0.472
Shaft length L_{shaft} [m]	0.550
Pitch P [m]	0.045
Screw diameter D_s [m]	0.090
Shaft diameter d_s [m]	0.030

4.2.2 PARTICLES

At the beginning of the simulation, the particles are randomly generated and positioned at the inlet of the hopper. They are subsequently allowed to fall freely under gravity and left to settle (i.e., until they have dissipated a certain amount of their energy) into the portion of the tube enclosed by the temporary cover while the screw remains stationary. It was found that the insertion of cohesive particles in this manner leads to blockage above the mixing screw during the settling phase, due to the formation of liquid bridges and subsequent particle-particle adhesion before the material settles down. To minimize this effect, wet particles are inserted with $\sigma = 0$ during the settling phase. By setting this value of the surface tension, the liquid bridge forces are activated but return a value of zero, allowing the particles settle without agglomeration. This study employs mono-sized particles, as this is the simplest case and requires less computational effort when compared to simulations using particles of varying sizes.

4.2.3 SPECIES

As discussed in Section 3.2, only the sand and cement particles are considered as the material components in this study so that only two particle species and a wall species are required. Additionally, a separate species is needed for all inter-species interactions (cement-sand, cement-wall, sand-wall). Hence, six species must be defined to describe all the possible interactions as shown in Table 4.2.

TABLE 4.2. Overview of the species used in the simulation, where the ‘×’ indicates the objects between which an interaction occurs and for which the interaction parameters are set within the species.

	Particle type-1: cement	Particle type-2: sand	Walls	Contact type
species 0			×	wall-wall
species 1	×			cement-cement
species 2		×		sand-sand
species 01	×		×	wall-cement
species 02		×	×	wall-sand
species 12	×	×		cement-sand

As seen in Figure 4-2, a total of 24 input parameters (yellow fields) are required for the model. In Section 3 it was discussed that the time step can be determined as a function of the particle and (certain) interaction parameters, $\Delta t = f(m_{eff}, k_n, \gamma_n)$. It was also shown that the normal stiffness,

damping coefficient and restitution coefficient are linked to each other via mathematical relationships, allowing one to be determined if the other two are known. This inter-dependency of parameters provides a first reduction of the number of unknown inputs. In the following, it will be discussed how other parameters such as the spring stiffnesses and damping coefficients of the tangential degrees of freedom can be deduced from the normal stiffness and damping coefficient to serve as preliminary estimates. This results in a final set of 16 parameters (shown in the yellow fields enclosed by red lines in Figure 4-4) to be specified for each of the model species. A brief survey of these parameters is presented below to provide some perspective on the rationale for their selection.

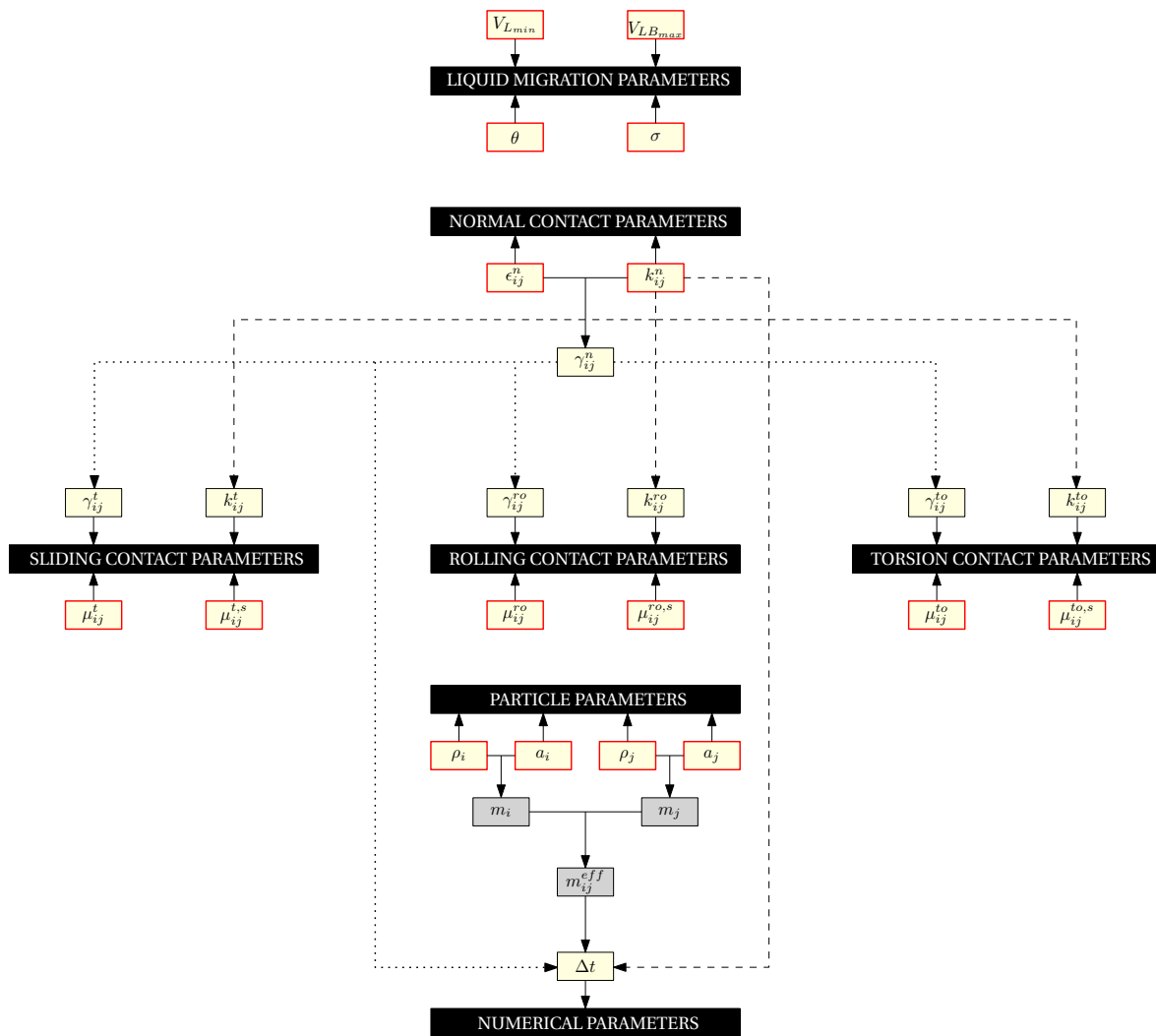


FIGURE 4-2. Overview of the particle, interaction and numerical input parameters with the arrows indicating which parameters can be calculated as functions of each other. The yellow fields indicate which parameters must be determined by model calibration while the grey fields can simply be derived from the yellow fields.

4.2.3.1 MATERIAL PARAMETERS

The relevant material-dependent properties are the particle size, density, water intake and contact angle for cement (CEM I 52.5 R) and sand (which is assumed to be 0-2 mm sand), and surface tension for water. Table 4.3 presents indicative values for these properties based on ranges and/or experimental measurement results found in literature. The water intake values were not found in literature, hence, the effect of this parameter will be studied in the simulations.

TABLE 4.3. Summary of the true material properties found in literature.

	Symbol	Sand	Cement	Water
Median diameter [mm]	d_{50}	9×10^{-1} [75]	4.5×10^{-3} [75, 76]	
Bulk density [kg/m ³]	ρ_b	1500 [9]	1100 [77]	
Particle density [kg/m ³]	ρ_p	2412 [9]	3120 [77]	
Contact angle [deg]	θ	0 [75]	25 [75]	
Surface tension [N/m]	σ			0.07275 [9]

Particle size

The material properties shown in Table 4.3 are retrieved from literature for the actual materials, i.e., considering actual size and shapes of the particles. Ideally, the number of particles in the system would be reasonable enough to use the actual particle size in the simulation. In reality, industrial systems contain a very large amount of individual particles of microscopic size making it infeasible to model the computational volume using the actual particle size. Also, it is impossible to accurately resemble the actual shape of each individual particle in the simulation. Hence in practice, spherical particles are assumed and the number of particles N_p is often reduced with respect to the size of the simulation domain. This can be done by scaling the particle size, i.e., using so-called pseudo-particles, which represent a collection of unscaled particles. By altering the size and shape of the particles in the simulation, the material properties must also be adjusted to maintain the actual bulk properties.

Particle density

With regard to the density, a distinction is made between the particle density ρ_p and the bulk density ρ_b . The bulk density is generally defined as the mass of a bulk material sample divided by the bulk volume occupied by that sample, i.e., the bulk density accounts for volume of the particles *and* the voids between the particles in the packing. As the voids are generally filled by air, it can be assumed that the mass of the voids is negligible and therefore, the bulk mass is approximately equal to the particles' total mass. Hence, the bulk density is determined by:

$$\rho_b \approx \frac{m_p}{V_b} \quad (4.1)$$

The particle density, on the other hand, only accounts for the mass and volume occupied by the solids in the packing:

$$\rho_p = \frac{m_p}{V_p} \quad (4.2)$$

When using upscaled particles, the adjusted particle densities for sand and cement are determined using the following methodology:

- The geometry is filled with particles by allowing them to fall under gravity and settle down. The particle bed is leveled by removing all particles above a certain specified height H in the container. The total occupied (bulk) volume V_b is then determined at the height H .
- The total mass of all particles is calculated:

$$m_p = \rho_p \times V_p = \rho_p \times \left(N_p \frac{4}{3} \pi a_p^3 \right) \quad (4.3)$$

- The bulk density is calculated:

$$\rho_b = \frac{m_p}{V_b} \quad (4.4)$$

- The bulk density is determined for a range of particle density values, $\rho_p \in [1000, 2000, 5000, 10000]$ and a value of ρ_p that corresponds to the bulk density of the material reported in Table 4.3 is subsequently determined by interpolation of the data set.

4.2.3.2 INTERACTION PARAMETERS

Spring stiffness

The value of the normal spring stiffness is an important parameter as it directly affects the degree of particle overlap and the simulation time step. Typical values of k^n are usually between $10^6 - 10^8$ N/m, however, many studies report the use of much smaller values in the order of 10^3 N/m [78]. It must be noted that the use of such small values is usually justified in systems where the contact forces are not the predominant forces in the system, for example in fluidized beds. In mixers however, particle contacts are critical to the motion and the effect of the spring stiffness on the particle impact characteristics must be carefully considered [79]. Such an analysis can be done by considering the mechanical energy evolution of the particles, with the total mechanical energy of a particle i being defined as the sum of the gravitational potential energy, the kinetic energy and the elastic potential energy:

$$E_m = E_g + E_k + E_e = m_i g h + \frac{1}{2} m_i v_i^2 + \frac{1}{2} k_n \delta_{ij}^2 \quad (4.5)$$

In theory, when friction effects are neglected in the analysis, the total mechanical energy is conserved. This assumption already provides an indicative value for the stiffness. To demonstrate, we consider the simple case of a spherical particle which falls freely from a certain height over a fixed particle. Initially, the particle possesses gravitational potential energy due to the height, i.e., $E_{m_1} = E_{g_1}$. At the instance just before collision, all the gravitational potential energy has been transformed into kinetic energy so that the particle is at its maximum velocity and $E_{m_2} = E_{k_2}$. As the particles overlap, the kinetic energy is transformed into elastic potential energy. Finally, at the moment of maximum overlap, the particle is motionless and the elastic potential energy reaches its maximum, so $E_{m_3} = E_{e_3}$. This example illustrates that for a certain initial distance there is a maximum velocity v_{max} and maximum overlap δ_{max} for which the conservation of energy principle is obeyed. By assuming conservation of mechanical energy for particle i between state 2 and state 3, the following expression for the required normal contact stiffness is obtained:

$$k^n = \frac{m_i v_{i_{max}}^2}{\delta_{ij_{max}}^2} \quad (4.6)$$

Hence, in order to select the spring stiffness, first, an estimation of the maximum velocity in the simulation and a value for the maximum overlap (particle-particle or particle-wall) are required. With regard to the overlap it can be said that the value of $\delta_{ij_{max}}$ generally depends on the application; however, a general rule of thumb is [78]:

$$\delta_{ij_{max}} = \pm 0.01 a_{eff} \quad (4.7)$$

The particles in the system obtain their velocities from the rotating mixing blade, the tip speed of the blade can serve as an indication of the maximum velocity:

$$v_{i_{max}} = \frac{\pi \Omega}{60} D_s \quad (4.8)$$

where D_s is the diameter of screw blade and Ω is the rotation speed in rpm. The tangential stiffness is usually determined based on analytical approaches since the tangential impact properties are often difficult to measure [80]. For example, Schäfer et al. [81] proposed a value of $k^t/k^n = 2/7$, which sets the period of normal and shear contact oscillations equal to each other. For simplicity, this value of the tangential stiffness is assumed as the nominal value in the simulations. While no indicative values were found for the rolling and torsion stiffness in literature, the same value is adopted for the simulations.

Friction and dissipation coefficients

The remaining parameters are those associated with energy loss, i.e, the restitution and friction coefficients. The normal restitution coefficient will be set, from which the normal dissipation coefficient (γ^n) can be found. Following the analogy of spring stiffness, the values for the remaining dissipation coefficients are set to $\gamma^\nu/\gamma^n = 2/7$, with $\nu = t, ro, to$. With regard to friction coefficients, static friction coefficients are typically larger than the dynamic coefficients; however, for simplicity they are often assumed to have the same value. Following this assumption, only one friction coefficient will be set for sliding, rolling and torsion (hereafter referred to as μ^t , μ^{ro} and μ^{to} , respectively).

4.3 REFERENCE SIMULATION

Initially, the effects of liquid induced cohesion are neglected by performing simulations with dry particles. The value for the spring stiffness and the particle density will be determined for the upscaled particles. As a starting point for the simulations, a particle size of $a_p = 2.83$ mm is chosen for both sand and cement particles, which results in $N_p = 2000$ while maintaining fill fraction of approximately 0.5, which results in acceptable simulation times. The remaining parameters are set to an intermediate value of 0.5 as seen in the following table.

TABLE 4.4. Modeling conditions for the particle density evaluation.

a [mm]	ϵ^n [-]	μ^s [-]	μ^{ro} [-]	μ^{to} [-]	ρ_p [kg/m ³]	k^n [N/m]
2.83	0.5	0.5	0.5	0.5	?	?

4.3.1 STIFFNESS ANALYSIS

As shown in Table 4.5, the particle size, restitution and friction coefficients are kept constant while the normal stiffness is varied. As the particle density is not yet determined, the values reported in Table 4.3 are used as an initial value. The time step is chosen as $\Delta t = 0.02 \times t_c$. Following the estimation procedure described in Section 4.2.3.2, a maximum spring stiffness of $k^n \approx 12 \times 10^4$ N/m is required for a rotational speed of $\Omega = 120$ RPM, which is the maximum rotational speed which will be considered in this study. In the following, three sets of simulations will be performed for different values of the spring stiffness: the reference value, a value one order of magnitude higher and lastly, a value one order of magnitude lower. Each case study is performed using a filling fraction of 0.5 and different values of the shaft rotation speed $\Omega \in [60, 120]$ rpm. Figures 4-3a-b demonstrate the degree of overlaps and average particle velocity occurring during the mixing with $\Omega \in [60, 120]$ rpm, respectively. As expected, the number of high particle deformations increases as the value of k^n is reduced and, at a constant value of the stiffness, larger deformations occur as the rotation speed Ω increases.

TABLE 4.5. Modeling conditions for the normal stiffness evaluation.

	a [mm]	ϵ^n [-]	μ^s [-]	μ^{ro} [-]	μ^{to} [-]	k^n [N/m]
Case 1						12×10^5
Case 2	2.83	0.5	0.5	0.5	0.5	12×10^4
Case 3						12×10^3

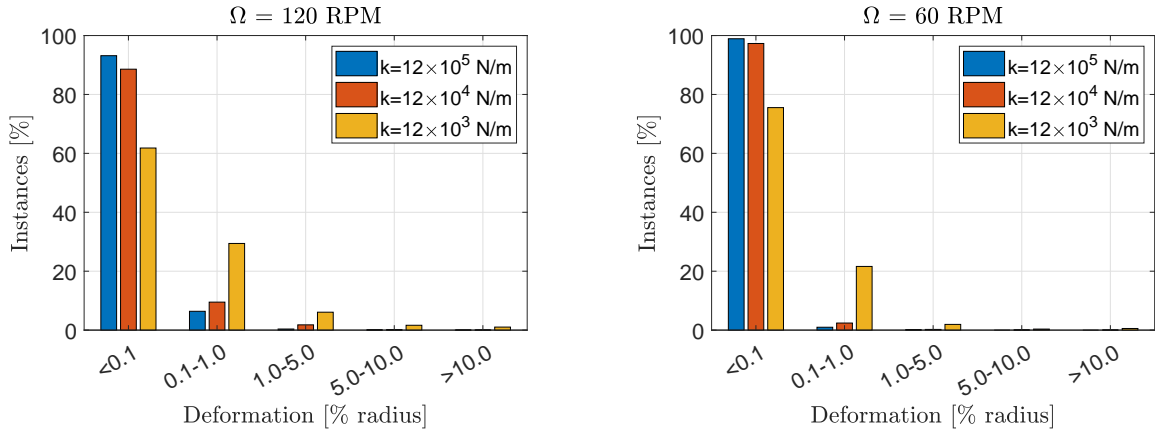


FIGURE 4-3. (a) Particle deformation and (b) average particle velocity for different values of the spring stiffness at $\Omega = 120$ RPM and $\Omega = 60$ RPM.

4.3.2 PARTICLE DENSITY

Using the determined value of the stiffness, the correct particle densities are now determined. The simulation parameters are summarized in the following table.

TABLE 4.6. Modeling conditions for the particle density evaluation.

a [mm]	ρ_p [kg/m ³]	ϵ^n [-]	μ^s [-]	μ^{ro} [-]	μ^{to} [-]	k^n [N/m]
2.83	$[1, 2, 5, 10] \times 10^3$	0.5	0.5	0.5	0.5	12×10^5

Following the method described in Section 4.2.3.1, the bulk densities are calculated from their respective particle densities for as shown in Figure 4-4. A linear fit is applied to the data points to allow for the interpolation of the particle density which corresponds to the bulk density values of sand and cement presented in Table 4-4. Through this fit it was found that $\rho_{p,sand} = 2351.8 \text{ kg/m}^3$ and $\rho_{p,cement} = 1724.7 \text{ kg/m}^3$ in simulations where the particle size is $a = 2.83 \text{ mm}$.

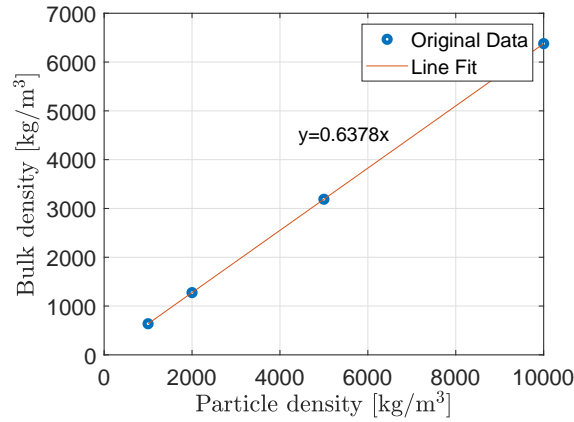


FIGURE 4-4. Calculation of the bulk density from a range of particle densities.

Since the particle densities determined above are less than the reported values from Table 4.3, lower values of the normal stiffness are permitted. Repeating the same procedure of Section 4.3.1, we obtain a maximum stiffness of $k^n = 8.9 \times 10^4 \text{ N/m}$.

4.4 PARTICLE RESOLUTION ANALYSIS

As the particle size of $a = 2.83 \text{ mm}$ was chosen arbitrarily, a scaling analysis is performed to analyze how the material behavior changes by increasing or decreasing the particle resolution. When using upscaled particles, the main idea is that the number of elements in the analysis must be chosen such that the system behavior is captured accurately, and, on the other hand, the number of elements must be minimized such that the simulation can be run in a reasonable amount of time. It is generally expected that increasing the particle resolution produces more accurate results. Although no experimental data is available for comparison, the particle kinetics from the simulations can be compared to each other in order to obtain an indication of when the particle behavior appears to vary significantly as the scale increases. Two additional simulations are performed in order of increasing particle resolution for comparison with the reference simulation, as seen in the following table. For each case, the particle density and the stiffness are determined following the same procedure of Section 4.3. All dissipation coefficients are kept at a value of 0.5.

TABLE 4.7. Parameters for the particles resolution simulations with the grey colored row indicating the reference simulation.

	N_p	a [mm]	$\rho_{p,sand} / \rho_{p,cement}$ [kg/m ³]	k_n [N/m]	Δt [s]
Case 0	2000	2.83	2351.8/1724.7	8.9×10^4	1.02×10^{-5}
Case 1	5000	2.09	2335.7/1712.9	8.8×10^4	1.03×10^{-6}
Case 2	10000	1.66	2330.6/1709.1	8.8×10^4	1.03×10^{-6}

The velocity profiles for each simulation case are shown in Figure 4-5. The graphs clearly show a large deviation in the average velocity for the coarse particle grid ($N_p = 2000$) in comparison to the other two profiles which are strikingly similar. Based on these results, at this stage it is assumed that using $N_p = 5000$ in the simulations is sufficient. In the future a more extensive resolution analysis is required where simulation results are compared to experimental results.

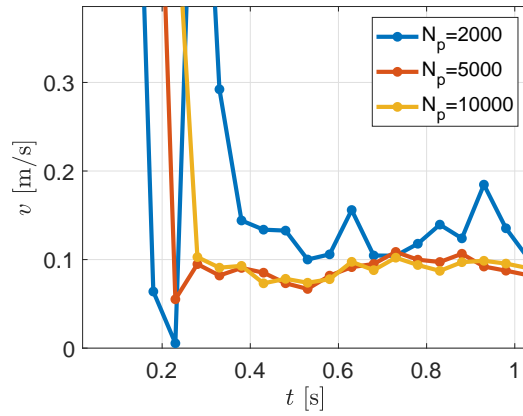


FIGURE 4-5. Particle velocity profiles for simulations with 2000, 5000 and 10000 particles.

4.5 EFFECTS OF INTERACTION PARAMETERS

4.5.1 EFFECT OF FRICTION

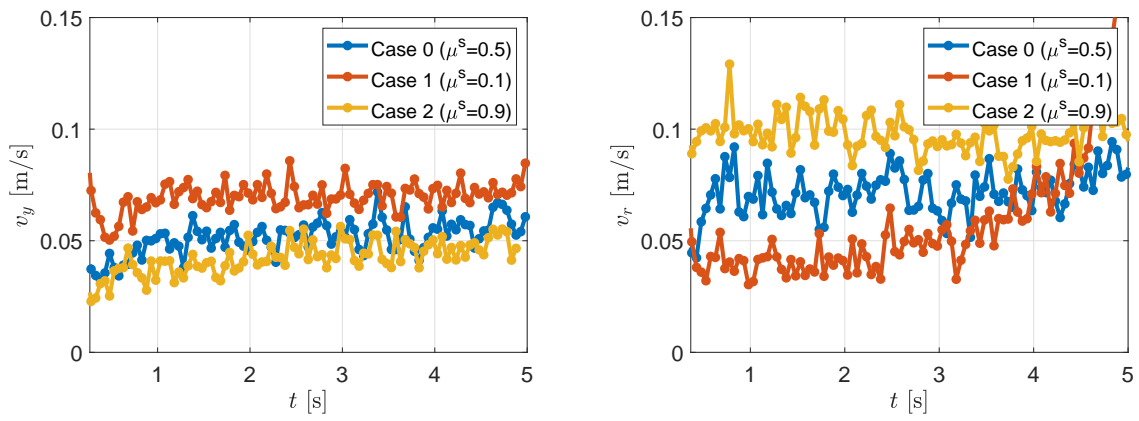
The effects of all three friction coefficients μ^s , μ^{ro} and μ^{to} is analyzed by performing the case studies listed in Table 4.8. In the reference simulation (Case 0), all three coefficients are set to an intermediate value of 0.5 for all species. Next, six other simulations (Case 1-6) are performed in which each coefficient is set to a low value (0.1) and high value (0.9) while the other coefficients are kept at the base case value of 0.5 for all species. Based on the results from these studies, a final set of simulations (Case 7-10) is performed to differentiate between particle-wall friction (μ_{01}, μ_{02}) and particle-particle friction ($\mu_{1-1}, \mu_{2-2}, \mu_{1-2}$). In each simulation the rotation speed is $\Omega = 60$ RPM and the number of particles is kept constant such that the filling fraction is approximately equal to 0.5.

TABLE 4.8. Model parameters for the friction sensitivity analysis with 50% filling volume and rotation speed of $\Omega = 60$ RPM.

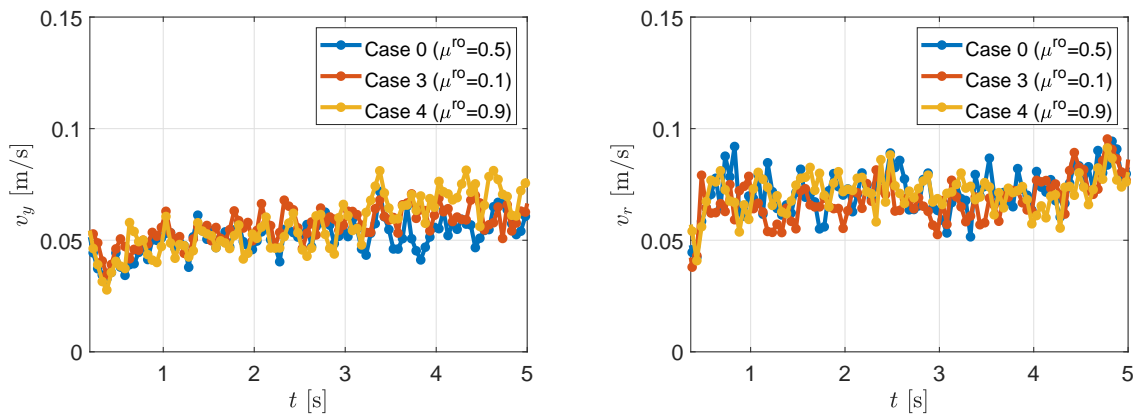
	Species	ϵ^n	μ^s [-]	μ^{ro} [-]	μ^{to} [-]
Case 0	<i>all</i>	0.5	0.5	0.5	0.5
Case 1	<i>all</i>	0.5	0.1	0.5	0.5
Case 2	<i>all</i>	0.5	0.9	0.5	0.5
Case 3	<i>all</i>	0.5	0.5	0.1	0.5
Case 4	<i>all</i>	0.5	0.5	0.9	0.5
Case 5	<i>all</i>	0.5	0.5	0.5	0.1
Case 6	<i>all</i>	0.5	0.5	0.5	0.9
Case 7	<i>0-1, 0-2</i>	0.5	0.1	0.5	0.5
	<i>1-1, 2-2, 1-2</i>		0.5		
Case 8	<i>0-1, 0-2</i>	0.5	0.9	0.5	0.5
	<i>1-1, 2-2, 1-2</i>		0.5		
Case 9	<i>0-1, 0-2</i>	0.5	0.5	0.5	0.5
	<i>1-1, 2-2, 1-2</i>		0.1		
Case 10	<i>0-1, 0-2</i>	0.5	0.5	0.5	0.5
	<i>1-1, 2-2, 1-2</i>		0.9		

4.5.1.1 PARTICLE VELOCITIES AND FLOW PATTERNS

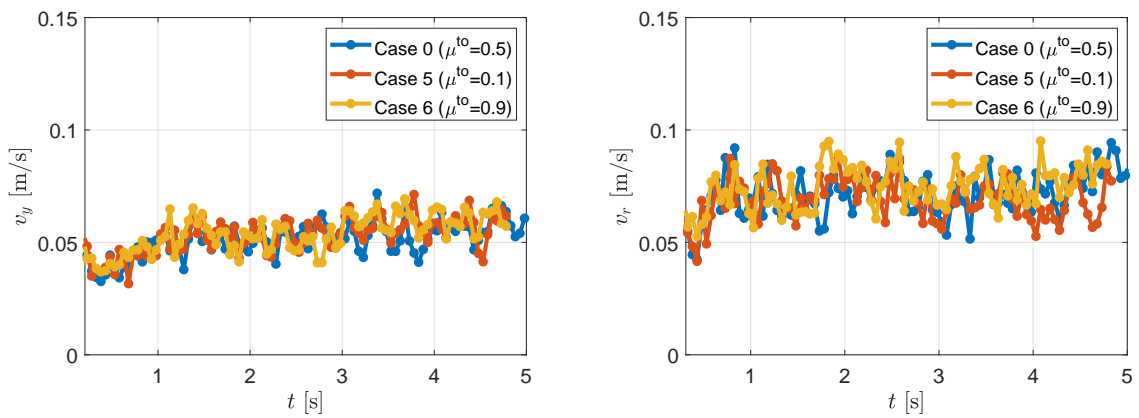
The particle velocities are examined to achieve a better understanding of the particle flow. Figure 4-6 shows the average axial velocity in the feeding direction v_y (left) and the average circumferential (swirl) velocity $v_r = \langle \vec{v}_x, \vec{v}_z \rangle$ (right) for Case 0-6. Several conclusions can be drawn from the graphs. First of all, it is clear that the axial and swirl velocity curves for rolling (Figure 4-6b) and torsion friction (Figure 4-6c) coincide with one another and show similar trends, which indicates that the variation of μ^{ro} and μ^{to} has no significant effect on the velocity and direction of particle movement inside the screw conveyor. However, this does not apply for the sliding friction coefficient (Figure 4-6a). It can be seen that the average axial velocity becomes lower as μ^s increases, which is an expected result since sliding friction hinders the particles' axial motion. Conversely, the average swirl velocity increases for higher μ^s values as the particles are more easily transported in tangential direction due to the rotating motion of the shaft.



(a) Sliding friction



(b) Rolling friction



(c) Torsion friction

FIGURE 4-6. Effect of (a) sliding friction, (b) rolling friction and (c) torsion friction on the average axial velocity and the average swirling velocity for $\Omega = 60$ RPM.

Figure 4-7 shows snapshots of the particle flow for the sliding friction cases. The top figure clearly shows the (mostly) axial flow direction of the particles when sliding friction is low. As the friction increases, the radial motion becomes more dominant and mixing action is enhanced.

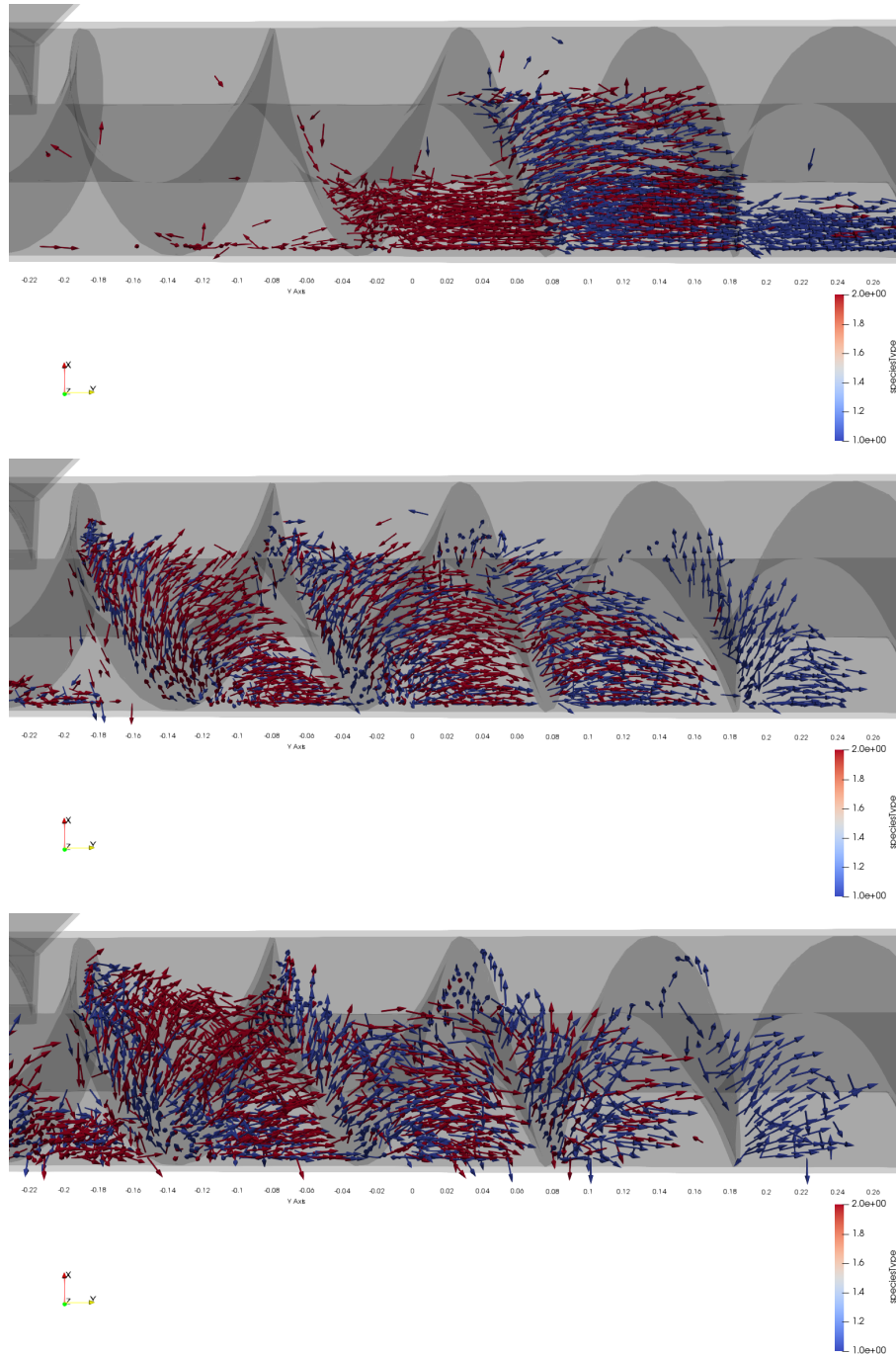


FIGURE 4-7. Effect of sliding friction on the flow direction where (a) $\mu^s = 0.1$, (b) $\mu^s = 0.5$ and (c) $\mu^s = 0.9$.

Figure 4-8 and 4-9 show the average axial and radial position of the particles for the different friction coefficients, respectively, with the vertical bars representing the standard deviation. First, we analyze the graphs displaying the average axial position. The steepness of the graph provides an indication of how fast the material travels through the conveyor. As expected from the discussion of particle velocities, it is clear that the flow of particles through the screw conveyor is only slightly affected by μ^{ro} (Figure 4-8b) and practically unaffected by μ^{to} (Figure 4-8c), while the material travels faster from the inlet to the outlet for decreasing values of μ^s .

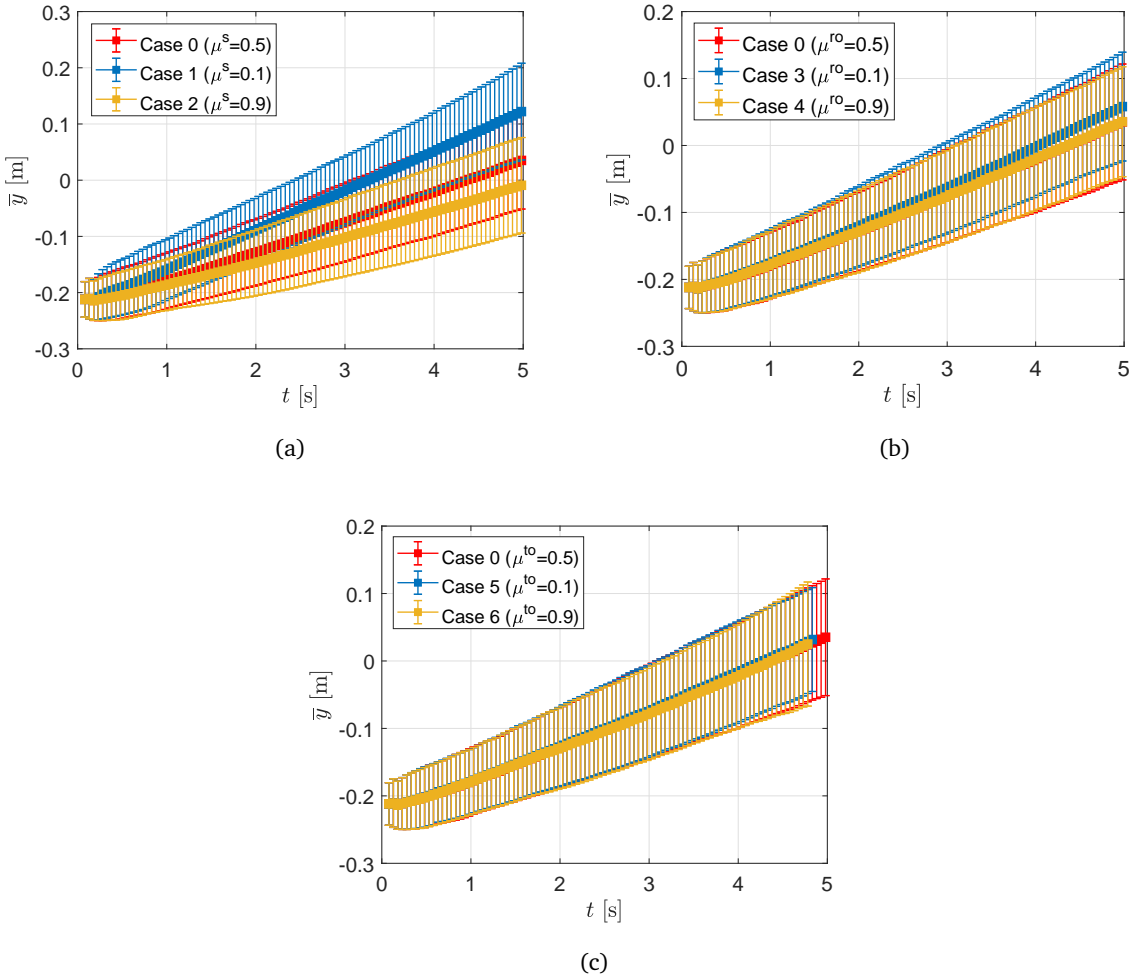
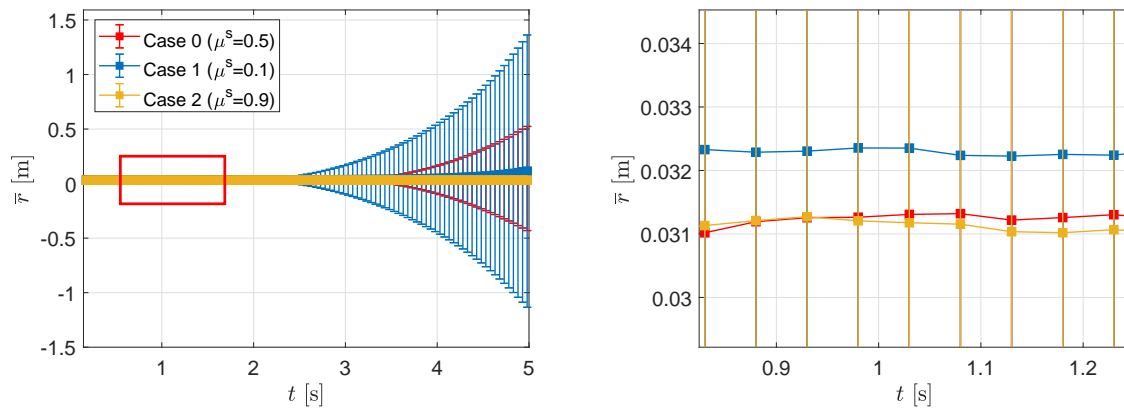
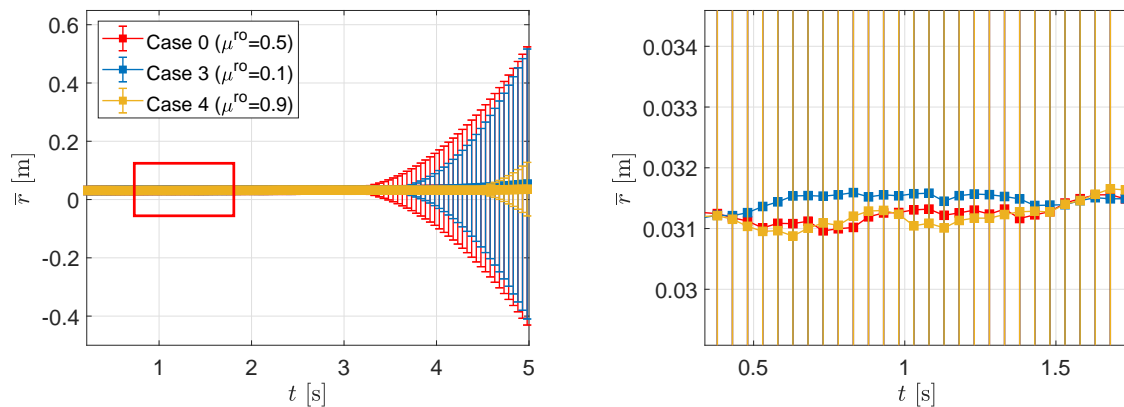


FIGURE 4-8. Effect of (a) sliding friction, (b) rolling friction and (c) torsion friction on the average axial position of the particles for $\Omega = 60$ RPM, with vertical lines representing the standard deviation.

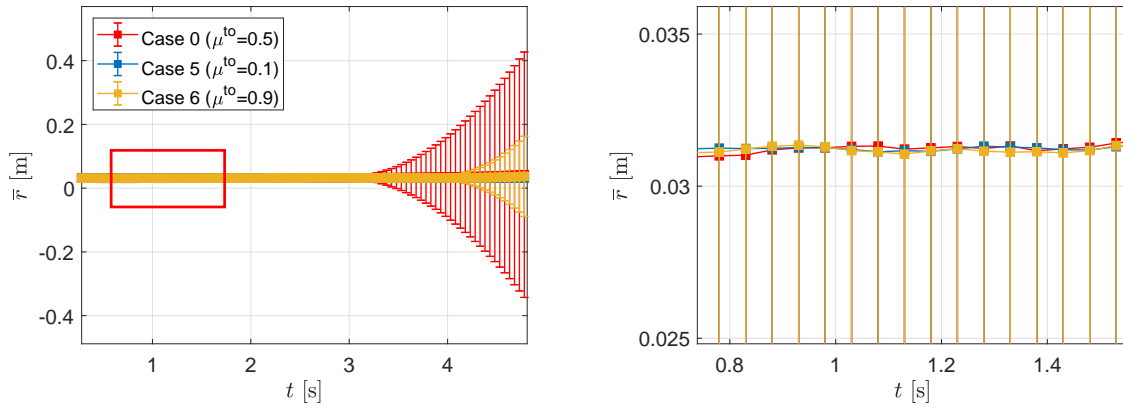
Figure 4-9 shows the graphs for sliding, rolling and torsion friction with regard to the radial position. The figures on the left present the overall graphs from which it can be observed that the curves slowly tilt upwards towards the end. For example for Case 1 in Figure 4-9a (left) the curve becomes more steep after approximately $t = 4$ s. Since the average radial position is determined by the x coordinate, this indicates that particles are being discharged at the exit of the conveyor, as x becomes increasingly large for particles falling out of the system. The figures on the right are zoomed-in from a part of the overall graph –where no particles have been discharged yet– enclosed by the red lines. From inspection of all three graphs it is once again evident that the effect of torsion friction is negligible. The effect of sliding friction is clearly visible, and, it appears that the difference between the profiles becomes less pronounced for higher values of μ^s . A somewhat similar trend is visible for rolling friction; however, the effect is less significant.



(a) Sliding friction



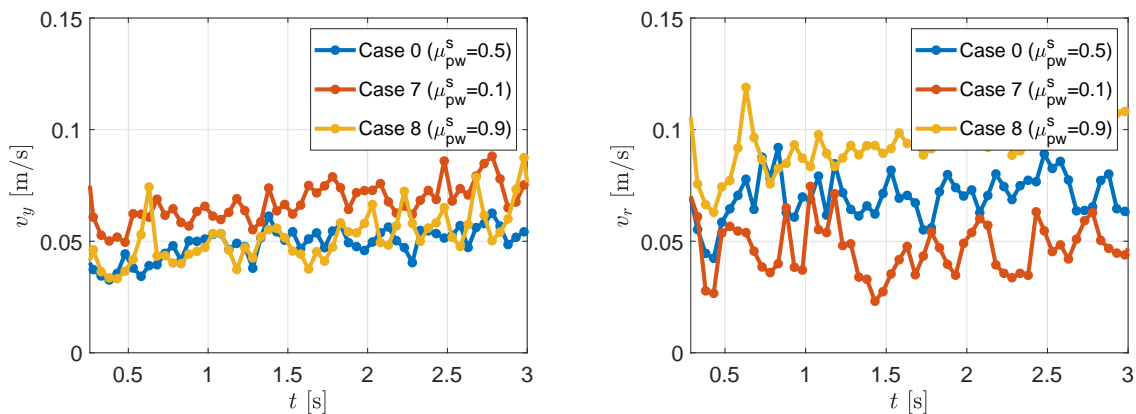
(b) Rolling friction



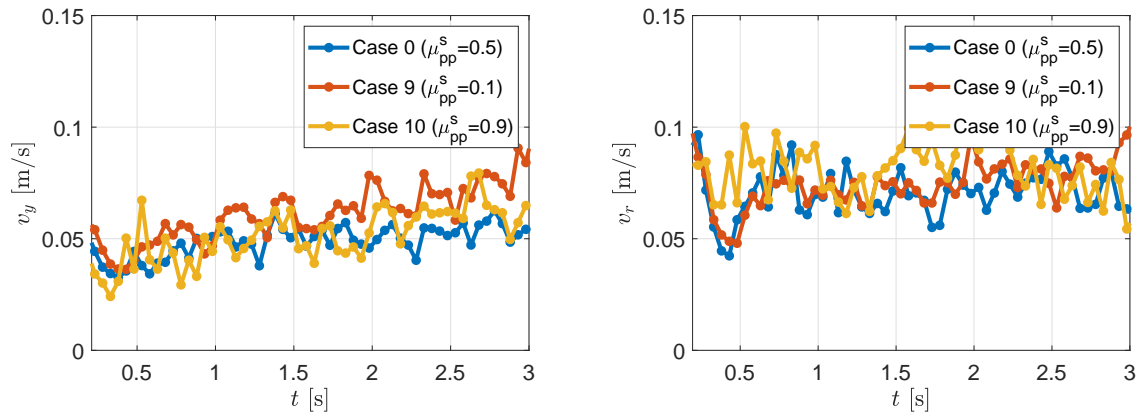
(c) Torsion friction

FIGURE 4-9. Effect of (a) sliding friction, (b) rolling friction and (c) torsion friction on the average radial position of the particles for $\Omega = 60$ RPM, with vertical lines representing the standard deviation.

From the first set of simulations it was found that the sliding friction coefficient has a significant effect on the material behavior in the screw conveyor. Previously, the same value of the friction coefficient was assumed for all species. A more detailed analysis is performed by distinguishing between the sliding friction between particles μ_{pp}^s and between particles and walls μ_{pw}^s . Figure 4-10a shows the velocity profiles for varying particle-wall sliding friction coefficients while keeping the particle-particle friction at 0.5 (Case 1, 7 and 8) and Figure 4-10b shows the profile for varying particle-particle sliding friction coefficients while keeping the particle-wall friction at 0.5 (Case 1, 9 and 10). Although both μ_{pp}^s and μ_{pw}^s seem to affect the average particle velocity, the effect of μ_{pw}^s is more pronounced.



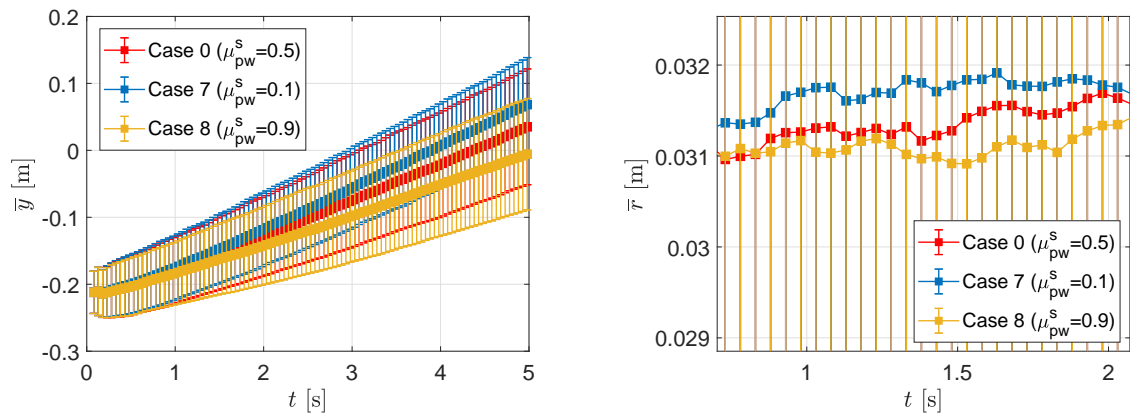
(a) Particle-wall sliding friction



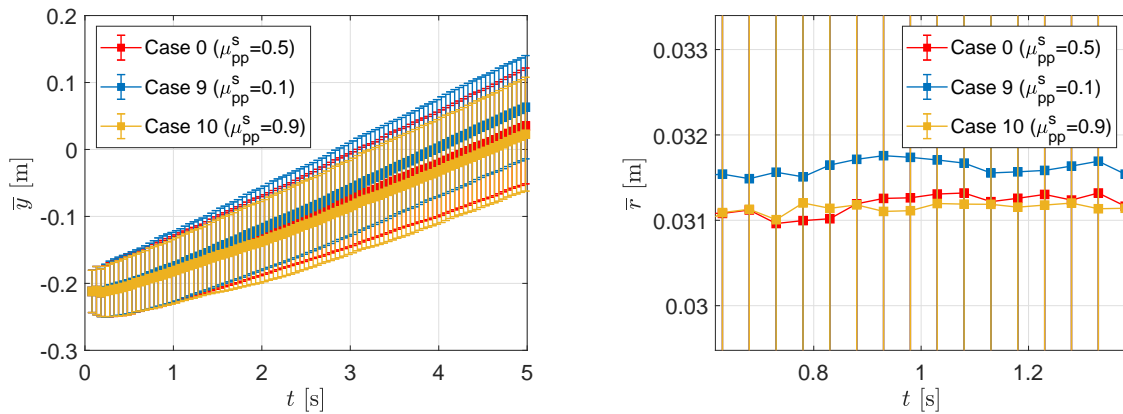
(b) Particle-particle sliding friction

FIGURE 4-10. Effect of (a) particle-wall sliding friction and (b) particle-particle sliding friction on the average axial velocity and the average swirling velocity for $\Omega = 60$ RPM.

Similar to the previously performed analysis of average particle positions, the average axial and (zoomed-in) radial position profiles are shown in Figure 4-11. It can generally be concluded that the variations are larger for particle-wall friction, both for the average axial and average radial position. Also, the profiles for particle-particle friction show the same trend as in Figure 4-9a, i.e., the variations in radial position become less evident for higher values of μ_{pp}^s .



(a) Particle-wall sliding friction

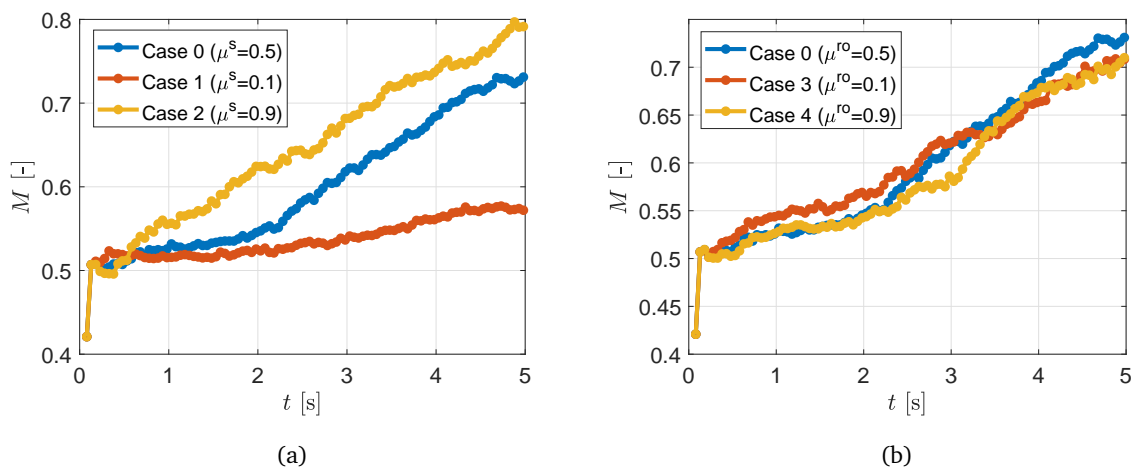


(b) Particle-particle sliding friction

FIGURE 4-11. Effect of (a) particle-wall sliding friction and (b) particle-particle sliding friction on the average axial and (zoomed-in) radial position for $\Omega = 60$ RPM.

4.5.1.2 MIXING DEGREE

From the previous analyses it can already be concluded that a low value of μ^s results in poor mixing, as the particles mostly travel axially as a “block” with limited relative movement. This is confirmed by analysis of the mixing index, as shown in Figure 4-12a. Figure 4-12b and c show that mixing is much less sensitive to the rolling friction coefficient and practically not affected by the torsion friction coefficient. Finally, Figure 4-12d and e show the effect of particle-wall and particle-particle sliding friction coefficients on the mixing index. From the previous analyses it was already found that both coefficients affect the flow; however, the particle-wall coefficient is more significant. This result is also reflected in the mixing indices.



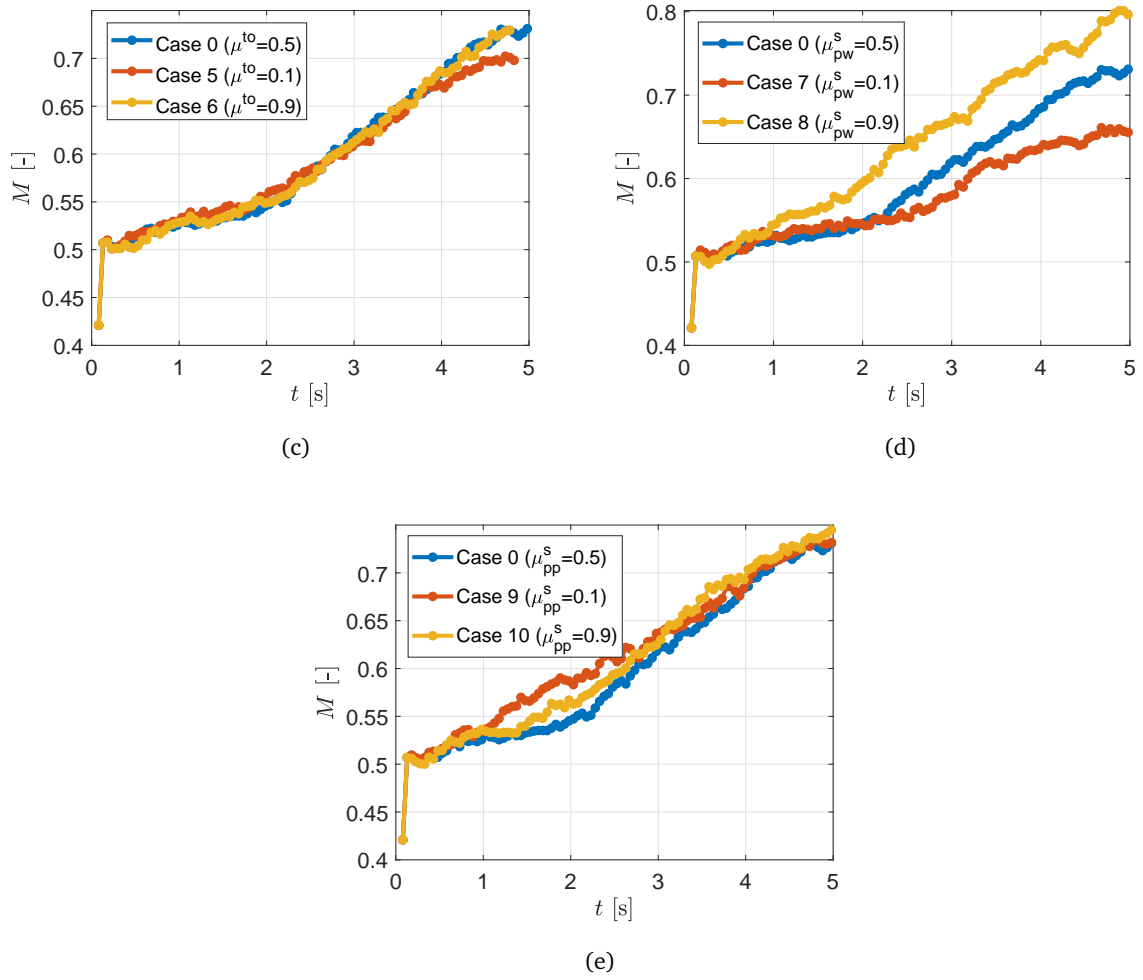


FIGURE 4-12. Effect of (a) sliding friction, (b) rolling friction, (c) torsion friction, (d) particle-wall sliding friction and (e) particle-particle sliding friction on the mixing index.

4.5.2 EFFECT OF THE RESTITUTION COEFFICIENT

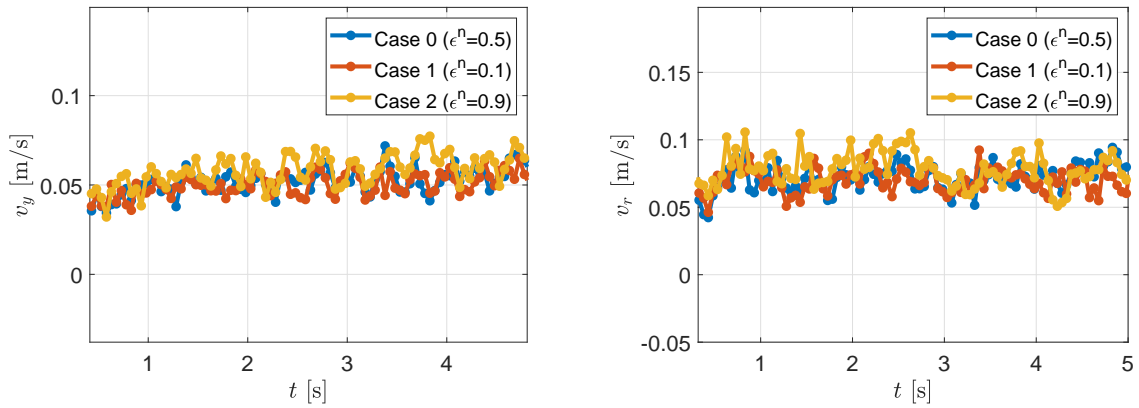
Next, the effect of the normal restitution coefficient ϵ^n is considered. Again, an intermediate value of 0.5 is used for the base case simulation (Case 0) for all species and subsequent simulations are performed using a low value (Case 1) and high value (Case 2) as shown in Table 4.9. In each simulation the number of particles is kept constant such that the filling fraction is equal to 0.5. Next, additional simulations are performed in which the effect of particle-particle (Case 3 and 4) and particle-wall (Case 5 and 6) restitution coefficients are considered.

TABLE 4.9. Modeling conditions for the restitution sensitivity analysis with 50% filling volume and rotation speed of $\Omega = 60$ RPM.

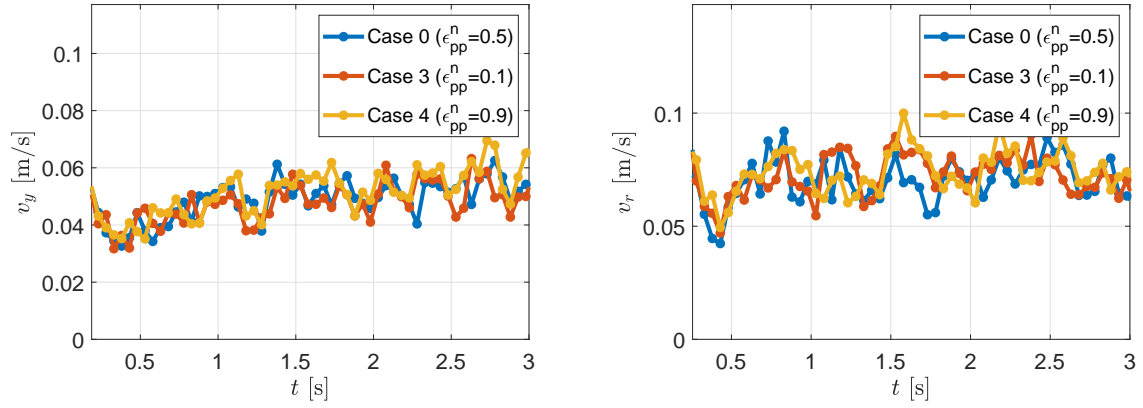
	Species	ϵ^n [-]	μ^s [-]	μ^{ro} [-]	μ^{to} [-]
Case 0	<i>all</i>	0.5	0.5	0.5	0.5
Case 1	<i>all</i>	0.1	0.5	0.5	0.5
Case 2	<i>all</i>	0.9	0.5	0.5	0.5
Case 3	<i>0-1, 0-2</i>	0.5	0.5	0.5	0.5
	<i>1-1, 2-2, 1-2</i>	0.1			
Case 4	<i>0-1, 0-2</i>	0.5	0.5	0.5	0.5
	<i>1-1, 2-2, 1-2</i>	0.9			
Case 5	<i>0-1, 0-2</i>	0.1	0.5	0.5	0.5
	<i>1-1, 2-2, 1-2</i>	0.5			
Case 6	<i>0-1, 0-2</i>	0.9	0.5	0.5	0.5
	<i>1-1, 2-2, 1-2</i>	0.5			

4.5.2.1 PARTICLE VELOCITIES AND FLOW PATTERNS

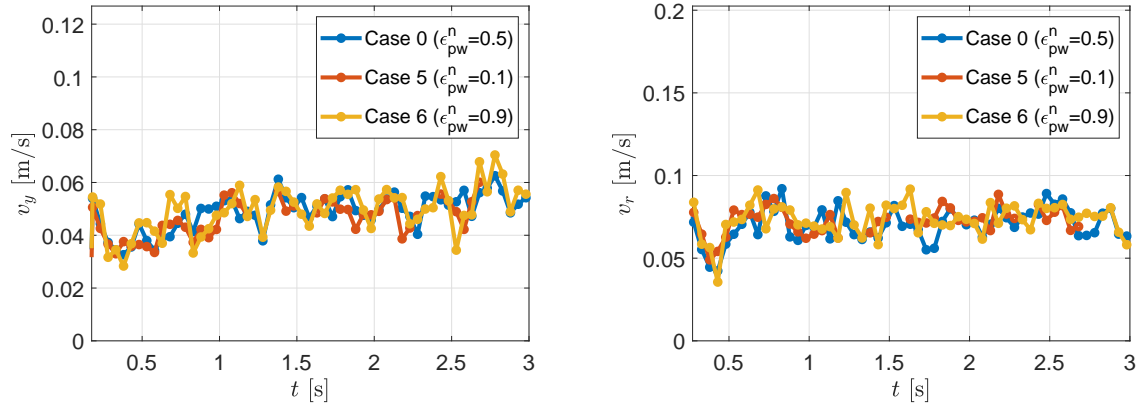
The plots in Figure 4-13 show the average axial (left) and swirl (right) velocities for the different values of ϵ^n . Although the graphs generally have the same trend, it can be seen that the average velocity is slightly higher for increasing values of the restitution coefficient. This result was expected, as a high restitution coefficient implies low energy dissipation after each collision.



(a) Restitution coefficient



(b) Particle-particle restitution coefficient



(c) Particle-wall restitution coefficient

FIGURE 4-13. Effect of (a) restitution coefficient, (b) particle-particle restitution coefficient and (c) particle-wall restitution coefficient on the average axial velocity and the average swirling velocity for $\Omega = 60$ RPM.

The average axial and (zoomed-in) radial position profiles are shown in Figure 4-14. From Figure 4-14a it appears that the effect of the restitution coefficient becomes more dominant at higher values, since the profiles of $\epsilon^n = 0.1$ and $\epsilon^n = 0.5$ are relatively close to each other when compared to the profile of $\epsilon^n = 0.9$. When comparing Figure 4-14b and c, no significant difference is seen.

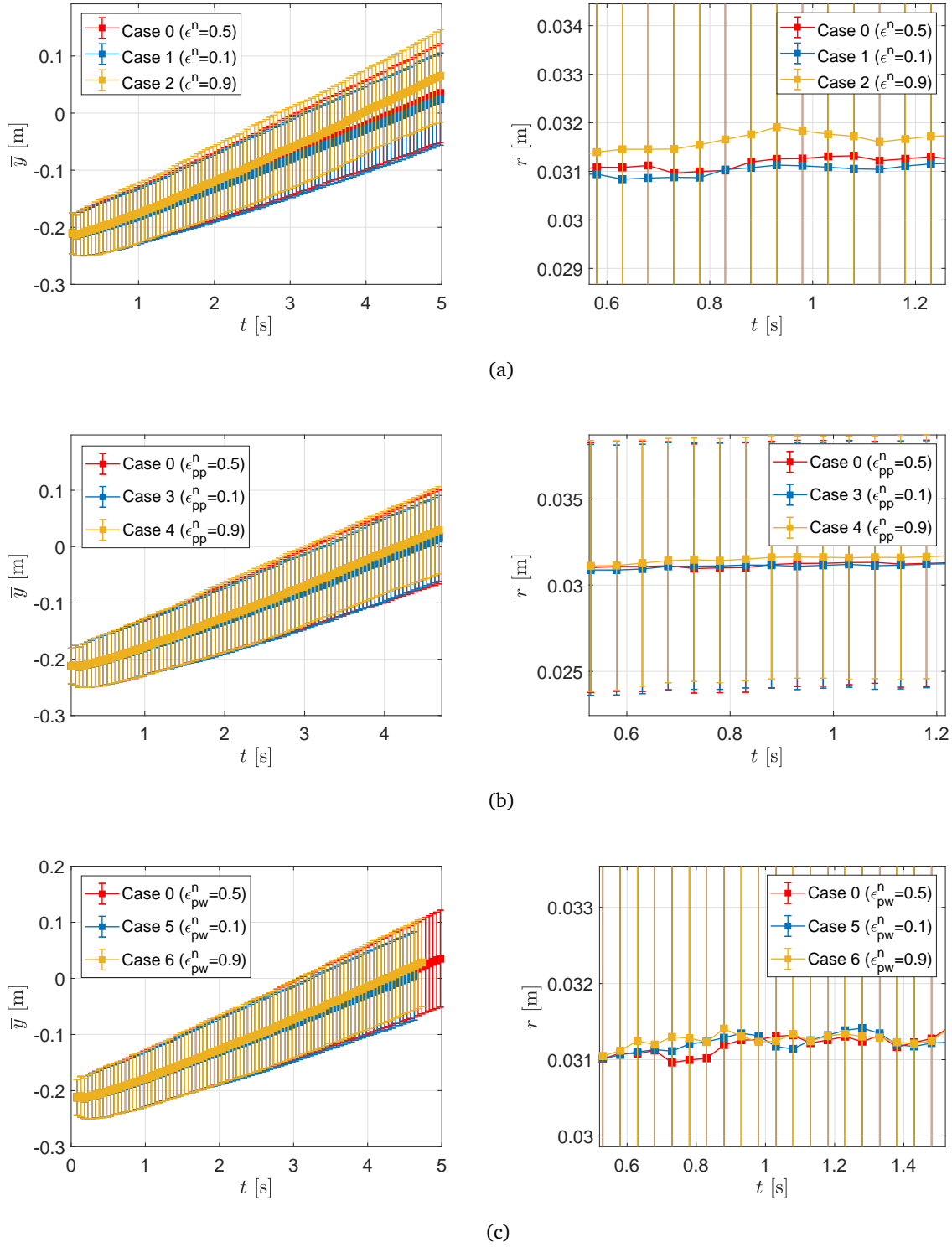


FIGURE 4-14. Effect of (a) restitution coefficient, (b) particle-particle restitution coefficient and (c) particle-wall restitution coefficient on the average axial position (left) and the average radial position (right) of the particles for $\Omega = 60$ RPM, with vertical lines representing the standard deviation.

4.5.2.2 MIXING DEGREE

The mixing indices are plotted for each case in Figure 4-15. Each plot shows that the mixing index is slightly affected by the restitution coefficient. In the first plot, the mixing index is most affected at high ϵ^n , while it remains unaffected for lower values. In the second and third plot the differences are less significant.

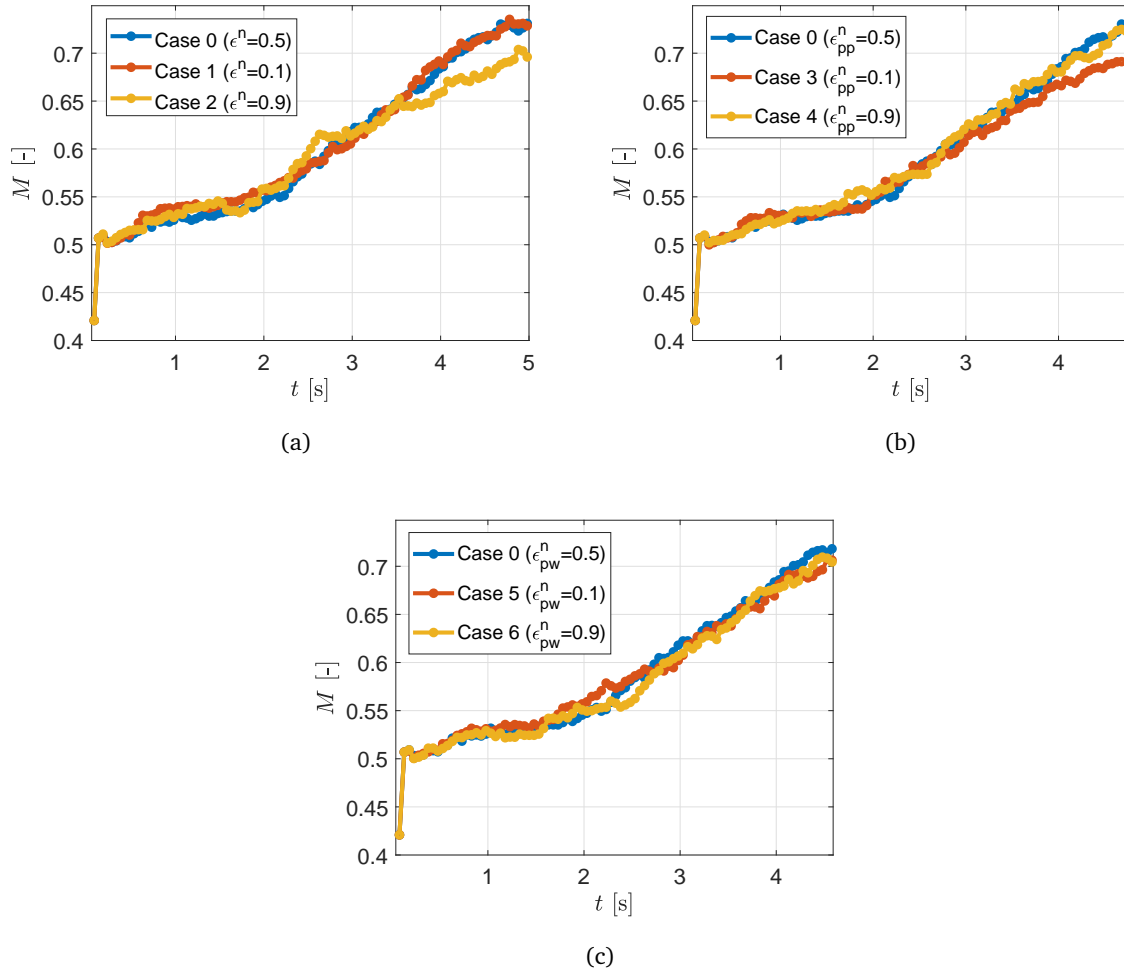


FIGURE 4-15. Effect of (a) restitution coefficient, (b) particle-particle restitution coefficient and (c) particle-wall restitution coefficient on the mixing index for $\Omega = 60$ RPM.

4.5.3 EFFECT OF COHESION

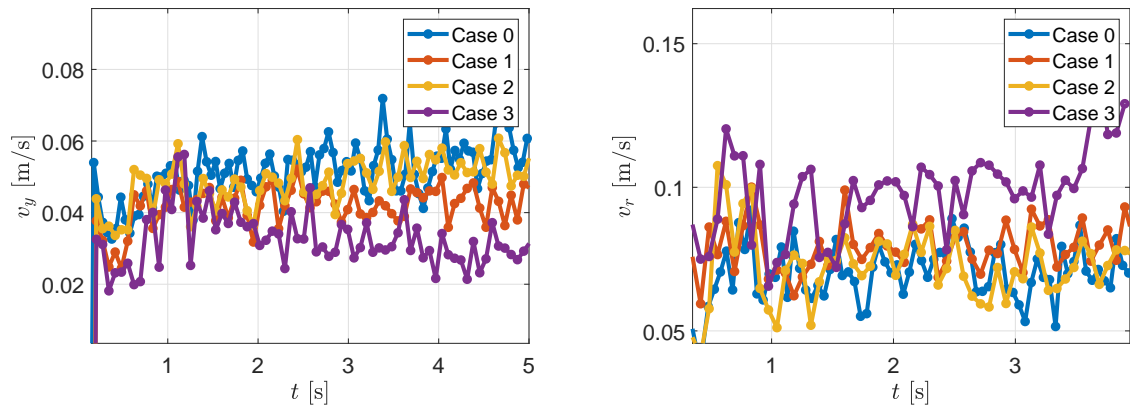
The following set of analyses is performed to assess the affect of cohesion between particles. The capillary cohesive force on a particle is determined by various factors: the liquid bridge volume V_{ij}^b , the contact angle θ_{ij}^{eff} , the surface tension σ , and the size of the particles connected by the bridge a_{ij}^{eff} . In Section 2.1.2 it was discussed that the strength of the cohesive force is usually expressed in terms of the Bond number, which is in this case the ratio of the liquid bridge force to the weight of a particle. In the case studies of Table 4.10, the cohesive capillary force (and therefore the Bond number) is varied by changing the surface tension while keeping the remaining parameters constant. The liquid volume assigned to each particle is determined by the water to sand ratio w/s , which is measured by weighing an amount of initially moist sand before and after heating it to allow the water trapped inside the material to evaporate. With $w/s = 0.029$, the liquid mass and volume are deduced and the amount of liquid is evenly distributed amongst all sand particles. Case 0 corresponds to a zero cohesion state. Case 1, 2 and 3 simply use a high, low and very high value for the surface tension, respectively. As the particle density differs for sand and cement, the Bond number is also slightly different for the two species. Both Bond numbers corresponding to the chosen value of the surface tension are presented. In all simulations, the dissipation coefficients are kept at nominal values of 0.5 and the number of particles is kept constant such that the filling fraction is approximately 0.5. The liquid intake of the particles is set to zero.

TABLE 4.10. Modeling conditions for the cohesion sensitivity analysis with 50% filling volume and rotation speed of $\Omega = 60$ RPM.

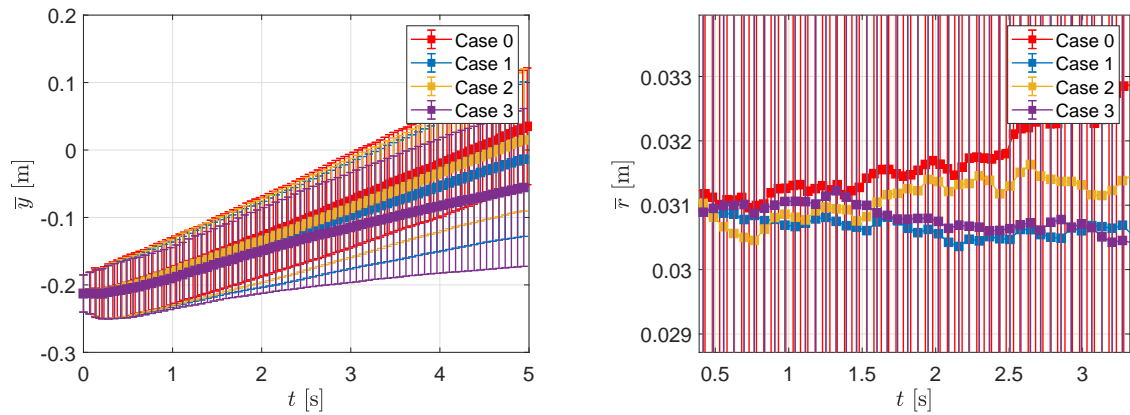
	Species	σ	V_{Lmin} [m ³]	ϵ^n, μ^ν [-]
Case 0	<i>all</i>	0.0 ($Bo = 0$)	0.0	0.5
Case 1	<i>all</i>	0.7 ($Bo = 5.6 - 7.7$)	0.0	0.5
Case 2	<i>all</i>	0.07 ($Bo = 0.56 - 0.77$)	0.0	0.5
Case 3	<i>all</i>	7 ($Bo = 56 - 77$)	0.0	0.5

4.5.3.1 PARTICLE VELOCITIES AND FLOW PATTERNS

We first analyze the effect of cohesion strength. The average axial and radial velocity profiles for the first four cases are shown in Figure 4-16a. It can be seen that the cohesion strength has a clear affect on the flow speed. As the cohesion levels decrease, the axial velocity increases since the particles can flow freely. The average radial velocity is higher as cohesion increases, since clumped particles rotate collectively, i.e., more particles are being rotated when compared to low cohesion levels, as shown in Figure 4-17. Looking at the average position profiles in Figure 4-16b, it is clear that the material transfers faster in axial direction as the cohesion levels decrease, which was already expected and can also be seen from Figure 4-17 where the snapshots are taken at $t \approx 3.97$ s for low, high and very high cohesion. The average radial position appears to decrease for high levels of cohesion, as the particles become clumped together. Figure 4-18 shows snapshots of the flow for Case 1-3. The formation of large agglomerates for high cohesion can be seen.



(a) Particle velocity profiles



(b) Particle position profiles

FIGURE 4-16. Effect of the cohesive force strength on (a) the average particle velocities and (b) the average particle positions for $\Omega = 60$ RPM.

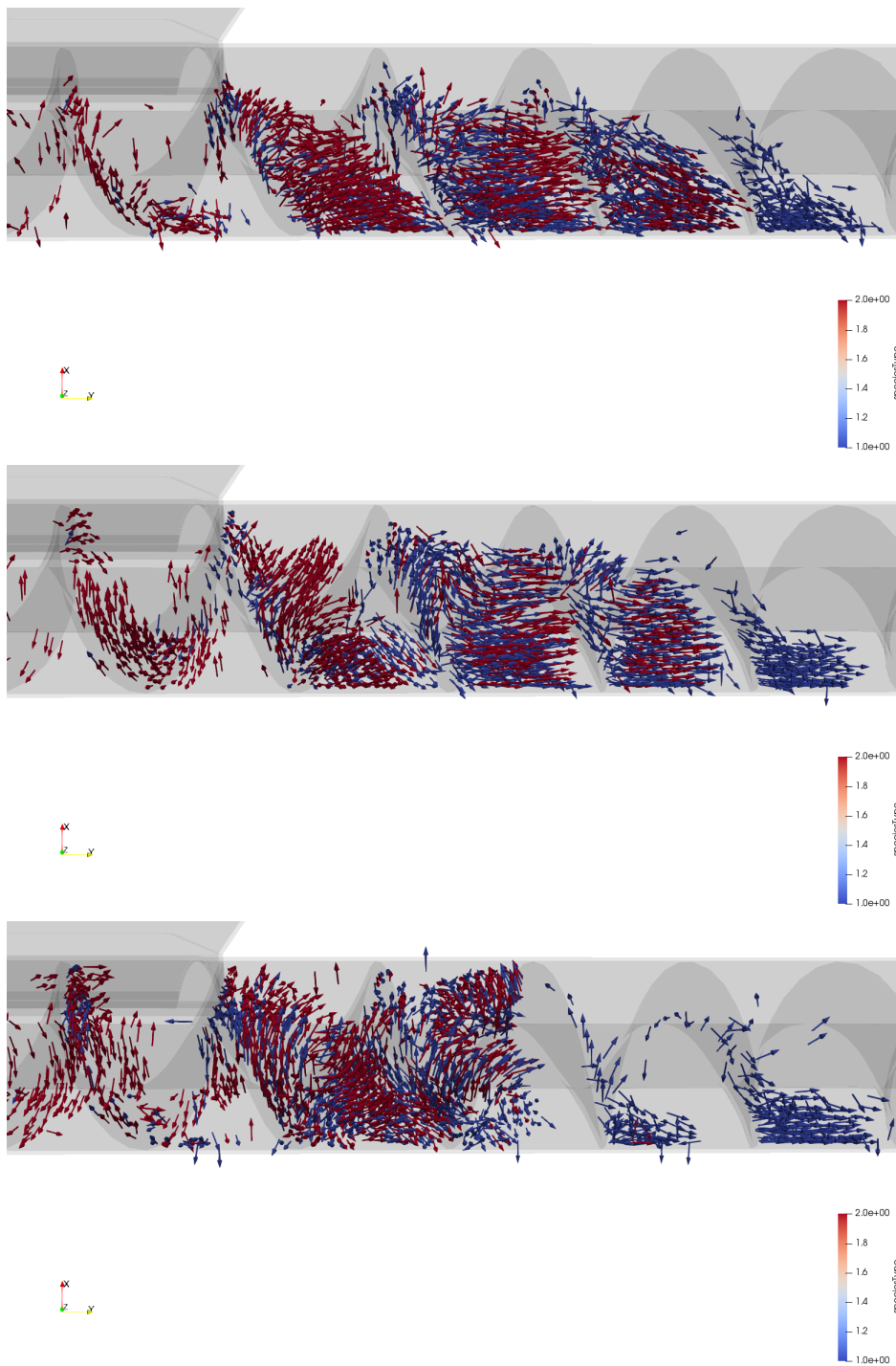


FIGURE 4-17. Effect of cohesion strength on the velocity field for low cohesion (Case2), high cohesion (Case 1) and very high cohesion (Case 3) from top to bottom; snapshots of the flow at $t \approx 3.97$ s.

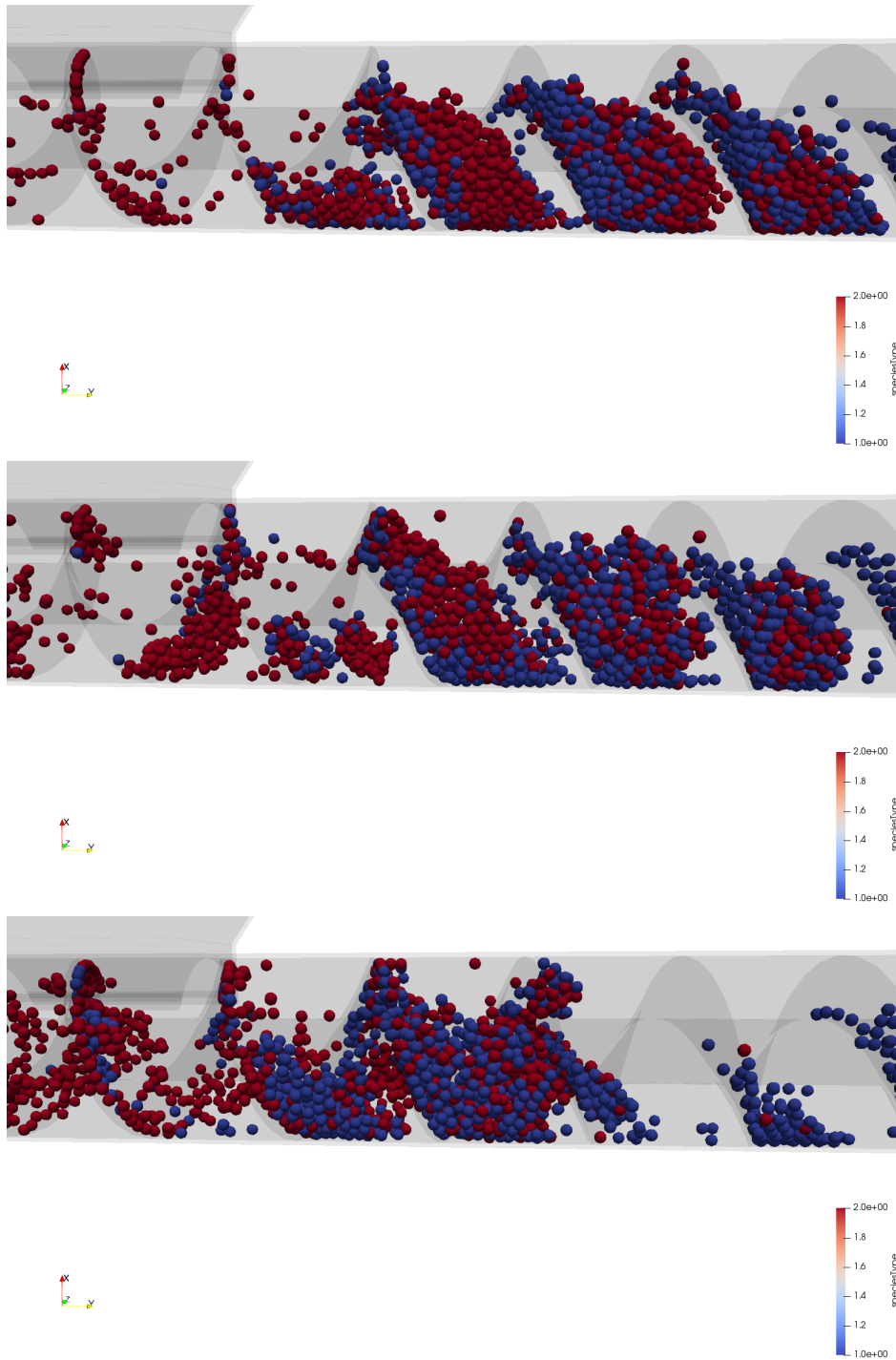


FIGURE 4-18. Particle flow for low cohesion (Case2), high cohesion (Case 1) and very high cohesion (Case 3) from top to bottom; snapshots of the flow at $t \approx 4.94$ s.

4.5.3.2 MIXING DEGREE

The mixing degree for all cases is shown in the following figure. The profiles clearly show that the particles become more unmixed as cohesion increases in this system. This indicates that the material agglomerates which are formed for strong cohesion are not effectively broken down by the mixing screw. Instead, the agglomerated particles tend to rotate collectively towards the screw outlet. Interestingly, the mixing index for $Bo = 56 - 77$ is slightly higher than the index corresponding to $Bo = 5.6 - 7.7$.

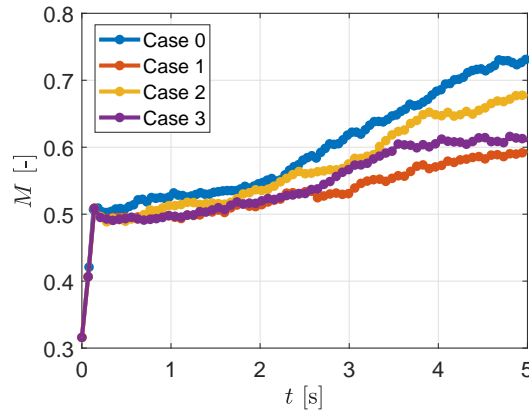


FIGURE 4-19. Effect of cohesion strength on the mixing index for $\Omega = 60$ RPM.

4.5.4 EFFECT OF WATER INTAKE

The simulations regarding the effect of cohesive strength were performed using a water intake $V_{Lmin} = 0$ for the particles. In the following case studies, the liquid intake will be varied between zero and 10% of the particle volume, as shown in the following table.

TABLE 4.11. Modeling conditions for the cohesion sensitivity analysis with 50% filling volume and rotation speed of $\Omega = 60$ RPM.

	Species	σ	V_{Lmin} [-]	ϵ^n, μ^ν [-]
Case 1	<i>all</i>	1 ($Bo = 8.1 - 11.6$)	0.0	0.5
Case 2	<i>all</i>	1 ($Bo = 8.1 - 11.6$)	$0.01 \times V_p$	0.5
Case 3	<i>all</i>	1 ($Bo = 8.1 - 11.6$)	$0.1 \times V_p$	0.5

4.5.4.1 PARTICLE VELOCITIES AND FLOW PATTERNS

Figure 4-20 shows the results for the average velocity and position profiles. It can be seen that there is a small yet noticeable effect of the liquid intake on the profiles. As some of the liquid becomes trapped in the particles, less water is available for bridge formation and it is expected that the cohesiveness will slightly decrease. The velocity profiles are in accordance with this expectation, as it was previously seen (in Section 4.5.3) that the particles' average axial velocity tends to decrease for increasing cohesion while the radial velocity increases. The results for the axial position were also expected, since

the previous results showed similar trends for increasing/decreasing cohesiveness.

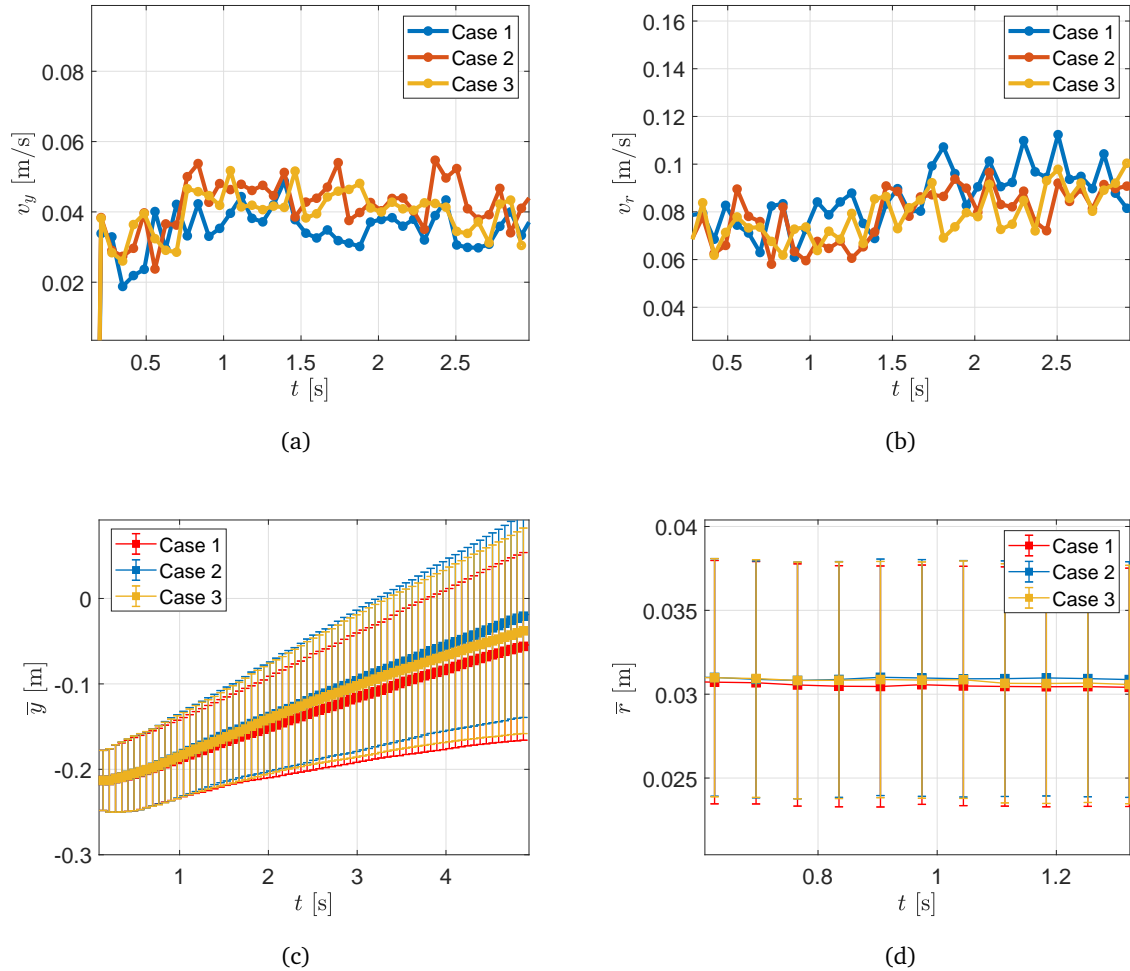


FIGURE 4-20. Effect of the screw design on (a) the average axial velocity, (b) the average radial velocity, (c) the average axial position and (d) the average (zoomed-in) radial position for all the case studies at $\Omega = 60$ RPM.

4.5.4.2 MIXING DEGREE

The results for the mixing index are shown in the following figure. Apparently, the liquid intake level has a noticeable effect on the degree of mixing. The mixing index is highest for the case of largest liquid intake (i.e., lowest cohesiveness). Surprisingly, the lowest value is not obtained for the case of highest cohesiveness.

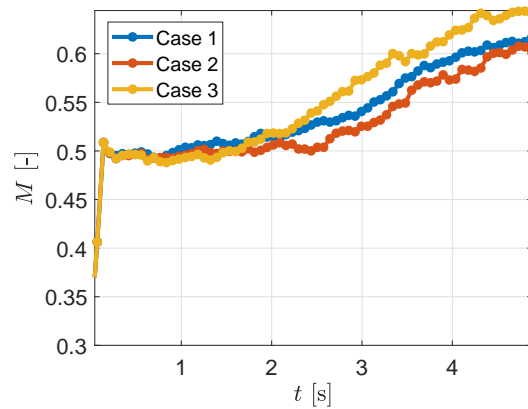


FIGURE 4-21. Effect of the liquid intake on the mixing index at $\Omega = 60$ RPM.

4.6 EFFECT OF MIXING ELEMENT GEOMETRY

In Section 4.5, several sensitivity analyses were performed to scrutinize the effect of the model parameters on the flow behavior and mixing index. From the literature survey presented in Section 2.4.2 it is known that the mixer geometry also affects the flow in a screw conveyor. For example, the study by Pezo et al. [58, 59] showed that adding additional elements to the screw results in prolonged transporting paths and increased velocities of *dry* particles inside the conveyor, which may result in enhanced mixing. One of the modified designs in their study is a screw with an additional (straight) strip aligned with the shaft of the screw. A similar model is developed (Figure 4-22) and will be used to assess whether the modified design indeed results in higher velocities and enhanced mixing. Contrary to the study by Pezo et al., the simulations are performed for moist particles at different cohesion strengths, as shown in Table 4.12. Each case study is performed using the original and modified design and the results are compared as follows.

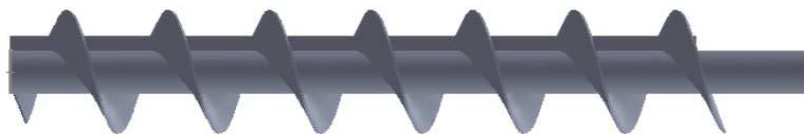
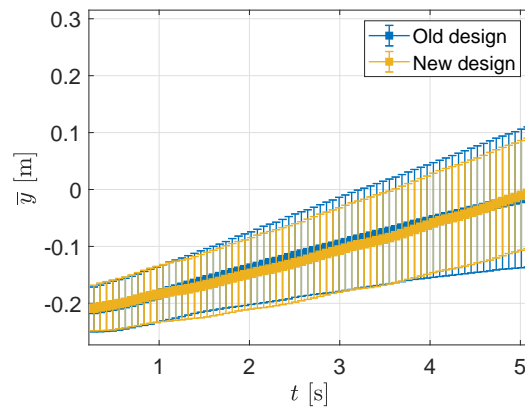


FIGURE 4-22. Modified screw, similar to a design proposed by Pezo et al. [58, 59], which is expected to enhance mixing.

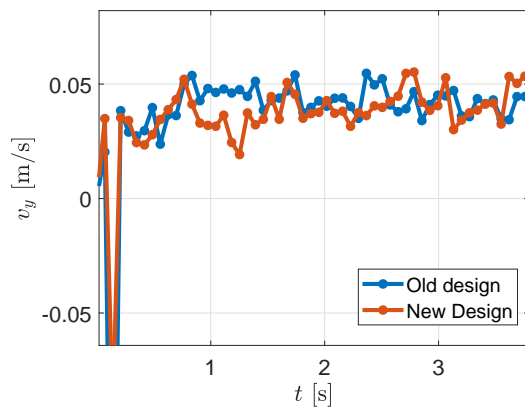
TABLE 4.12. Modeling conditions for the cohesion sensitivity analysis with 50% filling volume and rotation speed of $\Omega = 60$ RPM.

	Species	σ	$V_{L_{sand}}$ [m ³]	ϵ^n, μ^ν [-]
Case 1	<i>all</i>	1 ($Bo = 8.1 - 11.6$)	0.0	0.5
Case 2	<i>all</i>	7 ($Bo = 56 - 77$)	0.0	0.5

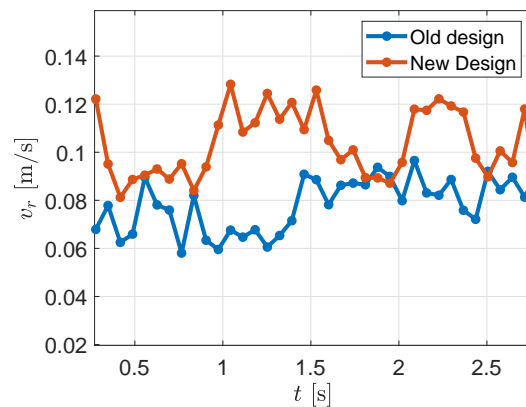
Figure 4-23 shows the flow and mixing results of the new screw design in comparison to the original design for Case 1. The first plot indicates that the material retention time is practically the same for both designs, while the average velocity plots reveal that the radial velocity is significantly increased for the modified screw design. These results correspond to the findings of Pezo et al. [58, 59], despite the fact that the authors considered free-flowing particles in their research while cohesive particles are used in this study. The last plot shows a significant increase in the mixing index when the modified screw is used. Figure 4-24 shows snapshots of the flow for the original design (top) and the modified design (bottom).



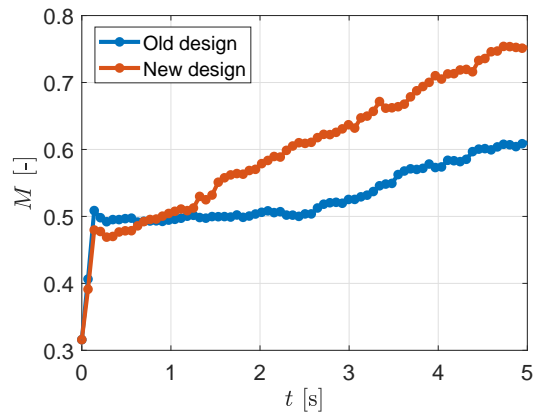
(a)



(b)



(c)



(d)

FIGURE 4-23. Effect of the screw design on (a) the average axial particle position, (b) the average axial particle velocity, (c) the average radial particle velocity and (d) the mixing index for Case 1 at $\Omega = 60$ RPM.

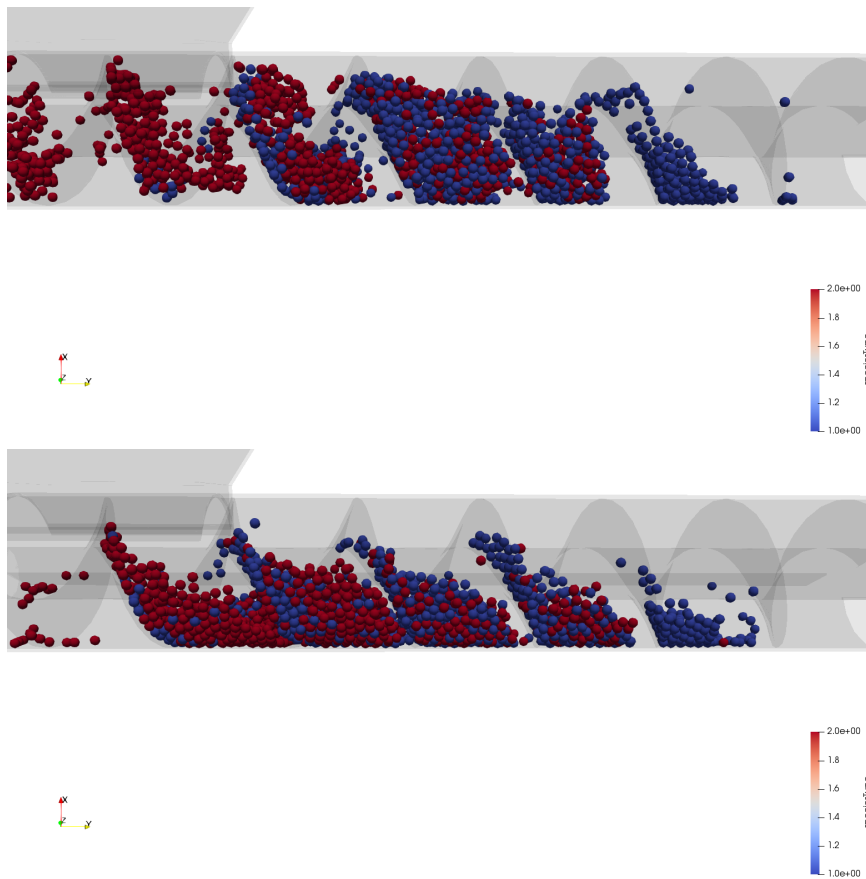
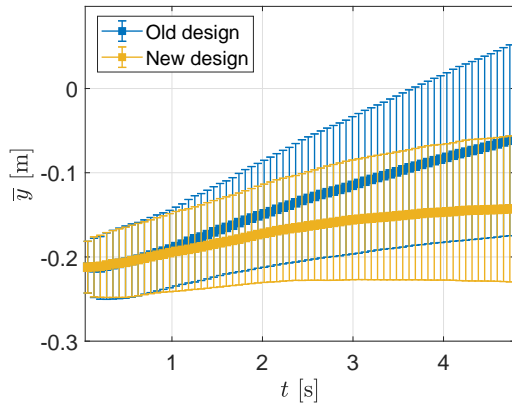
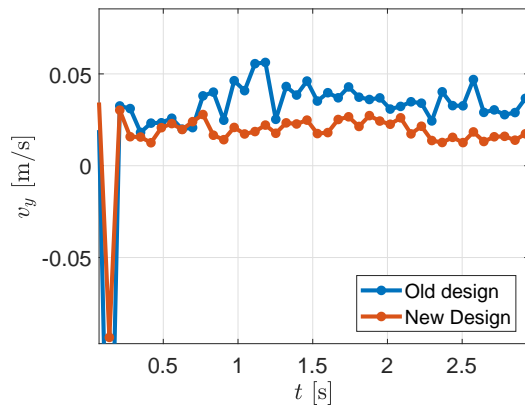


FIGURE 4-24. Particle flow using the original design (top) and the modified design (bottom) for Case 1; snapshots of the flow at $t \approx 3.97$ s.

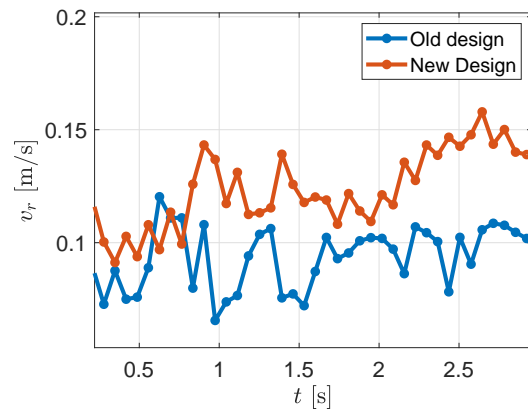
Figure 4-25 shows the results for Case 2. The flow behavior is very different than for Case 1. The residence time of the particles is no longer constant; the material travels much slower in the conveyor with the modified screw. Also, the mixing index increases more rapidly when using the modified design, but eventually reaches approximately the same value as for the original design. This indicates that if cohesion becomes very strong, then the modified geometry of Figure 4-22 does not make a significant difference and other options must be considered. Figure 4-26 shows snapshots of the flow for the original design (top) and the modified design (bottom).



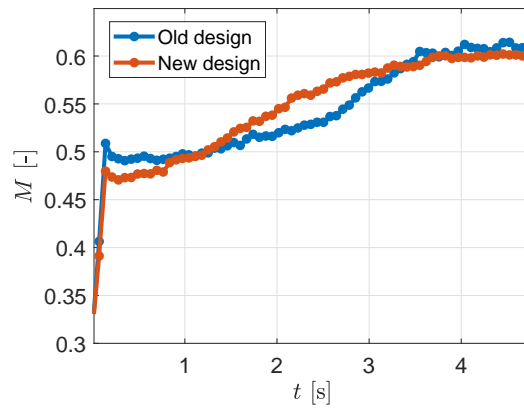
(a)



(b)



(c)



(d)

FIGURE 4-25. Effect of the screw design on (a) the average axial particle position, (b) the average axial particle velocity, (c) the average radial particle velocity and (d) the mixing index for Case 2 at $\Omega = 60$ RPM.

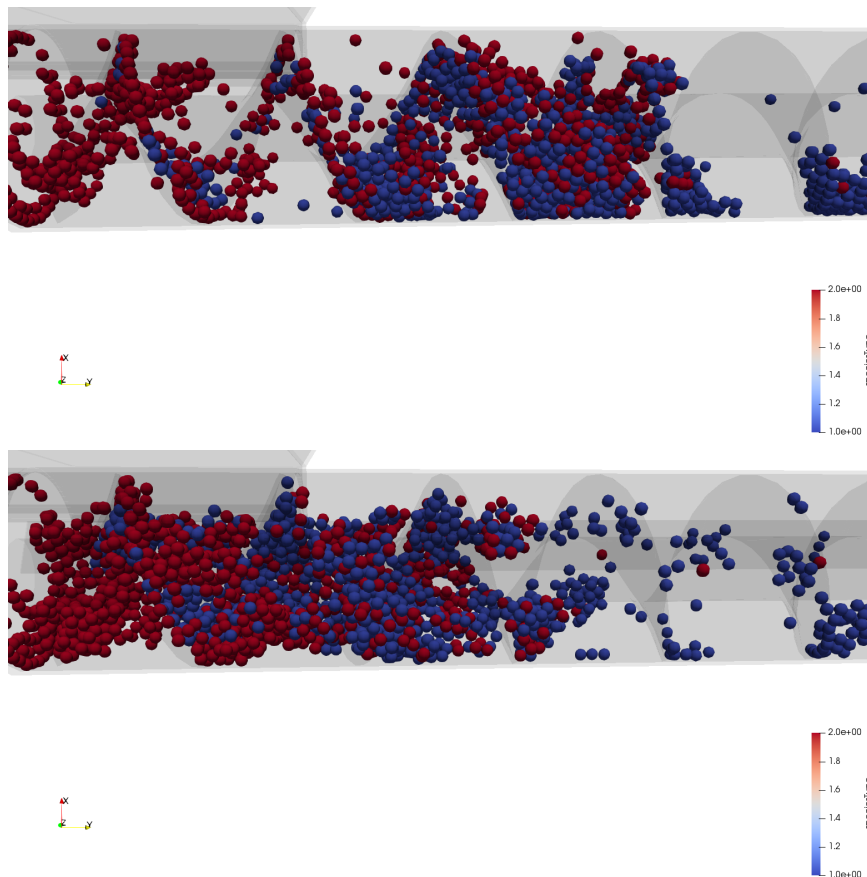


FIGURE 4-26. Particle flow using the original design (top) and the modified design (bottom) for Case 2; snapshots of the flow at $t \approx 4.73$ s.

5

DISCUSSION & RECOMMENDATIONS

5.1 CONCLUSIONS

The goal of this study was to perform the first steps in modeling a continuous concrete mixing process using the discrete element method in MercuryDPM. In this regard, the focus was limited to the so-called “dry-mixing” unit, where moist concrete constituents are pre-blended in a screw conveyor while being transported to the main mixer. A coarse-grained particle size and mono-sized spheres were chosen to model both sand and cement particles to reduce the computational run time to a reasonable level. Hence, the model is not able to predict phenomena such as segregation due to difference in particle size. Also, homogeneity on the particle scale cannot be studied. Nonetheless, the model can be used to gain a general understanding of the transportation and mixing phenomena of the material in a screw-conveyor system.

The first step in performing simulations was to determine a reasonable amount of coarse particles for the analyses. The particle resolution analysis was performed by arbitrarily choosing particle sizes which are much larger than the actual average size of cement and up to 3 times the average size of sand. Three cases were considered: 2000, 5000 and 10000 particles. By scaling the particle size, the particle density was also adjusted in order to maintain the same bulk density of both materials in the simulation. It was found that as the particle size decreases, and thus the number of particles increases, the velocity profiles coincide more closely.

Next, sensitivity analyses were performed to scrutinize the effects of friction coefficients, normal restitution coefficient and cohesive strength on flow patterns and mixing behavior of sand and cement in the screw conveyor. This provided preliminary indications of which parameters should be measured and where the future calibration or material properties measurement effort should be focused. The simulation results showed that sliding friction has a dominant effect on the mixing kinetics. More

specifically, it was found that increasing the sliding friction coefficient can promote particle recirculation and therefore enhance mixing. On the other hand, rolling friction affects mixing to a lesser extent and torsion friction effects are insignificant. Since sliding friction was found to be very important, its effect was studied in more detail by distinguishing between particle-wall and particle-particle friction. It was found that particle-wall friction is significant, while particle-particle friction seems less important at high values. The restitution coefficient was found to have a more or less insignificant impact on flow and mixing behavior, especially when only the particle-particle or particle-wall restitution coefficient is varied. When both are set to a high value (0.9), the flow and mixing behavior changes slightly. Finally, it was seen that cohesion strongly affects both flow through the screw conveyor and mixing behavior. First of all, the material travels more slowly in axial direction as the cohesive forces become stronger. On the other hand, radial transportation is enhanced for higher cohesion, since the particles clump together easily for high cohesive forces and are consequently rotated in a collective manner. The mixing index seems to decrease with increasing cohesion, suggesting that the simple screw design is not capable of breaking material agglomerates. Liquid intake levels show to have a small effect on the flow behavior and a noticeable effect on the degree of mixing when varying the liquid intake of the particles in the range of 0 – 10%.

The final part of this research presents two case studies in which a modified design of the rotor (from a previous study in literature) is used, to assess how the flow and mixing behavior of wet material changes. The literature study shows that the specific modified design results in enhanced mixing behavior of dry, free-flowing materials. In this study, it appears that the average radial velocity increases and better mixing occurs to some degree using the modified design. For very high Bond numbers, the mixing index does not improve significantly using that specific new design. Although many other designs are possible and can be investigated further, the goal of the two case studies was to illustrate how the model may be used to redesign a mixer geometry if the correct material properties are known.

5.2 RECOMMENDATIONS AND FUTURE WORK

The results of this work provide insight into moist granular flows, which are of high relevance to concrete mixing and other fields in the powder processing industry. The sensitivity analyses were performed by changing parameters one at a time to assess their individual effects on the flow and mixing behavior. This method is generally observed in literature as a first step in the calibration process. More elaborate sensitivity analyses can also be performed by analyzing the cross-correlations between parameters, i.e., changing multiple parameters per case study. Such an analysis is far more complex, as the number of parameter combinations is large. Hence, a more systematic approach based on statistical methods (such as, for example, performed in [82]) would be required in the future. Although the developed model was able to perform the simple sensitivity analyses of the material properties, this model is only a small step towards the full understanding of concrete mixing which includes significantly higher liquid contents than assumed in this study, and other complex phenomena such as hydration. While the findings of the sensitivity study are useful, the most important aspect which would allow the model to be implemented for equipment (re)design is the calibration process, which is currently lacking. It is therefore recommended to perform a more detailed analysis of the parameter dependencies through bulk calibration experiments and validate the model in order to eventually propose an improved design for the screw conveyor. Also, a more extensive particle resolution analysis is required in order to determine to which degree the particles can be upscaled while maintaining

accuracy of the predictions. This can be done by comparing experimental flow results with simulation results where various particle sizes are used.

The simulations were performed in MercuryDPM using the *LiquidFilmParticle* package, which is applicable to model the phenomena associated with moist particles. The package currently requires further development to include for parallel computing. One of the main difficulties encountered during this project was performing the simulations in a reasonable amount of time, as parallel computing was not an option. For this reason, the choice was made to limit the number of particles in the simulation by not filling the hopper with material, but rather using a small amount of material in the conveyor. Hence, the “continuous” mass flow behavior could not be analyzed as no new material entered the conveyor. This is an interesting topic to study in the future, as one of the key design objectives of a screw conveyor system is to deliver a steady, constant mass flow rate. Another option for saving computational effort is the use of periodic sections. This method has been applied to screw conveyors in other works found in literature, and is currently also applicable in MercuryDPM.

REFERENCES

- [1] R. A. Busewell, W.R. Leal de Silva, S.Z. Jones, and J. Dirrenberger. 3D printing using concrete extrusion: a roadmap for research. *Cement and Concrete Research*, 112:37–49, 2018.
- [2] James K. Wight and James G. MacGregor. *Reinforced Concrete: Mechanics and Design*. Pearson Education, Inc., fifth edition, 2009.
- [3] P. Kumar Mehta and Paulo J. M. Monteiro. *Concrete Microstructure, Properties, and Materials*. The McGraw-Hill Companies, Inc., third edition, 2006.
- [4] Freek Bos, Rob Wolfs, Zeeshan Ahmed, and Theo Salet. Additive manufacturing of concrete in construction: potentials and challenges of 3d concrete printing. *Virtual and Physical Prototyping*, 2016.
- [5] 4TU.Federation. 4TU.Bouw 2016 ‘newspaper’, 2017.
- [6] Dennis Horsthuis, Django Grunder, Wouter Postel, Niek Slebos, Mart Ningbers, Jeroen Weda, Robbert Helthuis, and Marcin Kuchta. Het optimaliseren en verschalen van het huidige 3D-printsysteem. resreport, Saxion University of Applied Sciences, July 2018.
- [7] Chiara F. Ferraris. Concrete Mixing Methods and Concrete Mixers: State of the Art. *Journal of Research of the National Institute of Standards and Technology*, 106(2):391–399, 2001.
- [8] Steven Jon Brown. Design of a High-Shear Geopolymer Concrete Mixer. resreport, University of Southern Queensland, Faculty of Engineering and Surveying, 2011.
- [9] Knut Krenzer. *Development of a state-dependent DEM material model to simulate mixing processes of fresh concrete*. phdthesis, Technische Universität Dresden, 2016.
- [10] K. Kesava Rao and Prabhu R. Nott. *An Introduction to Granular Flow*. Cambridge University Press, New York, 2008.
- [11] R. M. Nedderman. *Statics and Kinematics of Granular Materials*. Cambridge University Press, 1992.
- [12] Anita Mehta, editor. *Granular Matter: An Interdisciplinary Approach*. Springer-Verlag New York, Inc., 1994.
- [13] Yoël Forterre and Olivier Pouliquen. Granular flows. *Séminaire Poincaré XIII*, 2009.
- [14] Heinrich M. Jaeger, Sidney R. Nagel, and Robert P. Behringer. The Physics of Granular Materials. *Physics Today*, 1996.
- [15] Heinrich M. Jaeger and Sidney R. Nagel. Physics of the Granular State. *Science*, 255, 1992.
- [16] Namiko Mitarai and Franco Nori. Wet granular materials. *Advances in Physics*, 55(1-2):1–45, January 2006.
- [17] W. L. Sluyter and P. C. Kreijger. Qualitative explanation of the fluidity of fresh concrete. Technical report, Technische Hogeschool Eindhoven. Afd. Bouwkunde, Laboratorium Materiaalkunde, 1978.

- [18] Jesper Knijnenburg. Influence of vibrations on particle flow behaviour. Master's thesis, TU Delft, 2008.
- [19] Steven T. Nase, Watson L. Vargas, Adetola A. Abatan, and J. J. McCarthy. Discrete characterization tools for cohesive granular material. *Powder Technology*, 116:214–223, 2001.
- [20] Todd A. Kingston. Granular mixing visualization and quantification in a double screw mixer . matheresis, Iowa State University, Ames, Iowa, 2013.
- [21] P. M. C. Lacey. Development in the theory of particle mixing. *Journal of Applied Chemistry*, 4:257–268, 1954.
- [22] John Bridgewater. Mixing of powders and granular materials by mechanical means—A perspective. *Particuology*, 10:397–427, 2010.
- [23] An-Ni Huang and Hsiu-Po Kuo. Developments in the tools for the investigation of mixing in particulate systems—A review. *Advanced Powder Technology*, 25:163–173, 2014.
- [24] Guoping Lian, Colin Thornton, and Michael J. Adams. Discrete particle simulation of agglomerate impact coalescence. *Chemical Engineering Science*, 53(19):3381–3391, 1998.
- [25] Kimiaki Washino, Ei L. Chan, Taku Matsumoto, Seiji Hashino, Takuya Tsuji, and Toshitsugu Tanaka. Normal viscous force of pendular liquid bridge between two relatively moving particles. *Journal of Colloid and Interface Science*, 494:255–265, 2017.
- [26] Yoshitsugu Muguruma, Toshitsugu Tanaka, and Yutaka Tsuji. Numerical simulation of particulate flow with liquid bridge between particles (simulation of centrifugal tumbling granulator). *Powder Technology*, 109:49–57, 2000.
- [27] Saurabh Sarkar and Bodhisattwa Chaudhuri. DEM modeling of high shear wet granulation of a simple system. *Asian Journal of Pharmaceutical Sciences*, 13:220–228, 2018.
- [28] Simon M. Iveson, James D. Litster, Karen Hapgood, and Bryan J. Ennis. Nucleation, growth and breakage phenomena in agitated wet granulation processes: a review. *Powder Technology*, 117:3–39, 2001.
- [29] P. Suresh, I. Sreedhar, R. Vaidhiswaran, and A. Venugopal. A comprehensive review on process and engineering aspects of pharmaceutical wet granulation. *Chemical Engineering Journal*, 328:785–815, 2017.
- [30] J. A. Westerhuis. Multivariate statistical modelling of the pharmaceutical process of wet granulation and tableting, 1997.
- [31] Ksenija Vasilić. *A Numerical Model for Self-Compacting Concrete Flow through Reinforced Sections: a Porous Medium Analogy*. phdthesis, Technischen Universität Dresden, 2016.
- [32] P. A. Cundall and O. D. L. Strack. A discrete numerical model for granular assemblies. *Geotechnique*, 29(1):47–65, 1979.
- [33] MercuryLab. The Fundamentals of Discrete Particle Simulations, October 2018.
- [34] A. Ghaderi. On Characterization of Continuous Mixing of Particulate Materials. *Particulate Science and Technology*, 21:1–12, 2003.
- [35] M. Poux, P. Fayolle, J. Bertrand, D. Bridoux, and J. Bousquet. Powder mixing: some practical rules applied to agitated systems. *Powder Technology*, 68:213–234, 1991.
- [36] Chawki Ammarcha, Cendrine Gatamel, Jean-Louis Dirion, M. Cabassud, and Henri Berthiaux. Continuous powder mixing of segregating mixtures under steady and unsteady state regimes: Homogeneity assessment by real-time on-line image analysis. *Powder Technology*, 315:39–52, 2017.
- [37] Yijie Gao. *MODELING AND ANALYSIS OF CONTINUOUS POWDER BLENDING*. phdthesis,

- Graduate School-New Brunswick Rutgers, The State University of New Jersey, 2012.
- [38] Patricia M. Portillo, Marianthi G. Ierapetritou, and Fernando J. Muzzio. Effects of rotation rate, mixing angle, and cohesion in two continuous powder mixers-A statistical approach. *Powder Technology*, 194:217–227, 2009.
- [39] Patricia M. Portillo, Fernando J. Muzzio, and Marianthi G. Ierapetritou. Using Compartment Modeling to Investigate Mixing Behavior of a Continuous Mixer. *J Pharm Innov.*
- [40] Yuanyun Wen, Malin Liu, Bing Liu, and Youlin Shao. Comparative study on the characterization method of particle mixing index using DEM method. *Procedia Engineering*, 102:1630–1642, 2015.
- [41] W. Godlieb, N.G. Deen, and J.A.M. Kuipers. Characterizing solids mixing in DEM simulations. In *6th International Conference on Multiphase Flow, ICMF 2007*, 2007.
- [42] Stefan Radl, Eva Kalvoda, Benjamin J. Glasser, and Johannes G. Khinast. Mixing characteristics of wet granular matter in a bladed mixer. *Powder Technology*, 200:171–189, 2010.
- [43] Steffen Schmelzle and Herrmann Nirschl. DEM simulations: mixing of dry and wet granular material with different contact angles. *Granular Matter*, 20.
- [44] Paul W. Cleary and Matthew D. Sinnott. Assessing mixing characteristics of particle-mixing and granulation devices. *Particuology*, 6:419–444, 2008.
- [45] Matthew Sinnott and Paul Cleary. 3D DEM Simulations of a High Shear Mixer. In *Third International Conference on CFD in the Minerals and Process Industries, CSIRO, Australia*, 2003.
- [46] R. L. Stewart, J. Bridgwater, Y. C. Zhou, and A. B. Yu. Simulated and measured flow of granules in a bladed mixer – a detailed comparison. *Chemical Engineering Science*, 56:5457–5471, 2001.
- [47] F. Bertrand, L. A. Leclaire, and G. Levecque. DEM-based models for the mixing of granular materials. *Chemical Engineering Science*, 2005.
- [48] H. P. Kuo, P. C. Knight, D. J. Parker, Y. Tsuji, M. J. Adams, and J. P. K. Seville. The influence of DEM simulation parameters on the particle behaviour in a V-mixer. *Chemical Engineering Science*, 57:3621–3638, 2002.
- [49] Maitraye Sen, Subhodh Karkala, Savitha Panikar, Olav Lyngberg, Mark Johnson, Alexander Marchut, Elisabeth Schafer, and Rohit Ramachandran. Analyzing the Mixing Dynamics of an Industrial Batch Bin Blender via Discrete Element Modeling Method. *Processes*, 5(22), 2017.
- [50] Alvaro Realpe, Karen Barrios, and Martha Rozo. Assessment of Homogenization Degree of Powder Mixing in a Cylinder Rotating Under Cascading Regime. *International Journal of Engineering and Technology*, 7, 2015.
- [51] Ahmed Jarray, Vanessa Magnanimo, Marco Ramaioli, and Stefan Luding. Scaling of wet granular flows in a rotating drum. In *Powders and Grains 2017 - 8th International Conference on Micromechanics on Granular Media, Montpellier, France*, 2017.
- [52] Ahmed Jarray, Vanessa Magnanimo, and Stefan Luding. Wet granular flow control through liquid induced cohesion. *Powder Technology*, 2017.
- [53] Bodhisattwa Chaudhuri, Amit Mehrotra, Fernando J. Muzzio, and M. Silvina Tomassone. Cohesive effects in powder mixing in a tumbling blender. *Powder Technology*, 165:105–114, 2006.
- [54] J. J. McCarthy. Micro-modeling of cohesive mixing processes. *Powder Technology*, 138:63–67, 2003.
- [55] Justin W.Fernande, Paul W. Cleary, and William McBride. Effect of screw design on hopper drawdown of spherical particles in a horizontal screw feeder. *Chemical Engineering Science*,

- 66:5585–5601, 2001.
- [56] Q. F. Hou, K. J. Dong, and A. B. Yu. DEM study of the flow of cohesive particles in a screw feeder. *Powder Technology*, 256:529–539, 2014.
- [57] L. Orefice and J. G. Khinast. DEM study of granular transport in partially filled horizontal screw conveyors. *Powder Technology*, 305:347–356, 2017.
- [58] Aca Jovanović, Lato Pezo, Sanja Stanojlović, Nenad Kosanić, and Ljubinko Lević. Discrete element modelling of screw conveyor-mixers. *Hemijska industrija*, 69:95–101, 2015.
- [59] Lato Pezo, Aca Jovanović, Milada Pezo, Radmilo Čolović, and Biljana Lončar. Modified screw conveyor-mixers - Discrete element modeling approach. *Advanced Powder Technology*, 26:1391–1399, 2015.
- [60] Wei-Ren Tsai and Chun-I Lin. On the mixing of granular materials in a screw feeder. *Powder Technology*, 80:119–126, 1994.
- [61] Kei ich Tanida, Kouji Honda, Nobuaki Kawano, Toshihiro Kawaguchi, Toshitsugu Tanaka, and Yutaka Tsuji. Particle Motion in Screw Feeder Simulated by Discrete Element Method. In *IS&Ts NIP 14: 1998 International Conference on Digital Printing Technologies*, 1998.
- [62] F. Qi, T. J. Heindel, and M. M. Wright. Numerical study of particle mixing in a lab-scale screw mixer using the discrete element method. *Powder Technology*, 308:334–345, 2017.
- [63] Yunfei Shi, Xiliang Zhang Shoujuan Cui, and Kui Ma. Contact Forces in a Screw Feeding Process. *Advances in Materials Science and Engineering*, 2018.
- [64] Shuyan Wang, Haolong Li, Ruichao Tian, Ruichen Wang, Xu Wang, Qiji Sun, and Jiawei Fan. Numerical simulation of particle flow behavior in a screw conveyor using the discrete element method. *Particuology*, 43:137–148, 2019.
- [65] J. L. Plawsky, S. Jovanovic, H. Littman, K. C. Hover, S. Gerolimos, and K. Douglas.
- [66] Jeffrey S. Marshall and Shuiqing Li. *Adhesive Particle Flow – A Discrete Element Approach*. Cambridge University Press, 2014.
- [67] Stefan Luding. Cohesive frictional powders: contact models for tension. *Granular Matter*, 10:235–246, 2008.
- [68] Deliang Shi and J. J. McCarthy. Numerical simulation of liquid transfer between particles. *Powder Technology*, 184:64–75, 2008.
- [69] Roman Mani, Dirk Kadau, and Hans J. Hermann. Liquid migration in sheared unsaturated granular media. *Granular Matter*, 15:447–454, 2013.
- [70] Kimiaki Washino, Koki Miyazaki, Takuya Tsuji, and Toshitsugu Tanaka. A new contact liquid dispersion model for discrete particle simulation. *Chemical Engineering Research and Design*, 110:123–130, 2016.
- [71] Sudeshna Roy. *Hydrodynamic Theory of Wet Particle Systems*. phdthesis, University of Twente, 2017.
- [72] Adrian Jensen, Kirk Fraser, and George Laird. Improving the Precision of Discrete Element Simulations through Calibration Models. In *13th International LS-DYNA Users Conference*, 2014.
- [73] Kimiaki Washino, Ei. L. Chan, Koki Miyazaki, Takuya Tsuji, and Toshitsugu Tanaka. Time step criteria in DEM simulation of wet particles in viscosity dominant systems. *Powder Technology*, 302:100–107, 2016.
- [74] C. J. Coetzee. Review: Calibration of the discrete element method. *Powder Technology*, 310:104–142, 2017.
- [75] Nayara S. Klein, Jorg Bachmann, Antonio Aguado, and Berenice Toralles-Carbonari. Evaluation

- of the wettability of mortar component granular materials through contact angle measurements. *Cement and Concrete Research*, 42:1611–1620, 2012.
- [76] Konstantin Sobolev and Surendra P. Shah, editors. *Nanotechnology in Construction*, 2015.
- [77] Aalborg White. White Cement - Made in Denmark. Product specification sheet B10 MARKETING A/S 239.081.04/01.10.
- [78] Hamid Reza Norouzi, Reza Zarghami, Rahmat Sotudeh-Gharebagh, and Navid Mostoufi. *Coupled CFD-DEM Modeling: Formulation, Implementation and Application to Multiphase Flows*. John Wiley & Sons, Ltd, 2016.
- [79] N. J. Watson, M. J. W. Povey, G. K. Reynolds, Y. Ding, and B. H. Xu. Development of a discrete element model with moving realistic geometry to simulate particle motion in a Mi-Pro granulator. *Computers and Chemical Engineering*, 93:234–247, 2016.
- [80] A. Bakshi, M. Shahnam, A. Gel, T. Li, C. Altantzis, W. Rogers, and A.F. Ghoniem. Comprehensive multivariate sensitivity analysis of CFD-DEM simulations: Critical model parameters and their impact on fluidization hydrodynamics. *Powder Technology*, 338:519–537, 2018.
- [81] J. Schäfer, S. Dippel, and D. E. Wolf. Force Schemes in Simulations of Granular Materials. *Journal de Physique I*, 6:5–20, 1996.
- [82] Z. Yan, S. K. Wilkinson, E. H. Stitt, and M. Marigo. Discrete element modelling (DEM) input parameters: understanding their impact on model predictions using statistical analysis. *Computational Particle Mechanics*, 2:283–299, 2015.
- [83] John Newman and Ban Seng Choo, editors. *Advanced Concrete Technology - Constituent Materials*. Elsevier Ltd., 2003.
- [84] Isabella Sharpley. The Effect of Hydration on the Microstructural Properties of Individual Phases of Ordinary Portland Cement. mathesis, University College London, Dept. Physics and Astronomy, April 2015.
- [85] Karen Louise Scrivener. *The Development of Microstructure During the Hydration of Portland Cement*. phdthesis, University of London, July 1984.
- [86] Ruzena Chamrova. *Modelling and Measurement of Elastic Properties of Hydrating Cement Paste*. phdthesis, École Polytechnique Fédérale de Lausanne, 2010.
- [87] Jonathan Bartholomew Estrada. Scaling the Rock - A Micromechanical Model for the Elastic Properties of Hydrated Cement Pastes. BSc. Thesis, June 2011.
- [88] M. L. Gambhir. *Concrete Technology*, chapter Chemical Admixtures and Mineral Admixtures, pages 102–144. McGraw Hill education (India) Private Limited, fifth edition, 2013.
- [89] Konstantin Kovler and Nicolas Roussel. Properties of fresh and hardened concrete. *Cement and Concrete Research*, 41:775–792, 2011.
- [90] M. Abdullahi. Effect of aggregate type on Compressive strength of concrete. *International Journal of Civil and Structural Engineering*, 2(3), 2012.
- [91] ConcreteBasics.org. High Performace Concrete. Online article, 2014.
- [92] CIP 37 - Self Consolidating Concrete (SCC). techreport, National Ready Mixed Concrete Association (NRMCA), 2004.
- [93] Hajime Okamura and Masahiro Ouchi. Self-Compacting Concrete. *Journal of Advanced Concrete Technology*, 1(1):5–15, April 2003.
- [94] Biranchi Panda, Yi Wei Tay, Suvash Chandra Paul, Tan Ming Jen, Kah Fai Leong, and Ian Gibson. Current Challenges and Future Perspectives of 3D Concrete Printing. In *2nd International Conference on Progress in Additive Manufacturing (Pro-AM 2016)*, May 2016.

- [95] Peng Wu, Jun Wang, and Xiangyu Wang. A critical review of the use of 3D printing in the construction industry. *Automation in Construction*, 68:21–31, 2016.
- [96] Zeina Malaeb, Hussein Hachem, Adel Tourbah, Toufic Maalouf, Nader El Zarwi, and Farook Hamzeh. 3D Concrete Printing: Machine Mix and Design. *International Journal of Civil Engineering and Technology (IJCIET)*, 6, 2015.
- [97] Behzad Nematollahi, Ming Xia, and Jay Sanjayan. Current Progress of 3D Concrete Printing Technologies. In *34th International Symposium on Automation and Robotics in Construction*, 2017.
- [98] Properties of 3D Printable Concrete. In Gideon P. A. G. van Zijl, Suvash Chandra Paul, and Ming Jen Tan, editors, *2nd International Conference on Progress in Additive Manufacturing (Pro-AM 2016)*, May 2016.
- [99] Don de Koker. Manufacturing Processes for Engineered Cement-Based Composite Material Products. Master's thesis, University of Stellenbosch, December 2004.
- [100] Syntron Material Handling. Link-belt screw conveyors. Product catalogue.
- [101] K. Krenzer, V. Mechtcherine, and U. Palzer. Simulating mixing processes of fresh concrete using the discrete element method (DEM) under consideration of water addition and changes in moisture distribution. *Cement and Concrete Research*, 115:274–282, 2018.
- [102] H. Beitzel and Y. Charonnat. Assessment and classification of performance mixers. *Materials and Structures*, 36:250–264, May 2003.



CONCRETE MIXING BASICS

INTRODUCTION

Concrete is a complex material consisting of various constituents, each of which are required to achieve the desired properties of the final (hardened) product. The aim of this section is to form a basis for understanding concrete mixing processes in general. In order to achieve this goal, a literature study is conducted in order to understand the specific requirements for different concrete types and the variety of concrete mixing equipment available on the market.

A.1 GENERAL MATERIAL COMPONENTS

The substance referred to as “concrete” is constituted of various particles, typically ranging from the nanometer to the centimeter scale. Generally speaking, concrete is a combination of three different material categories: the aggregates (sand, gravel or crushed rock), the binder (a paste of cement and water) and the admixtures (additives). Once the dry ingredients are combined with water, chemical reactions occur which change the mixture composition and flow behavior in time. A short description of typical concrete components and a discussion of the material properties are provided as follows.

A.1.1 CEMENT PASTE

Cement paste is the product which is formed through chemical reactions once dry cement and water come into contact with each other during concrete production. Hydraulic-cement concretes are most commonly used worldwide, where the binding component in the concrete is a mixture of hydraulic cement and water. The term “hydraulic” refers to the fact that this type of cement is able to set and harden only after it is brought into contact with water. Portland cement is the most well-known hydraulic cement, which is essentially a mixture of two raw materials: limestone or chalk (typically 80%) which provides CaO, and shay or clay, which is the source of other necessary oxides such as

SiO_2 , Al_2O_3 and Fe_2O_3 . The raw materials are ground to fine powders and sent to a rotary kiln at approximately 1500 °C, where the powder is partially melted to form a granular material known as clinker. The principal chemical compounds present in most European clinkers are the calcium silicates known as alite (C_3S , ca.50 wt-%), belite (C_2S , ca.25 wt-%), aluminate (C_3A , ca.10 wt-%) and ferite (C_4AF , ca.10 wt-%). The clinker is cooled down and ground with gypsum ($\text{C}\overline{\text{S}}\text{H}_2$, ca.2 wt-%) to produce cement [83]. When the dry constituents of concrete are combined, no binding of fine and coarse aggregates occurs. However, once water is added, the cement acquires its adhesive property through chemical reactions of calcium silicate and aluminate phases in the cement with water. This process, referred to as “hydration”, can be thought of as a sequence of two steps:

1. *Dissolution*

The cement minerals C_3S and C_3A are highly soluble, i.e., they dissolve rapidly once water is added to cement. Thus, the mixing water quickly transforms from pure H_2O into an aqueous solution containing various ions. Eventually the solution becomes supersaturated, meaning that some of the ions have a tendency to combine into new solid phases. Apparently, alite reacts with water to form a calcium-silicate-hydrate (“C-S-H”) crystalline gel and a large amount of CH, also known as portlandite. A similar gel-like product (ettringite) is formed from the hydration of aluminate. These hydration products are formed around unreacted cement particles, separating them from the rich ionic solution and thereby preventing further dissolution [84]. The dissolution process is of short duration, lasting for only a few minutes. During the following few hours (the induction period), the hydration process is stagnant and the amount of produced hydrates no longer increases.

2. *Precipitation*

During this step, the “protective” hydrates layer around the anhydrous cement grains disrupts and allows the hydration process to continue [85]. During this second hydration stage, the reaction rate initially increases rapidly and reaches a maximum at approximately 24 hours after mixing. Afterwards, the reaction rate decreases and the hydration continues slowly for several months. The final hardened product is mostly comprised of C-S-H solids, which is responsible for the mechanical properties of the structure and comprises about 60% of the final volume [86]. A close analysis of the cement microstructure shows that the C-S-H gel phase is actually a collection of “basic units” (globules) which can be described as tiny, layered C-S-H particles (Figure 2-1). At a particular instance, there are regions of less dense (more porous) gel (low density C-S-H), which occupy the space where water was originally present, while other regions, originally occupied by cement particles, are more dense (high density C-S-H). As the hydration reaction continues, the globules become more tightly packed.

The amount of water which is added relative to the amount of cement is an important parameter (called the water/cement ratio or “ w/c ”) in concrete production. Ideally, the w/c must be designed such that almost all of the water is utilized in the hydration process, leaving only a small amount of excess water to evaporate. If the value of w/c is too low, the concrete mix will be stiff and clumpy; however, the final concrete product is stronger and more durable as w/c increases towards an optimal value. When the w/c ratio is too high, the strength of the hardened concrete decreases. This makes sense, considering the fact that the space occupied by water in fresh concrete is replaced by pores in the final product. Thus, the value of w/c should be as low as possible, i.e., it should be just high enough such that it is workable for the intended application.

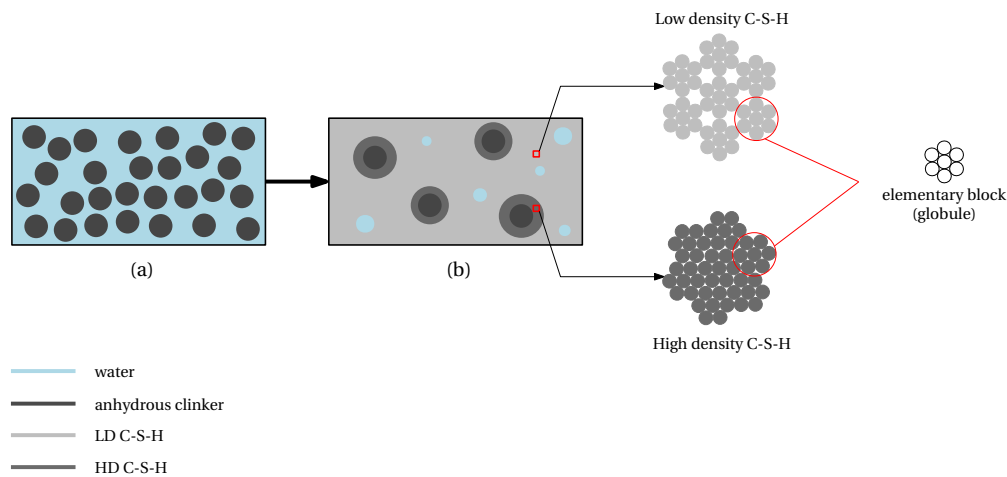


FIGURE A.1. Illustration of cement hydration with: (a) initial stage of clinker-water contact and (b) later stages of hydration, where high-density C-S-H gel is present around clinker particles in an overall matrix of low-density C-S-H gel; adapted from [87].

A.1.2 AGGREGATES

Aggregates are solid bodies, ranging from fine sand particles to large coarse rocks which form around 70-80% of the concrete volume and are held in place by the cement paste. Aggregates are usually considered as only the “filler” in concrete; however, the type of aggregate strongly influences the fresh and hardened properties of concrete. Aggregates are therefore classified according to, among other factors, their size, grading, shape and surface texture. When considering the size, a distinction is made between coarse aggregates (for example crushed gravel or stone) and fine aggregates (for example natural sand). Usually, the coarse aggregates are graded such that each batch contains particles of different size fractions in suitable proportions so that the bulk mass contains lesser voids (fine particles fill the voids between large particles). A proper coarse aggregate grading produces dense concrete which requires less fine aggregate and cement paste, hence optimizing the cost. It must be noted that the size of the aggregates also affects the workability of the mixture. Since a collection of fine particles has a larger surface area when compared to larger particles, a mixture with fine grading requires more water to become workable. This means that bigger particles have higher workability for a fixed water content. Hence, an optimum between grading and workability must be found to produce a high quality concrete. The shape of aggregates also affects the workability: particles with lower specific surface area, for example rounded particles, require less cement paste to achieve the same workability as concrete containing aggregates with elongated and flat particles. Also, rough surface textures require more water than smooth surfaces since they produce more friction. If the particle is nonabsorbent, less water is required when compared to micro-porous particles.

A.1.3 ADMIXTURES

The materials which are present in concrete in addition to the basic constituents (aggregates/sand, cement and water) are referred to as admixtures. These materials are used to enhance the properties of concrete, for example by increasing the workability, strength, durability and homogeneity. The admixtures are mainly of the following two types:

1. *Mineral admixtures*

Mineral admixtures (also called pozzolans) are basically replacements of cement which possess little to no cementitious properties on their own, but which will form compounds with cementitious properties after reacting with CaO and water. The product which is formed is a high-quality cement gel which provides extra strength to the concrete. Mineral admixtures either occur in nature (for example materials from volcanic origin, clay and shales) or they can be produced using industrial waste, resulting in artificial admixtures such as fly ash, silica fume and blast furnace slag. Inert mineral admixtures (such as granite, marble, quartz or aggregate powder) can also be used as fillers with the purpose of reducing the concrete cost. These materials do not exhibit cementitious properties and therefore, they do not contribute to the strength of concrete.

2. *Chemical admixtures*

Chemical admixtures are used to modify the properties of concrete for a certain application or to overcome difficult construction situations, and, according to [Gambhir \[88\]](#) they can be broadly classified as general-purpose admixtures and specialty category admixtures. For the sake of brevity, only the general-purpose admixtures will be discussed as follows:

- *Water-reducing admixtures*

When water is added to the dry constituents of concrete, the cement and other fine particles (fly ash, silica fume etc.) clump together, a process known as “flocculation”. In doing so, the particles encapsulate small amounts of water which leads to an increase in viscosity, i.e., the mixture becomes more difficult to handle. One obvious way to resolve this problem is by adding extra water to the mixture which increases the flowability. However, as previously discussed, excess water can be detrimental to the hardened concrete properties and must generally be avoided. Water-reducing admixtures (also known as plasticizers) allow for higher flowability of fresh concrete without the need for extra water during production, thus providing increased strength, density, durability and reduced permeability of hardened concrete. When plasticizers are added, they are absorbed on the surface of cement particles and create repulsive forces between the flocculated particles. This results in dispersion of the particles, allowing the entrapped water to become available to fluidify the mixture. Depending on the degree of flocculation, the plasticizers are classified as normal, mid-range and high-range water reducers. High-range water reducers (HRWR, superplasticizers) are a special type of water-reducer which have a greater ability to reduce the water content (20-40%) of a given concrete mixture, and are especially used in high strength and low permeability concrete mixtures with higher contents of cementitious materials and mixtures containing silica fume.

- *Accelerating admixtures*

Accelerators are used to speed up the initial set of concrete either by: i) increasing the rate of hydration of hydraulic cement (hence increasing the strength development) or ii) shortening the setting time. This can be of great importance in the construction of for example underwater structures and waterfront structures in tidal zones. In general, the working principle of accelerators is to cause a more rapid dissolution of cement compounds, particularly C_3S . The most widely used accelerator is $CaCl_2$, which is dissolved in part of the mixing water before use.

- *Retarding admixtures*

Retarders slow down the initial rate of cement hydration or slow down the setting of cement paste in concrete by: i) forming a thin layer on cement particles, which slows down the dissolution and subsequent reaction with water or ii) increasing the intra-molecular distance of reacting silicates and aluminates from water molecules by forming a certain transient compounds in system. Once the silicates and aluminates hydrates are formed, the retarding effect diminishes and hydration occurs normally. By slowing down the initial hydration reaction, more water is available for workability and the concrete can be finished quickly. This is required for example in cases of high temperature, low humidity etc.

A.2 MATERIAL MIX DESIGN

Having presented the components of a concrete mixture, it is also relevant to discuss how these ingredients are proportioned. First, the factors which influence the choice of mix proportioning are discussed briefly. Next, some examples of typical concrete designs are presented.

A.2.1 MATERIAL REQUIREMENTS

When designing the concrete mix, the following key aspects are generally considered:

1. *Cost requirements*

One of the primary material design aspects is keeping the cost as low as possible. The cost of concrete is usually optimized by minimizing the amount of cement in the mixture, since it is the most expensive component. This is usually done by replacing Portland cement by pozzolans where possible, as previously discussed in Section [A.1.3](#).

2. *Short-term (fresh state) material requirements*

The most important property of fresh concrete is workability, which can be defined as the ease and homogeneity with which the material can be mixed, transported, placed and consolidated. The term “homogeneity” refers to the uniform and stable distribution of the constituents and the resistance to segregation. Workability is a complex property, which is a combination of two critical parameters [89]:

- *Consistency* (or fluidity) of a concrete mixture refers to the relative mobility of the concrete, or the ability of the fresh concrete to flow without segregation and bleeding. If a mix is too dry, it will be difficult to mix, place and compact and segregation may occur due to the lack of cohesiveness of the paste. On the other hand, if the mix is too wet, separation and segregation may also occur.
- *Stability* (or cohesiveness) indicates that fresh concrete should remain homogeneous, i.e., no segregation should occur. Segregation can be defined as the separation of the constituents of a mixture, such that their distribution is no longer uniform, as will be discussed later.

3. *Long-term (hardened state) material requirements*

Concrete is a versatile building material which can be suited for various applications. Hence, the

composition of concrete mixtures depends on the purpose of the material. The most important properties which define the material purpose are:

- *Strength*, which is a measure of the loads which can be applied to the material. Since hardened concrete is a brittle material, its strength is primarily governed by posterity of the cement paste. As discussed in Section A.1.1, the porosity in hardened state depends on the w/c ratio: the strength of fully compacted concrete increases as the w/c ratio decreases. Other factors which influence the strength are size, shape, grading and strength of aggregate used in the mixture [90].
- *Durability*, which refers to the material's ability to withstand aggressive environmental conditions (such as freezing and thawing, wetting and drying), chemical attack etc. Generally, the durability is also improved by minimizing the w/c ratio since a low water content decreases the permeability of the material in hardened state and therefore the penetration of deteriorating agents.

A.2.2 TYPES OF CONCRETE

From the discussion above it is clear that the w/c ratio must be carefully considered for both the fresh state and hardened state properties of concrete. While workability is enhanced as the ratio increases, the strength and durability are adversely affected. Hence, an optimal balance must be found when determining the w/c ratio. Admixtures are usually incorporated during the production of fresh concrete in order to optimize the w/c ratio, depending on the desired hard-state properties. In the following, it is shown how the composition of traditional, ordinary concrete is modified such that the material is suitable for a variety of new applications.

Ordinary concrete

Ordinary concrete, also known as regular, normal weight or normal strength concrete, is usually produced by mixing Portland cement with aggregates and a water-chemical mixture. While the hardened material is good at resisting compressive loads, the tensile strength is relatively low. Therefore, these types of concrete are mainly used for pavements and buildings where there is no demand for high tensile strength.

High-performance concrete

High-performance concrete (HPC) is a collective name for various mixtures which conform to a set of standards above those of regular concrete. For example, high-strength concrete has a higher compressive strength than regular concrete. This is mainly achieved by using a low w/c ratio of 0.35 or lower. Also, mineral admixtures such as fly ash and silica fume are added to the concrete mixture to provide additional strength by reacting with hydration products, thereby creating additional C-S-H gel, which is the substance responsible for the ultimate strength. The combination of low w/c ratio and use of mineral admixtures imparts a significance decrease of workability on the concrete mixture. It is therefore common practice to use superplasticizers, which compensate for the decreased workability. Finally, aggregate properties such as strength and size, the surface characteristics and the bonding between aggregate particles and the cement paste must also be considered [91]. Some other examples of standards used in relation to HPC are: permeability, density, toughness, compaction

without segregation etc.

Self-compacting concrete

Concrete structures are traditionally made using casting, to define the desired form of the element, with subsequent compacting to ensure that the concrete achieves the required properties. Self-compacting concrete (SCC) is a highly flowable mixture which is able to spread into the formwork and encapsulate reinforcements

are i) high flowability due to high deformability of the paste and ii) stability, which refers to the high resistance to aggregate segregation. The high flowability is attained by using superplasticizers in larger amounts, instead of adding extra water when compared to regular concrete. The stability is achieved by lowering the content of coarse aggregate to a level lower than normal and/or by using admixtures that modify the viscosity of the mixture (viscosity modifying agents, VMA). Thus, SCC mixtures typically have higher paste volume, lower coarse aggregate content and higher sand-coarse aggregate ratio than regular concrete [92, 93].

Concrete for extrusion printing

In concrete printing, the casting process is replaced by extruding self-compacting concrete through a nozzle to fabricate forms. However, the requirements for concrete to be used in a printing process are significantly different from those involved in traditional casting since the material needs to be pumped towards the nozzle(s) and extruded as continuous filaments. Thus, the printing process imposes additional requirements on the properties of the concrete mixture. Several authors [94, 95, 96, 97] mention that the suitability of a mixture for 3D printing is generally measured against the following key benchmarking properties: extrudability, workability, buildability and open time. High extrudability and workability are desired to allow for a continuous, easy-flowing behavior of the printing material from the source to the nozzle. In addition, the material must have sufficient buildability characteristics to ensure that each layer of printed material remains in position once printed and is hard enough to support the weight of the subsequently printed layers. Meeting these criteria is already a big challenge, as the requirements seem to conflict with each other: the mixture must be relatively easy to extrude yet viscous enough to hold itself and the following layers. Moreover, a proper bonding between the layers is important in order to avoid structural collapsing. The open time refers to the amount of time during which the fresh concrete mix from the source can maintain sufficient workability. It is worth noting that the bonding strength decreases as the time gap between printing the layers increases. On the other hand, the time gap must be sufficiently long to allow for adequate hardening which provides the required mechanical strength for sustaining the weight of the following layers.

For extrusion printing, the typical components for concrete (cement, water and aggregates) remain unchanged, however, the constituents are proportioned differently. The mixture is typically of high cement content and the maximum aggregate size is usually in the order of 2 mm to 3 mm, classifying the material as mortar [1]. To provide an optimal combination of mixture properties as discussed above, chemical admixtures are also required. Superplasticizers (SP) are used to decrease the w/c ratio (in order to increase strength) while maintaining a desired flowability. However, the amount of SP should be limited to ensure sufficient buildability. Also, a combination of retarders and accelerators is used to control the setting time, so that the concrete does not set during transportation to the printing nozzle on the one hand, and that it start to set immediately after printing on the other hand [96]. Some authors [98, 99] also report the use of viscosity modifying agents (VMA) to avoid segregation,

which is particularly possible due to high pressure build-up in extruders.

A.3 CONCRETE HANDLING EQUIPMENT

A.3.1 TRANSPORTATION SCREWS

Screw conveyor systems are typically used for transportation of process material, both horizontally and vertically. A screw conveyor generally consists of a trough or tube containing a spiral blade coiled around a shaft. Screw conveyors are common when using cementitious materials, as constant agitation is required during the material handling in order to avoid hardening of the cement. Depending on the application, the rotating element is often designed to have a dual function, for example, mixing screw conveyors are capable of blending different products while they are conveyed. In this regard, mixer screw conveyors are not only used for conveying concrete in its wet state, but also for example to transport the dry concrete constituents to the main mixer, while pre-blending of the ingredients takes place. Some commonly encountered screw blade designs are shown in Table A.1. A more detailed description of their applications is available in [100].

A.3.2 MIXERS

A concrete mixer is a device designed for producing fresh concrete by combining measured proportions of cement, aggregates and water. The two main categories of concrete mixers are batch mixers and continuous mixers. The first type produces fixed amounts of concrete one at a time, which requires the mixer to be emptied completely after each cycle and reloaded to prepare a new batch of fresh concrete. In the second type, the mixer is continuously in operation with the constituents entering at one end and fresh concrete exiting at the other end [7, 101].

Batch mixers

Batch-type mixers are the most widely used in industry, since they allow for greater user control. After weighing and loading all the ingredients into mixer, the material is thoroughly mixed for a suitable period of time and subsequently discharged. This process is repeated until the required amount of concrete is produced. The duration of a mixing cycle is generally considered as the time from adding the dry ingredients to the end of discharging the mixture. Since the ingredients are mixed while being loaded to the mixer, the loading process is generally divided in two parts: dry mixing and wet mixing. Dry mixing refers to pre-blending of the dry constituents before adding water to the mixer. Wet mixing occurs during and after the addition of water. There are generally two types of batch mixers:

- Drum mixers, where the concrete is mixed in a double conical frustum shaped container with blades arranged on the inner surface of the drum. The purpose of the blades is to lift the material as the drum is in motion. The container can either be of the tilting, non-tilting or reversing type. Tilting mixers have a single opening which functions as both the inlet and the outlet. Rapid concrete discharge is achieved by tilting the drum downwards, i.e., the material exits the drum under the act of gravity. Non-tilting (horizontal) mixers are only able to rotate about their horizontal axis. An inclined chute at the end of the drum collects and discharges the concrete. The reversing drum mixers are similar to the non-tilting type, with the main difference being the way concrete is discharged. The mixing takes place as the drum rotates in one direction and

the mixture is discharged by rotating the drum in the opposite direction. Two different sets of blades are arranged for these actions. A summary of drum mixers is provided in Table A.2.

- Pan mixers, where concrete is mixed in a circular pan using blades which are arranged in the center of the pan. Some pan mixers have a stationary pan with blades rotating about a vertical axis of the pan, while others operate in the opposite way. In both cases, the mixer outlet is a central hole in the pan. Some examples are shown in Table A.3.

Continuous mixers

Continuous mixers are usually non-tilting drums with blades or paddles attached to a long rotating shaft in the middle of the drum, which mix the material while it is being transported towards the mixer outlet. Some examples are shown in Table A.4. Although no apparent classification for the geometry of the mixing tool was apparent in literature, the majority of continuous concrete mixers were found to be of the paddle type.

TABLE A.1. Types of conveyor screws, adapted from [100].

Denomination	Remarks	Illustration
Cut flight conveyor screws	Have notches cut in the periphery of either helicoid or sectional flights which supplement the conveying action with a moderate mixing action.	
Ribbon flight conveyor screws	Consist of continuous helical fighting formed from steel bar and secured to the pipe by supporting lugs.	
Conveyor screws with paddles	Have paddles spaced at intervals and set to partially oppose the forward flow, to provide a moderate mixing or stirring of materials being conveyed. Paddles are adjustable and may be set at any angle to produce the desired degree of agitation.	
Cut and folded flight conveyor screws	Provide folded segments which act as lifting vanes to produce a cascading effect. This promotes agitation and aeration, resulting in better mixing.	
Short pitch conveyor screws	Are of regular construction except that the pitch of the flights is reduced. They are recommended for use in inclined conveyors of 20 degrees slope and over, including vertical conveyors and are extensively used as feeder screws.	
Cut flight conveyor screws with paddles	Have paddles mounted at intervals and set to counteract the flow of materials, considerably increases the agitation and mixing action produced by the cut flights.	
Paddle conveyor screws	Have formed steel blades mounted on rod shanks inserted through the pipe. Conveying action can be controlled by adjusting the angle of the paddles	

TABLE A.2. Types of drum mixers, adapted from Beitzel [102].

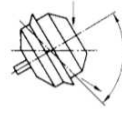
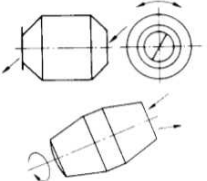
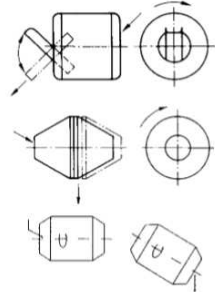
Denomination	Remarks	Illustration
Tilting drum inclined mixer	During mixing the axis is inclined, and emptying is effected by tilting of the drum axis.	
Reversing drum mixer	During mixing the axis is inclined or horizontal, and emptying is effected by reversal of the direction of rotation.	
Horizontal drum mixer	During mixing the axis is horizontal, and emptying is effected by the following possibilities: <ul style="list-style-type: none"> • Tilting of the drum axis, • Inserting a discharge into the drum, • Opening by splitting the drum whilst maintaining the same direction of rotation 	

TABLE A.3. Illustration of pan mixers, adapted from Beitzel [102].

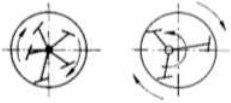
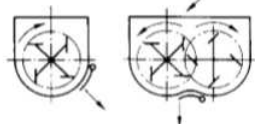
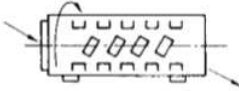
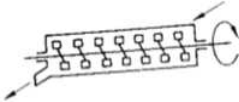
Denomination	Remarks	Illustration
Pan mixer	Mixer with fixed or rotating chamber, vertical or inclined axis. The fixed or rotating mixing paddles are concentric or eccentric.	
Trough mixer	Either one or two horizontal mixing shafts are mounted in a fixed or tilting open pan.	

TABLE A.4. Types of continuous mixers, adapted from Beitzel [102].

Denomination	Remarks	Illustration
Continuous drum mixer	Mixer with a cylindrical mixing chamber, in which the mixing tools are arranged among the horizontal or inclined axis, with permanent concrete output.	
Continuous trough single shaft mixer	Mixer with a horizontal or inclined mixing chamber, in which one mixing and conveying shaft rotates, with paddles inside.	
Continuous trough double shaft mixer	Mixer with a horizontal mixing chamber, in which two mixing and conveying shafts rotate, with paddles inside.	